Volume 10, Number 2, Spring 2024)

ACERP
Advanced Ceramics Progress

ISSN 2423-7477
e-ISSN 2423-7485

Advanced Ceramics Progress

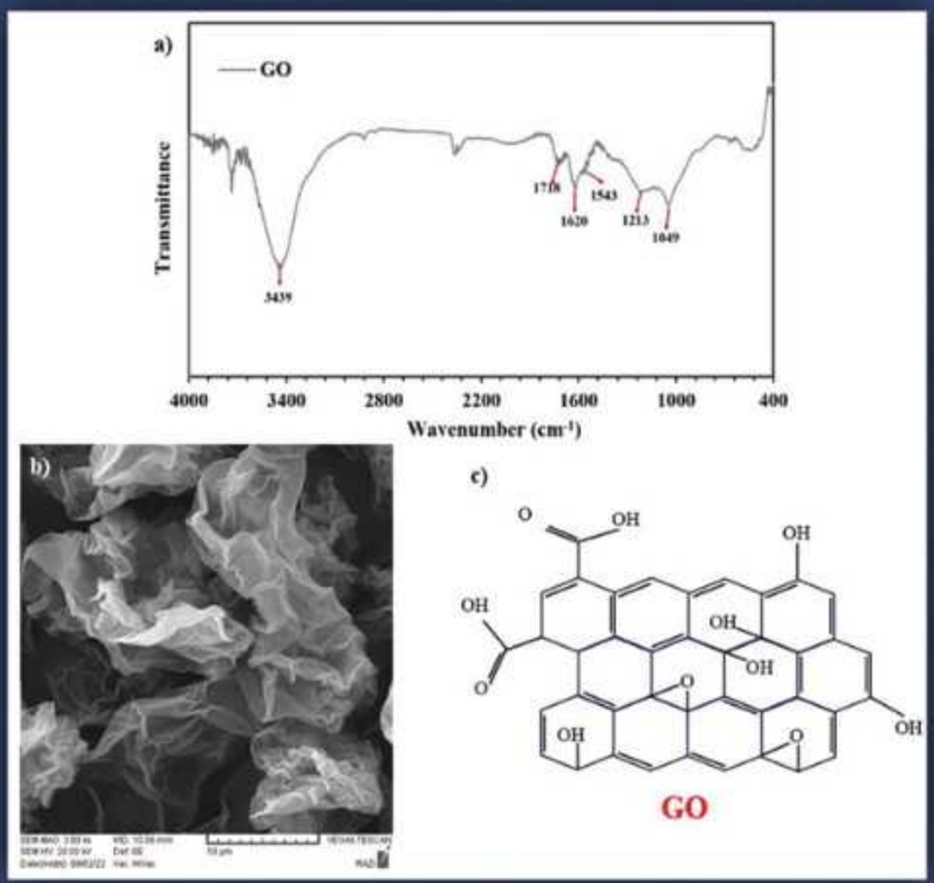

Materials and Energy
Research Center

Iranian Ceramic Society

In The name of God

Advanced Ceramics Progress

Advanced **Cer**amics **P**rogress (ISSN 2423-7477) (e-ISSN 2423-7485)

Web Site: www.acerp.ir, E-mail: office@acerp.ir
Tel: +98 (0) 26 36280040-7 ext.: 173, Fax: +98 (0) 26 36201888
Tel:+98 (0)21 88771626-7 ext.: 8931, Fax: +98 (0)21 88773352

Materials and Energy Research Center (MERC); Iranian Ceramic Society (ICERS)

AIMS AND SCOPE

Advanced Ceramics Progress (ACERP) as an ISC international journal is devoted to elucidating the fundamental aspects of chemistry and physics occurring at a wide range of oxide and nonoxide ceramics and composite materials and their processing, microstructure, properties, and applications. The journal provides a unique venue for publishing new exciting research, focusing on dynamic growth areas in this field.

INSTRUCTIONS FOR AUTHORS

Submission of manuscript represents that it has neither been published nor submitted for publication elsewhere and is result of research carried out by author(s).
Authors are required to include a list describing all the symbols and abbreviations in the paper. Use of the international system of measurement units is mandatory.

- On-line submission of manuscripts results in faster publication process and is recommended. Instructions are given in the ACERP web site: www.acerp.ir
- Hardcopy submissions must include MS Word and jpg files.
- Manuscripts should be typewritten on one side of A4 paper, double-spaced, with adequate margins.
- References should be numbered in brackets and appear in sequence through the text. List of references should be given at the end of the paper.
- Figures' captions are to be indicated under the illustrations. They should sufficiently explain the figures.
- Illustrations should appear in their appropriate places in the text.
- Tables and diagrams should be submitted in a form suitable for reproduction.
- Photographs should be of high quality saved as jpg files.
- Tables, illustrations, figures and diagrams will be normally printed in single column width (8 cm). Exceptionally large ones may be printed across two columns (17 cm).

PAGE CHARGES AND REPRINTS

ACERP subscribers do not need to make any payment for publication and reprints.

AUTHORS CHECKLIST

- Author(s), bio-data including affiliation(s) and mail and e-mail addresses.
- Manuscript including abstract, key words, illustrations, tables, figures with figures' captions and list of references.
- MS Word files of the paper.

Advanced **Cer**amics **P**rogress,
P.O. Box 31787-316, Karaj, Alborz, I. R. Iran
Materials and Energy Research Center, Imam Khomeini Blvd, Meshkin Dasht, Karaj, Alborz, I. R. Iran
P.O. Box 14155-4777, Tehran, I. R. Iran
No. 5, Ahuramazda St., Alvand Ave., Argentine Sq., Tehran, I. R. Iran

www.merc.ac.ir - www.acerp.ir

ISSN: 2423-7477; e-ISSN: 2423-7485

Advanced Ceramics Progress: Vol. 10 , No. 2, (Winter 2024) 1-48

CONTENTS

Advanced Ceramics Progress: Vol. 10, No. 2, (Spring 2024) 1-8

Materials and Energy Research Center
MERC

Contents lists available at ACERP

Advanced Ceramics Progress

Journal Homepage: www.acerp.ir

Original Research Article

Effect of Processing Parameters and Additives on Partially Sintering of Si_3N_4-$MoSi_2$ Composite

Seyed Ali Tayebifard

Associate Professor, Department of Semiconductors, Materials and Energy Research Center, Karaj, Iran.

*Corresponding Author Email: a.tayebifard@merc.ac.ir (S. A. Tayebifard)

URL: https://www.acerp.ir/article_209610.html

ARTICLE INFO

Article History:
Received: 28 April 2024
Revised: 09 September 2024
Accepted: 16 November 2024

Keywords:
Porous Composite,
Si_3N_4,
$MoSi_2$,
Additive,
Paritially Sintered

ABSTRACT

Addition of $MoSi_2$ to Si_3N_4 matrix leads to an improvement in the mechanical properties and oxidation resistance as well as an increase in the electrical conductivity of the produced composite, thus allowing for machining via Electrical Discharge Machining (EDM) or its potential applications as pieces of tinder (igniter) in diesel engines or aerospace devises. In this study, Si_3N_4 powder was mixed with $MoSi_2$ (synthesized in the previous work through SHS) and additives such as MgO, CeO_2, and Y_2O_3 in varying percentages. Some of the mixed powders were milled using a SPEX 8000. All material powders were then formed into pellets using a uniaxial press. The pellets were then sintered in an atmosphere-controlled tube furnace in argon at a maximum temperature of 1500 °C with a soaking time of 2 or 3 hours through Pressureless Sintering (PLS) process. The sintered samples were analyzed at different stages: density measurements, phase and microstructure studies using XRD and SEM, and HV microhardness measurements. The results demonstrated that Si_3N_4-$MoSi_2$ structural porous composites were successfully prepared and optimized by controlled parameters such as pressing pressure, milling process, type and percentage of additives, and soaking times.

https://doi.org/10.30501/acp.2024.453495.1151

1. INTRODUCTION

Two categories of different materials are candidates for stability at working temperatures of approximately 1200 ° C. The first category includes structural ceramics such as SiC and Si_3N_4 while the second one consists of structural silicons such as $MoSi_2$ (Tapia-Lopez et al., 2023). The structural materials based on Si_3N_4 are among the most commonly used ceramics in engineering owing to their unique properties namely thermal shock resistance, thermal resistant under load at high temperature, chemical impartiality, and excellent wear resistance (Singh et al., 2004; Lai et al., 2018; Charfi et al. 2002; Sciti et al., 2002) However, they also exhibit some limitations, including difficult sinterability due to their high-temperature sintering requirement (about 2000°C), decomposition at temperatures above 1900°C, need for improved oxidation resistance under working conditions over a long time (10,000 hours), difficult and costly machining due to their hardness and high electrical resistivity (~ 1014Ωcm), unreliable stability of properties in long-term applications, and insufficient fracture toughness for applications such as engine components. These limitations hinder the industrial use of silicon nitride.

As a result, the Si_3N_4 composites have been developed to improve these properties (Singh et al., 2004). $MoSi_2$ is one of the candidates for constructing composites with Si_3N_4 (Jankowiak et al., 2013; Lizuka et al., 2002). The properties of Silicon Nitride and Molybdenum Disiliide suggest that these two compounds can complement each other. For example, Si_3N_4 has good creep resistance at high temperatures while $MoSi_2$ contributes to toughening at low temperatures and plays a role in the flexural phase at high temperatures in the composite. Additionally, $MoSi_2$ is a conductive material and consequently, after its addition to Si_3N_4, the resulting

Please cite this article as: Tayebifard, S. A.. (2024). Effect of Processing Parameters and Additives on Partially Sintering of Si_3N_4-$MoSi_2$ Composite, *Advanced Ceramics Progress*, 10(2), 1-8. https://doi.org/10.30501/acp.2024.453495.1151

composite can become conductive and machined through Electrical Discharge Machining (EDM) (Singh et al., 2004).

Several synthesis methods have been proposed for preparing this composite, including metallurgical powder, combustion synthesis, two-step method HP/HIP, reaction bonding, combustion synthesis, and infiltration (Liu et al., 2022). Porous ceramics, widely used in different industrial fields such as filters, bioreactors, catalyst carriers, etc. (Yang et al., 2001), have been extensively studied experimentally and theoretically, regardless of their low strain at failure (Kota et al., 2023). Materials based on porous Si_3N_4 with rod-type β-Si_3N_4 grains possess excellent mechanical properties and chemical neutrality (Yang et al., 2001).

In this work, Si_3N_4 and $MoSi_2$ (synthesized through Self-propagating High-temperature Synthesis (SHS) in previous works (Fasihi Dastjerdi, et al., 2012; Shahbazi et al., 2016)) were selected as the raw materials. The structural composites were then produced using powder metallurgy and Pressureless Sintering (PLS). During the study, several parameters such as reactant activation through milling, green compact pressing pressure, and type and percentages of the sintering aids were optimized.

2. MATERIALS AND METHODS

2.1. MATERIALS

Si_3N_4 powder (particle size (45μm)), composed mainly of α-Si_3N_4, purity> 99%, was sourced from Aldrich Company, USA. $MoSi_2$ powder (particle size of 9μm) was synthesized in previous works (Yang et al., 2001; Kota et al., 2023) by SHS. MgO, Y_2O_3 and CeO_2 powders (particle sizes of 3μm), (4μm) and (10μm), respectively) with commercial grade purity, were used as sintering aids.

2.2. COMPOSITE SYNTHESIS

In this step, both Si_3N_4 and $MoSi_2$ synthesized powders (Yang et al., 2001; Kota et al., 2023) were weighted as the main constituents based on a 50/50 vol% ratio. MgO, Y_2O_3 and CeO_2 powders were added individually or together as sintering aids based on Table 1.

Initially, these powders were mixed, and a portion was milled using a Spex 8000 high-energy ball mill. Then all mixed and milled powders were granulated. To prepare the granulate powders, 3wt% Carboxymethyl Cellulose (CMC) binder and a few drops of water were thoroughly mixed, and the mixture was passed through a 40-mesh sieve. In the next step, the granulated powder was pressed into pellets using a uniaxial press at the pressure range of 300-900 MPa. The density of the green compacts was then measured geometrically. Followed by calculating the theoretical density of each sample based on the chemical composition density of its components and mixture of rules in composites, the green relative density of this samples was obtained accordingly. Afterward, the green compact composite samples were sintered in an atmospheric control furnace for the soak time of 2-3 hours at 1500ºC (Ramachandra et al., 2022).

First, the density and porosity of the products were measured using the Archimedes immersion method according to the ASTM C373-88 standard. Finally, the products were analyzed by XRD (Philips, PW3710), SEM (Stereo Scan 360-Leica Cambridge), and microhardness (Akoshi, MVK-H21).

TABLE 1. Introduction of the process parameters, additive, and sample number

Sample No.	Press Pressure (MPa)	Milling Time (h)	Sintering Aid (type & percentage)	Maximum Temperature of Sintering (ºC)	Soaking Time (h)
1	300	0	5wt% MgO	1500	2
2	450	0	5wt% MgO	1500	2
3	600	0	5wt% MgO	1500	2
4	750	0	5wt% MgO	1500	2
5	900	0	5wt% MgO	1500	2
6	600	0	10wt% MgO	1500	2
7	600	1	5wt% MgO	1500	2
8	600	1	10wt% MgO	1500	2
9	600	0	5wt% MgO	1500	3
10	600	1	5wt% MgO	1500	3
11	600	0	10wt% MgO	1500	3
12	600	1	10wt% MgO	1500	3
13	600	0	5wt% MgO + 5wt% CeO_2	1500	3
14	600	1	5wt% MgO + 5wt% CeO_2	1500	3
15	600	0	5wt% Y_2O_3	1500	3
16	600	1	5wt% Y_2O_3	1500	3
17	600	0	10wt% Y_2O_3	1500	3
18	600	1	10wt% Y_2O_3	1500	3

3. RESULTS AND DISCUSSION

3.1. PRESS PRESSURE

The pellets were pressed from the granulate powders using uniaxial press, as mentioned earlier. Figure 1 shows the effect of press pressure on the Relative Density (RD) of the green compacts and final products. As seen in this figure, when the pressure on the granulate powders increases up to 600MPa, the relative density of the green compacts and final products increase. However, if the compression pressure exceeds 900 MPa, the final product densities will not change significantly but the green compact density will decrease.

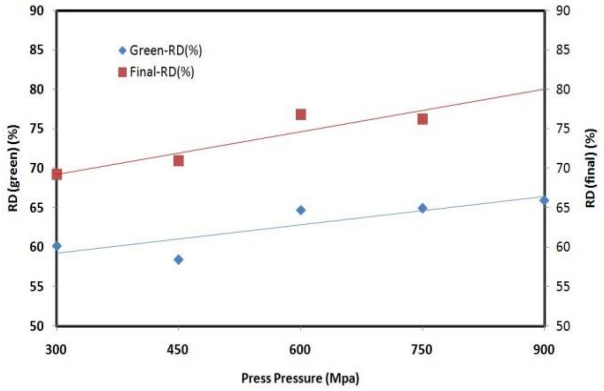

Figure 1. The effect of press pressure on green compacts & final products relative densities (RD). (sintering aid: 5wt% MgO, Max. Temperature: 1500ºC and 2h soaking time)

As noted in the references, increasing press pressure on the powder increases the density of the green compact up to a certain level. Beyond that point, with continues applied pressure, the increase in the green compact density will stop mainly because with higher pressure, there is no more space left in the grain powder to move and slide, thus preventing further density increase. Therefore, increasing pressure beyond a certain level is ineffective in enhancing density (Angelo et al., 2008; German, 2005). After optimizing the compression pressure, the samples were prepared based on the optimal pressure (600MPa) and are referred to in Figure 1.

Figure 2 shows the XRD pattern of the sintered sample. According to this figure, both Si_3N_4 and $MoSi_2$ are the main phases, indicating that the Si_3N_4-$MoSi_2$ composite has been successfully produced.

Figure 3 shows the microstructure of the fracture surface of this sample at two magnifications. This figure reveals a relatively homogenized microstructure with high porosity. However, upon closer examination, a dual morphology of coarse and fine grains can be detected. The grain boundaries of the coarse grain exhibit a curved shape, confirming the formation of liquid phase during the sintering process.

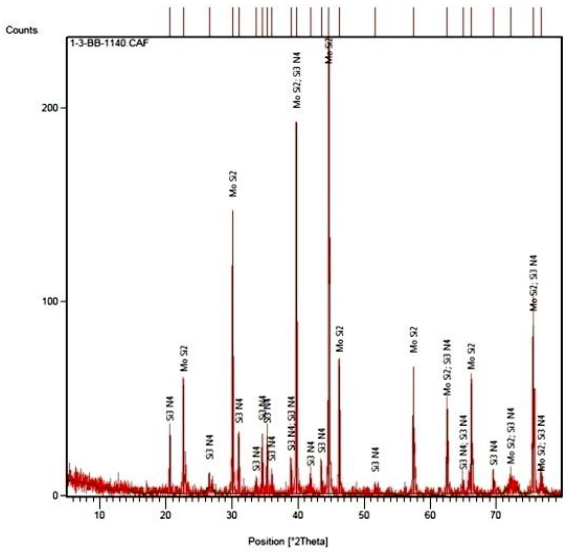

Figure 2. XRD patterns of composite (Si_3N_4-$MoSi_2$) sintered (sintering aid: 5wt% MgO, Press Pressure: 600 MPa, Max. Temperature: 1500ºC and 2h soaking time)

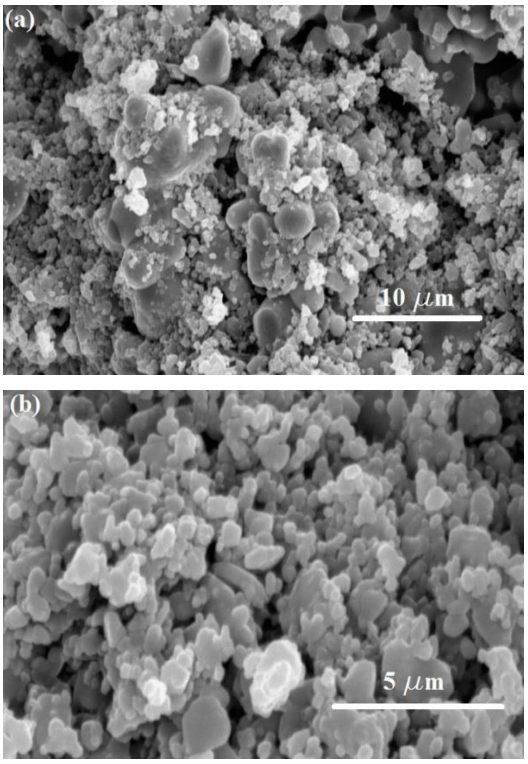

Figure 3.SEM micrographs of fracture surface of sample in secondary mode with two magnification: a- 3000 X and b- 8000 X (sintering aid: 5wt% MgO, Press Pressure: 600 MPa, Max. Temperature: 1500ºC and 2h soaking time)

3.2. MILLING

Part of the powders were milled using a Spex 8000 high energy mill before the pressing step. Table 2 shows

the effect of milling process on the densities of the green and final samples.

In addition, Figure 4 presents the green and sintered density diagrams of samples as a function of milled or unmilled raw materials.

It can be stated that the milling process of raw materials caused a significant increase in the final density of the samples, as seen in Table 2 and Figure 4.

The milling process also affects the microstructure of the samples. Figure 5 shows the SEM micrographs of Samples No. 3 and 7. According to this figure, sample No. 3 (un-milled) exhibits a coarser, more heterogeneous, and more porous than microstructure than sample No. 7 (milled).

In addition, Figure 6 shows the SEM micrographs of samples No. 6 and 8. In this figure (similar to Figure 5), sample No. 8 (milled) displays a finer and homogeneous microstructure than sample No. 6 (un-milled).

Milling, resulting from slipping together, not only reduces and refines the grain size of the raw materials but also increases the density (Figure 4) and microstructural homogeneity (Figure 5) of the samples. Moreover, the surface activity of the powder is increased by milling, which, in turn, enhances the final sample density (Singh et al., 2004).

TABLE 2. The effect of milling process on the green and final samples density and porosity

Sample No.	Milling Time (h)	RD green(%)	RD final(%)	Apprent Porosity(%)
3	0	65	77	22
7	1	75	78	21
6	0	73	65	33
8	1	77	85	14

3.3. SYNTERING AID

In this research, both values and types of sintering aids were studied.

3.3.1. SYNTERING AID VALUES

Samples No. 7 and 8 (containing MgO as the sintering aid) and No. 16 and 18 (containing Y_2O_3 as the sintering aid) were selected to investigate the effect of sintering aid on the density of the final sample.

Table 3 shows that the final density of the samples increased upon increasing the sinter aids value. Figure 7 demonstrates the SEM micrograph of samples No. 7, 8, and No. 16, 18. In this Figure, the microstructure of samples No. 8, 18 relatively more homogeneous with lower porosity, fewer detectable grain boundaries, fewer detectable individual grains, compared to sample No. 7, 16, respectively. These observations suggest that in these samples, the liquid phase was sufficiently produced and distributed within the sample microstructure during the sintering process due to the adequate sintering aid in these samples (German, 1996; German, 1985).

TABLE 3. The effect of the sintering aid value on the density and porosity of the final samples

Sample No.	Sintering Aid (type & percentage)	RD final (%)	Apprent Porosity(%)
7	5wt% MgO	78	21
8	10wt% MgO	85	14
16	5wt% Y_2O_3	76	23
18	10wt% Y_2O_3	81	18

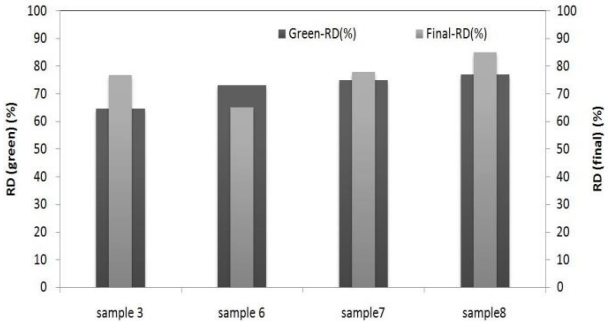

Figure 4. The effect of milling of raw materials on green and final samples density

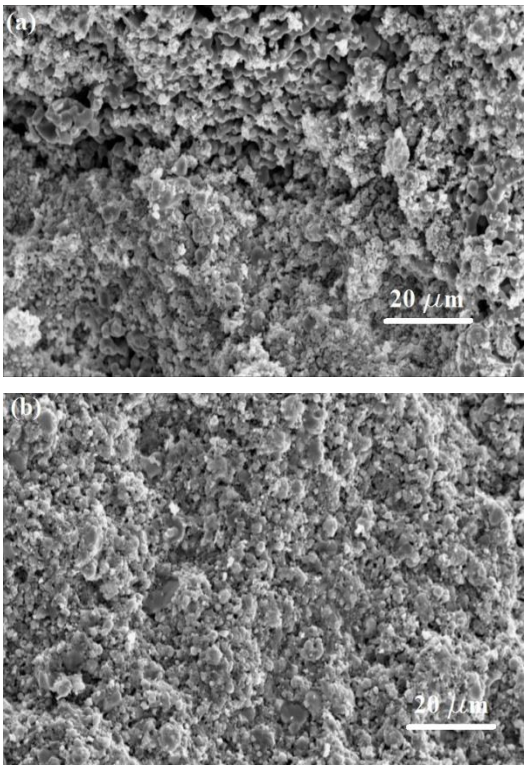

Figure 5. SEM micrographs of fracture surface of sample in secondary mode: a- No. 3 and b- no.7

3.3.2. SYNTERING AID TYPES

Liquid-phase properties such as viscosity, stability, and liquid-phase initiation temperature, among others, are related to the type of sintering aid used (Tayebifard, 2023; Heinrich et al., 2001). In this study, three types of synthesis aids were used in varying percentages (Table

4). Table 4 presents the final density and microhardness of the samples with similar preparation conditions but with different sintering aids used in their combinations. This table demonstrates that the sample containing milled raw materials and MgO as a sintering aid has a higher density than other samples. This is likely because MgO mixes well with other oxides (impurities) in these samples and is evenly distributed throughout the microstructure. Based on these assumptions, a homogeneous liquid phase is formed throughout the sample microstructure, resulting in higher or more controllable density in the samples (Figure 9). But why does this liquid phase form in samples doped with these additives? The sintering additive reacts with the oxygen-containing phases, such as SiO_2 or oxinitride, which are always present on the surface of commercially available Si_3N_4 powders, to form the liquid phase. Impurities in the starting powder are often also incorporated into this silicate melt as well (Ziegler et al., 1987).

As illustrated in Table 4, samples containing Y_2O_3, are characterized by less hardness than those with MgO and MgO-CeO_2. Accordingly, sample No. 8 demonstrates the best properties.

Non-homogeneous microstructure of these samples may account for their lower hardness (Figure 9). In Figure 8, the density and hardness of samples with various sintering aids are compared.

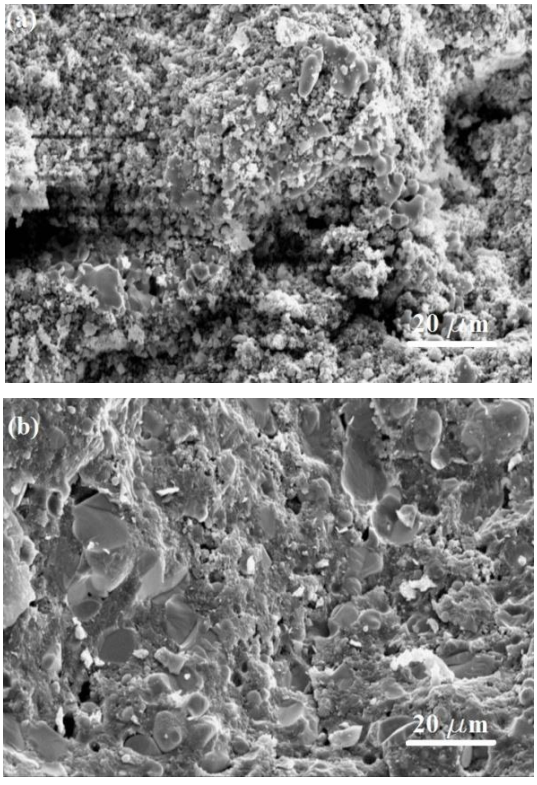

Figure 6. SEM micrographs of the fracture surface of samples in secondary mode: a- No. 6 and b- no.8

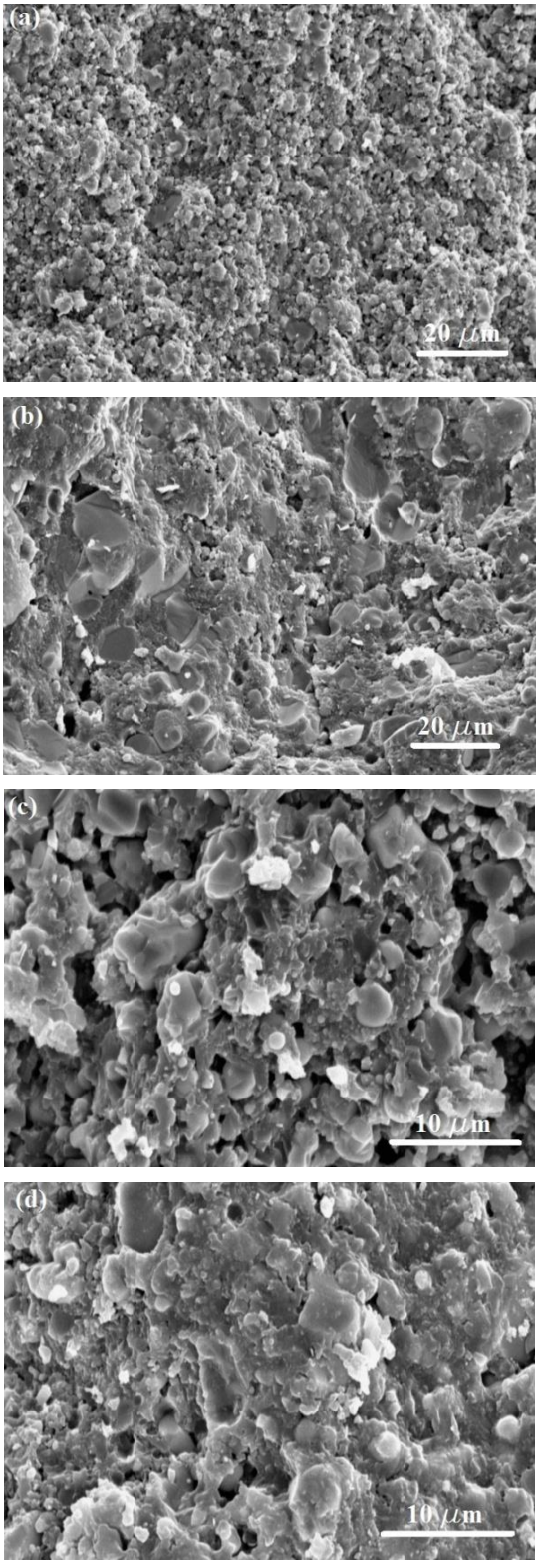

Figure 7. SEM micrographs of the fracture surface of samples in secondary mode: a- No. 7, b- No. 8, c- No. 16 and d- No. 18

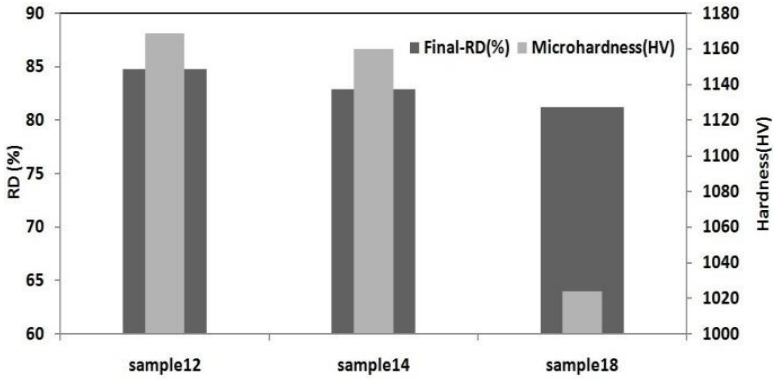

Figure 8. A comparison of the density and hardness of samples with various sintering aids

TABLE 4. The effect of the sintering aid type and soaking time on the densification and microharness of the final samples

Sample No.	Milling Time (h)	Sintering Aid (type & percentage)	Soaking Time (h)	RD final(%)	Apprent Porosity(%)	Microharness (HV)
7	1	5wt% MgO	2	78	21	-
8	1	10wt% MgO	2	85	14	1279
10	1	5wt% MgO	3	67	32	-
11	0	10wt% MgO	3	65	34	-
12	1	10wt% MgO	3	85	14	1169
13	0	5wt% MgO + 5wt% CeO_2	3	73	26	-
14	1	5wt% MgO + 5wt% CeO_2	3	83	15	1160
17	0	10wt% Y_2O_3	3	68	31	-
18	1	10wt% Y_2O_3	3	81	18	1024

Figure 9 shows the microstructure of the samples containing various sintering aids (as seen in Table 4). In this figure (9-a), the sample with MgO has a relatively homogeneous microstructure. As the sintering temperature rises, the spherical morphological phase becomes homogenously distributed. Figure 9b presents the microstructure of the sample containing MgO-CeO_2. In this sample microstructure, the matrix is homogeneous, and a small amount of visible porosity is present. Figure 9-c shows the microstructure of the sample containing Y_2O_3. This microstructure is not homogeneous, and the grains are not well-connected. It appears that the selected sintering temperature (1500°C) for this sample is insufficient to melt the glass phases containing Y_2O_3, leading to an incomplete and non-homogeneous final glass phase.

3.4. SOAKING TIME[1]

The density and microhardness of some samples sintered with different soaking times are compared in Table 4. These samples have similar composition and processing steps but vary in soaking times. Table 4 shows the final density of similar samples is not affected by soaking time; however, their hardness differ depending on the soaking time. For example, sample No. 12, with a soaking time of 3 hours, has lower hardness than sample No. 8, with a soaking time of 2 hours. The aspect ratio (l/d) is reduced with an increase in soaking time, where l is the length and d the diameter of the grain. Conversely, the mechanical properties of Si_3N_4, as a structural ceramic, improve with an increase in the percentage of β-phase, along with a higher aspect ratio. However, the increase in the soaking time leads to the growth of grain diameter, thus resulting in a reduction in the grain aspect ratio as well as the mechanical properties (Table 4) (German, 1996).

Figure 10 demonstrates the XRD patterns of samples No. 8 and 12. The analysis of these patterns confirms the presence of Si_3N_4 and $MoSi_2$ as the main phases in the desired composite. As evident in this figure, the presence of these phases is not affected at different soaking times.

Upon careful study of these patterns, several points can be understood. Table 5 shows the presence of α and β phases of samples No. 8 and 12. The table indicates that the α-Si_3N_4 score is higher than the β-Si_3N_4 score in both sample patterns. On the contrary, the β-phase score in sample No. 12 is higher relative that in sample No. 8. According to the reference, β-phase precipitates from the liquid phase (German, 1996). Therefore, increasing the soaking time can lead to an increase in the liquid phase during sintering and result in an increase of the β-phase score

[1]Time to keep the sample at maximum temperature

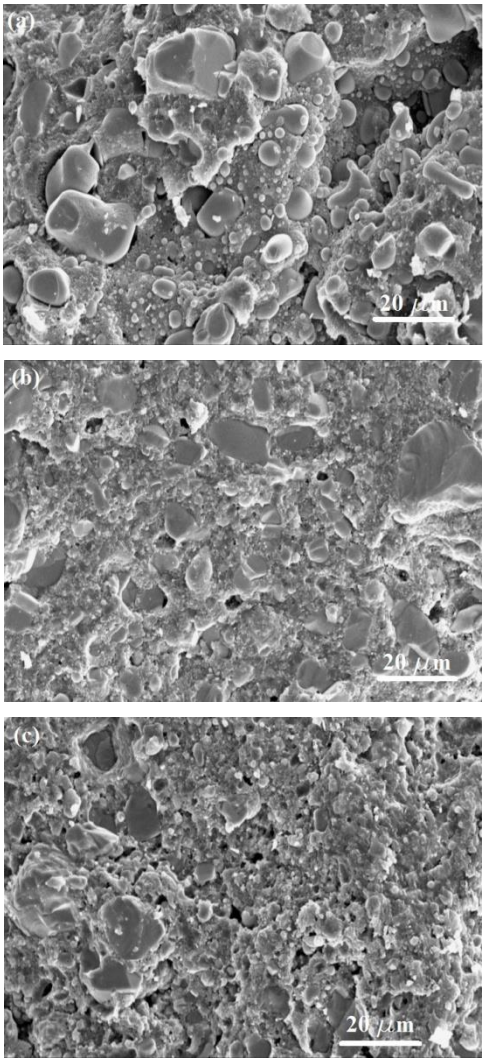

Figure 9. SEM micrographs of the fracture surface of samples in secondary mode: a- No. 12, b- No. 14, c- No. 18

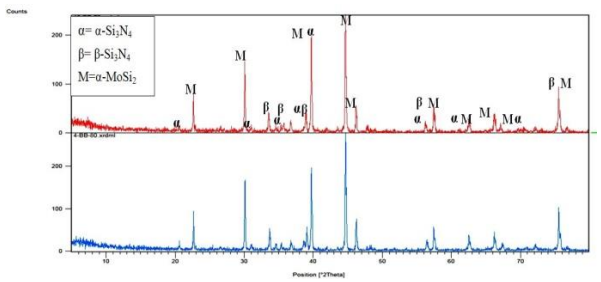

Figure 10. The XRD patterns of samples No. 8 and 12 (refer to Table 5)

TABLE 5. The effect of soaking time on score of types of the Si_3N_4 phases.

Sample No.	Soaking Time (h)	Score α-Si_3N_4	Score β-Si_3N_4	α/β (score)
8	2	12	2	6
12	3	15	8	1.88

Figure 11 presents the micrographs of samples No. 8 and 12. The significant difference between these two samples of microstructure is that in Figure 11-b, unlike Figure 11-a, some grains exhibit a spherical morphology. As mentioned earlier, the longer soaking time provides an opportunity for the grains to increase in diameter.

The reduction of the length-to-diameter ratio, which reflects the deformation of the pulled grains into a quasi-spherical shape, reduces the mechanical properties of the samples. For instance, this reduction is observed in the microhardness values shown in Table 4.

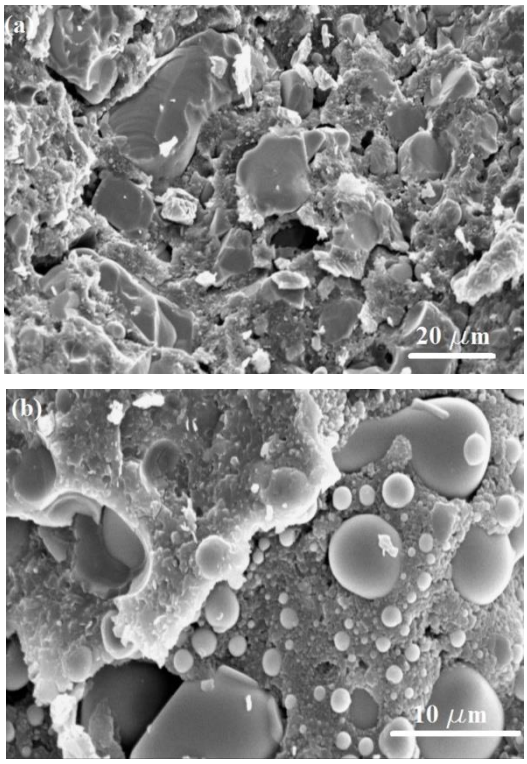

Figure 11. SEM micrographs of fracture surface of sample in secondary mode: a- No. 8, b- No. 12 (refer to table 5)

4. CONCLUSIONS

Increasing the compression pressure was an optimal approach to enhance the final density.

Milling of raw materials improved the final density as well as the homogeneity of the samples' microstructure.

The percentage and type of the sintering aid added to the raw material samples affected the densification and hardness of the final product. therefore, the sample No. 8 demonstrated the best properties.

An increase in the soaking time, although not affecting the sample density, resulted in an increase in the sample hardness due to higher aspect ratio and β-Si_3N_4 score.

Finally, these parameters were optimized in this research, resulting in the production of a composite with optimized porosity, homogeneity microstructure, favorable phase distribution, and optimum mechanical properties.

ACKNOWLEDGEMENTS

The author would like to acknowledge the financial support from Materials & Energy Research Center (MERC) of Iran for this research, based on grant number of 421392016.

REFERENCES

1. Angelo, P. C., & Subramanian, R. (2008). *Powder metallurgy: Science, technology and applications*. PHI Learning Pvt. Ltd. ISBN: 8120332814, 9788120332812. https://books.google.com/books/about/POWDER_METALLURGY.html?id=7cmb7BgZtvIC

2. Charfi, A., Ruttba, R., Kharrat, A. M., Wani, M. F., Dammak, M., & Sehgal, R. (2002). Friction and wear characterization of nanocomposites based on Si_3N_4 reinforced with SiC, Mo, and $MoSi_2$ nanoparticles. *Transactions of the Indian Institute of Metals*, *75*(3), 855–865. https://doi.org/10.1007/s12666-021-02494-1

3. Fasihi Dastjerdi, H., Tayebifard, S. A., Alizadeh, M., & Doroudian, M. (2012). Investigating the synthesis of $MoSi_2$ nanocrystal powder as a material capable of being used in industrial gas burners and jet turbine engines from commercial raw materials by self-propagating high-temperature synthesis (SHS). *Ith CNN, Shahrood*. https://civilica.com/doc/143255/

4. German, R. M. (1985). *Liquid phase sintering*. Springer Science & Business Media. ISBN: 978-1-4899-3601-1. https://link.springer.com/book/10.1007/978-1-4899-3599-1

5. German, R. M. (1996). *Sintering theory and practice*. John Wiley. ISBN: 978-0-471-05786-4. https://www.wiley.com/en-us/Sintering+Theory+and+Practice-p-9780471057864

6. German, R. M. (2005). *A-Z of powder metallurgy*. Elsevier. ISBN: 1856174298, 9781856174299. https://www.amazon.com/Powder-Metallurgy-Metal-Powders-Technology/dp/1856174298

7. Heinrich, J. G., & Aldinger, F. (2001). *Ceramic materials and components for engines*. John Wiley & Sons. Print ISBN: 9783527304165 | Online ISBN: 9783527612765 | https://doi.org/10.1002/9783527612765

8. Jankowiak, A., Valle, R., & Parlier, M. (2013). Potential of innovative ceramics for turbine applications. ODAS, Palaiseau, France. https://onera.hal.science/hal-01057786/document

9. Kota, N., Jana, P., & Roy, S. (2023). Elastic properties of porous silicon nitride fabricated via a low-temperature processing route. *Ceramics International*, *178*(49), 7066–7079. https://doi.org/10.1016/j.ceramint.2022.10.046

10. Lai, J., Kadin, Y., & Vieillard, C. (2018). Characterization and modelling of the degradation of silicon nitride balls with surface missing-material defects under lubricated rolling contact conditions. *Wear*, *398–399*, 48–54. https://doi.org/10.1016/j.wear.2017.12.007

11. Liu, Y., Xin, R., He, F., Qiu, & You, Zh. (2022). Novel approach to prepare Fe-TiN cermets from ilmenite concentrate using clean NH_3 gas. *International Journal of Refractory Metals and Hard Materials*, *108*, 105943. https://doi.org/10.1016/j.ijrmhm.2022.105943

12. Lizuka, T., Murao, T., Yamamoto, H., & Kita, H. (2002). Microstructures and properties of Mo_5Si_3-particle-reinforced Si_3N_4-matrix composites. *Journal of the American Ceramic Society*, *85*(4), 954–960. https://doi.org/10.1111/j.1151-2916.2002.tb00198.x

13. Ramachandra Rao, R. (2023). Dielectric constant and flexural strength of micro-porous slip-cast partially sintered silicon nitride. *Ceramics International*, *48*(23, Part B), 35927–35936. https://doi.org/10.1016/j.ceramint.2022.10.002.

14. Sciti, D., Guicciardi, S., & Bellosi, A. (2002). Microstructure and properties of Si_3N_4–$MoSi_2$ composites. *Journal of Ceramic Processing Research*, *3*(3), 87–95. http://www.jcpr.or.kr/journal/archive/view/90

15. Shahbazi, M., Tayebifard, S. A., & Razavi, M. (2016). Effect of Ni content on the reaction behaviour and microstructure of TiB_2–TiC/Ni cermets synthesized by MASHS. *ACERP*, *2*(2), 22–26. https://doi.org/10.30501/ACP.2016.70020

16. Singh, S., Godkhindi, M. M., Krishna Rao, R. V., & Murty, B. S. (2004). Effect of mechanical activation on synthesis of ultrafine Si_3N_4–$MoSi_2$ in situ composites. *Materials Science and Engineering A*, *382*, 321–327. http://dx.doi.org/10.1016/j.msea.2004.05.015

17. Tapia-López, J., & Pech-Canul, M. I. (2023). Processing, microstructure, properties, and applications of $MoSi_2$-containing composites: A review. *Frontiers in Materials*, *10*, 1165245. https://doi.org/10.3389/fmats.2023.1165245.

18. Tayebifard, S. A. (2023). *Non-oxide engineering ceramics*. Coarse Note, Materials and Energy Research Center. http://faculty.merc.ac.ir/tayebifard/

19. Yang, J. F., Zhang, G. J., & Ohji, T. (2001). Fabrication of low-shrinkage, porous silicon nitride ceramics by addition of a small amount of carbon. *Journal of the American Ceramic Society*, *84*, 1639–1641. https://doi.org/10.1111/j.1151-2916.2001.tb00890.x

20. Ziegler, G., Heinrich, J., & Wotting, G. (1987). Review relationships between processing, microstructure, and properties of dense and reaction-bonding silicon nitride. *Journal of Materials Science*, *22*, 3041–3086. https://doi.org/10.1007/BF01161167

Advanced Ceramics Progress: Vol. 10, No. 2, (Spring 2024) 9-16

Materials and Energy Research Center
MERC

Contents lists available at ACERP

Advanced Ceramics Progress

Journal Homepage: www.acerp.ir

Original Research Article

Effect of pH of the Electroless Bath on Microstructure and Corrosion Behavior of Ni-Co-La_2O_3-CeO_2 Coating

Katayoon Soleimani Roodi [a], Hadi Ebrahimifar [b,*], Farhad Mohsenifar [c]

[a] *MSc Candidate, Department of Materials Engineering and Metallurgy, Faculty of Engineering, Shahid Bahonar University, of Kerman, Kerman, Iran.*

[b] *Associate Professor, Department of Materials Engineering, Faculty of Mechanical and Materials Engineering, Graduate University of Advanced Technology, Kerman, Iran.*

[c] *Assistant Professor, Mechanical Engineering Department, Faculty of Engineering, Higher Education Complex of Bam, Bam, Kerman, Iran.*

* Corresponding Author Email: H.ebrahimifar@kgut.ac.ir (H. Ebrahimifar) URL: https://www.acerp.ir/article_209453.html

ARTICLE INFO

Article History:
Received: 14 September 2024
Revised: 09 October 2024
Accepted: 12 November 2024

Keywords:
Corrosion Resistance,
Composite Coating,
Potentiodynamic Polarization,
Electrochemical Impedance Spectroscopy

ABSTRACT

In this study, Ni-Co-La_2O_3-CeO_2 composite coatings were deposited on an AISI 430 steel substrate using the electroless method. The microstructure and corrosion behavior of coatings obtained at different bath pHs (8, 8.5, 9, 9.5, and 10) were investigated. Coating characterization was performed using a scanning electron microscope (SEM). To assess corrosion resistance, potentiodynamic polarization and electrochemical impedance spectroscopy (EIS) tests were conducted in a 3.5% NaCl aqueous solution. Microstructural examination showed that the coating formed at pH 9 has greater uniformity than the other coatings. Additionally, under this condition, the highest weight percentage of reactive elements (La and Ce) was present in the coating. The Tafel polarization test results demonstrated that applying the composite coating significantly reduces the corrosion current density of the uncoated sample. The positive effect of the coating on increasing the corrosion resistance of the steel is particularly significant for the coating formed at pH 9. In this case, the corrosion current density was reduced by more than 20 times (from 17.35 $\mu A \cdot cm^{-2}$ to 0.8 $\mu A \cdot cm^{-2}$) compared to the uncoated sample. The results obtained from electrochemical impedance spectroscopy (EIS) further support these findings. According to the EIS data, the charge transfer resistance for the uncoated sample was 4089 $\Omega \cdot cm^2$, while applying coatings at pH levels of 8, 8.5, 9, 9.5, and 10 increased the charge transfer resistance to 13,214, 19,840, 28,318, 17,060, and 9446 $\Omega \cdot cm^2$, respectively.

https://doi.org/10.30501/acp.2024.478445.1163

1. INTRODUCTION

430 stainless steel, containing 16-18% chromium, has a relatively low carbon content (0.12% C) and a ferritic matrix (Mosavi & Ebrahimifar, 2020). Chromium is the most important alloying element that protects stainless steels from oxidation and corrosion. The oxidation and corrosion resistance of these steels increases with higher chromium content (Yu et al., 2018).

Due to high nickel prices, there is a trend to switch from austenitic to ferritic stainless steels; however, ferritic stainless steels offer weaker mechanical and corrosion resistance properties compared to austenitic stainless steels because of their relatively weaker ferritic matrix, which somewhat limits their applications. Surface modification and deposition of a protective film or coating on these steels can expand their desirable properties and, consequently, their range of applications (Amin et al., 2016; Chen et al., 2022).

Composite coatings containing nickel and cobalt are among the most widely used coatings (Elkhoshkhany et al., 2017). Electroless and electroplating are two common methods for applying these coatings on metal surfaces.

Please cite this article as: Soleimani Roodi, K., Ebrahimifar, H. & Mohsenifar, F. (2024). Effect of pH of the Electroless Bath on Microstructure and Corrosion Behavior of Ni-Co-La2O3-CeO2 Coating, *Advanced Ceramics Progress*, 10(2), 9-16. https://doi.org/10.30501/acp.2024.478445.1163

Electroless technology, invented in 1946, is a chemical deposition method in which there is no external current, and the required electrons are provided by a chemical reaction in the solution (Kumar et al., 2020; Pancrecious et al., 2018). Electroless nickel coatings have a wide range of industrial applications due to their unique properties, such as excellent adhesion to the substrate, uniform thickness, high hardness, and wear resistance. Additionally, they exhibit higher hardness, wear, and corrosion resistance than those obtained by electroplating, though they are more brittle (Chintada et al., 2021; Fayomi et al., 2019). Nickel coatings alone have low corrosion resistance, hardness, and wear resistance. To address this limitation and improve corrosion properties, it is preferable to simultaneously deposit a second phase (Algailani et al., 2020; Saravanan et al., 2020; Shahbaznejad & Ebrahimifar, 2021). Oxides of reactive elements, such as ZrO_2, Y_2O_3, and CeO_2, increase the adhesion of the coating to the metal substrate and improve its corrosion resistance (Exbrayat et al., 2017; Shajahan & Basu, 2020; Wang et al., 2017; Wu et al., 2023).

The microstructure and final properties of the coating depend on many parameters. Factors such as the concentration of particles in the plating bath and the pH of the plating solution affect the amount of particles in the coating, morphology, mechanical properties, and corrosion behavior. Other effective parameters in electroless plating include bath temperature, plating time, and the presence of various additives (Deepthi & Krishna, 2018; Mousavi Anijdan et al., 2018; Sarkar et al., 2018; Shozib et al., 2021).

This study aimed to investigate the effect of pH on the microstructure and corrosion behavior of the Ni-Co-La_2O_3-CeO_2 composite coating deposited on AISI 430 stainless steel. A scanning electron microscope (SEM) was used to observe the morphology of the coatings. Potentiodynamic polarization and electrochemical impedance spectroscopy were employed to investigate the corrosion behavior of these coatings. For the first time, this work studied the effect of temperature on the microstructure and corrosion behavior of this iron-based composite coating.

2. MATERIALS AND METHODS

In this study, AISI 430 stainless steel was used as the substrate. Table 1 shows the chemical composition of this steel.

TABLE 1. Chemical composition of AISI 430 steel

Element	P	S	Si	Mn	Cr	C	Fe
wt%	0.03	0.02	0.85	0.92	17.4	0.12	Bal

Pieces of steel with dimensions of 10 mm × 10 mm × 3 mm were cut and then polished with sandpaper grits of 200, 500, 800, 1000, 2000, and 2500. To degrease, the samples were first washed with a soapy water solution and then rinsed with acetone. For surface preparation, each sample was initially placed in a phosphoric acid solution with a current density of 1 $A \cdot cm^{-2}$ for 3 minutes. The samples were then washed with distilled water and activated in a solution of 25% hydrochloric acid and 5% nitric acid for one minute, followed by another wash with distilled water. Each component in the bath plays one or more roles in the plating operation: nickel sulfate supplies nickel ions, cobalt sulfate provides cobalt ions, sodium hypophosphite acts as the reducing agent, sodium citrate serves as the complexing agent, ammonium chloride functions as the buffer, and lanthanum and cerium oxides provide the oxide phase in the plating bath. Table 2 shows the composition of the electroless plating bath. A dilute solution of sodium hydroxide and sulfuric acid was used to adjust the pH before and during the electroless process. After the plating process was completed, the samples were washed with distilled water and dried. To investigate the effect of pH on the microstructure and corrosion behavior of the coating, electroless plating was performed at various pH levels of 8, 8.5, 9, 9.5, and 10.

TABLE 2. Chemical composition of the electroless bath of Ni-Co-La_2O_3-CeO_2 coating

Material	Concentration (g/L)
Cobalt(II) sulfate ($CoSO_4$)	20
Nickel(II) sulfate ($NiSO_4$)	50
Cerium(IV) oxide (CeO_2)	10
Lanthanum oxide (La_2O_3)	10
Sodium hypophosphite ($NaPO_2H_2$)	6
Ammonium chloride (NH_4Cl)	50
Trisodium citrate ($Na_3C_6H_5O_7$)	70

A Cam Scan MV 2300 scanning electron microscope equipped with an EDS analyzer was used to investigate the microstructure of the samples. X-ray diffraction (XRD) was also carried out using a Philips X'Pert High Score diffractometer with Cu Kα radiation (λ = 1.5405 Å) to identify the phases present in the coated samples. Before any electrochemical test (potentiodynamic polarization and electrochemical impedance spectroscopy), each sample was connected to a copper wire and then mounted with epoxy resin. These electrochemical experiments were performed in a distilled water solution containing 3.5% NaCl (Merck) at ambient temperature using an EG&G Princeton Applied Research PARSTAT 2273 potentiostat/galvanostat Model 273A. The samples were immersed in the solution for 60 minutes to achieve a stable state. A commonly used three-electrode setup was employed, consisting of a working electrode (coated or uncoated sample), a saturated calomel electrode (SCE) as the reference electrode, and a platinum rod as the counter electrode (Figure 1). In the potentiodynamic polarization test, polarization was performed from the corrosion potential at a sweep rate of 1 $mV \cdot s^{-1}$ in the anodic and cathodic

directions. Before EIS measurements, all test samples were placed in the test solution for 30 minutes to stabilize. EIS measurements were recorded at the corrosion potential (E_{corr}) and in the frequency range of 10^{-2} to 10^{5} Hz. The AC amplitude used for the experiments was 10 mV. The exposed surface area was 1 cm^2. Princeton Applied Research PowerSuite 2.58 software was used to extract electrochemical data. The extracted potentiodynamic polarization and EIS data were then analyzed using Corrview 3.3 and Zview 3.1 software, respectively.

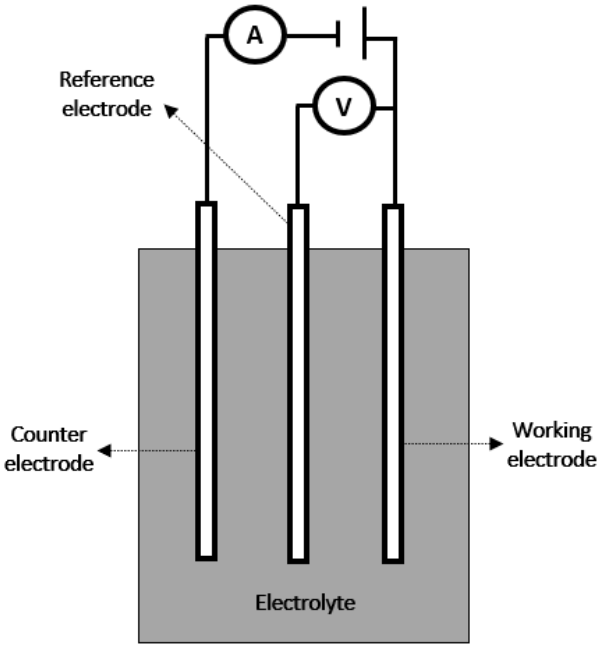

Figure 1. Simple schematic diagram of 3-electrode cell configuration used for the electrochemical investigations

3. RESULTS AND DISCUSSION

To investigate the effect of pH on the morphology and deposition rate of Ni-Co-La_2O_3-CeO_2 coating on AISI 430 stainless steel, coatings were applied at different plating bath pHs of 8, 8.5, 9, 9.5, and 10. Table 3 shows the chemical analysis of these coatings at different pH levels. Figure 2 shows the SEM images of the coatings formed at different pHs at two magnifications (1000x and 2000x).

As shown in Table 3, the amounts of nickel, cobalt, lanthanum oxide, and cerium oxide vary at different pHs. There are no substrate elements at pH = 8, but according to images A1 and A2, which correspond to this pH, oxide particles are dispersed on the surface of the coating. At pH = 8.5, only a small amount of nickel and lanthanum oxide have been deposited on the steel, with the remaining composition being iron. This is consistent with images B1 and B2, which confirm that no coating was formed on the steel surface. As the pH increases to 9, the percentage of coating elements increases, while the percentage of substrate elements decreases. In images C1 and C2, a uniform coating is observed. At pH = 9.5, according to images D1 and D2, a uniform coating has been created, and there is no trace of the substrate in this coating. The amount of lanthanum oxide in this coating is 73.3% by weight, although no cerium oxide was detected. At pH = 10, no coating was formed on the substrate, as indicated by the visible substrate preparation lines in images E1 and E2.

TABLE 3. EDS analysis data for Ni-Co-La_2O_3-CeO_2 coating at different plating bath pHs

	pH=8	pH=8.5	pH=9	pH=9.5	pH=10
Ni (wt%)	63.18	9.23	48.24	58.88	-
Co (wt%)	20.23	-	30.18	28.86	-
La (wt%)	1.48	5.14	8.09	3.73	0.15
Ce (wt%)	1.45	-	2.09	-	-
O (wt%)	4.19	12.39	9.25	6.57	8.82
P (wt%)	1.49	1.15	2.16	1.97	-
Cr (wt%)	-	-	-	-	15.85
Fe (wt%)	-	72.09	-	-	75.17

In the electroless process, H^+ ions are constantly formed, and the pH of the bath must be continuously controlled. There are different theories regarding the effect of pH on the deposition rate of solid particles in the coating. According to Table 3, as the pH of the plating bath increases, the deposition rate of cerium oxide and lanthanum oxide particles first increases and then decreases. With increasing pH, more adsorption sites are occupied by nickel ions, which reduces the adsorption of hydrogen ions on the surface of the particles, thereby increasing the percentage of particles in the coating. Additionally, as pH increases, the roughness of the coating surface increases (Ansari et al., 2017; Imanian Ghazanlou et al., 2018; Julka et al., 2016; Sadeghi & Ebrahimifar, 2021).

Most materials exhibit a zeta potential when placed in an aqueous environment, and this potential is influenced by the pH and ionic strength of the environment. This potential can serve as a criterion for the stability of the suspension. As the pH decreases, ionization causes a reduction in hydroxide ions, making the surface more positive. Conversely, as pH increases, the surface of the particles becomes more negative (Bhattacharjee, 2016). With increasing pH, the zeta potential becomes more negative. In this case, particles with a more negative charge move faster toward the cathode. The repulsive force increases with the rising surface charge of the particles, preventing their agglomeration. Consequently, the stability of the bath improves (Loosli & Stoll, 2017). In the Ni-Co-La_2O_3-CeO_2 coating at pH = 9, both the rate and amount of particle deposition increased. At pH values above 9, the bath became highly unstable, resulting in a decrease in the deposition rate of particles.

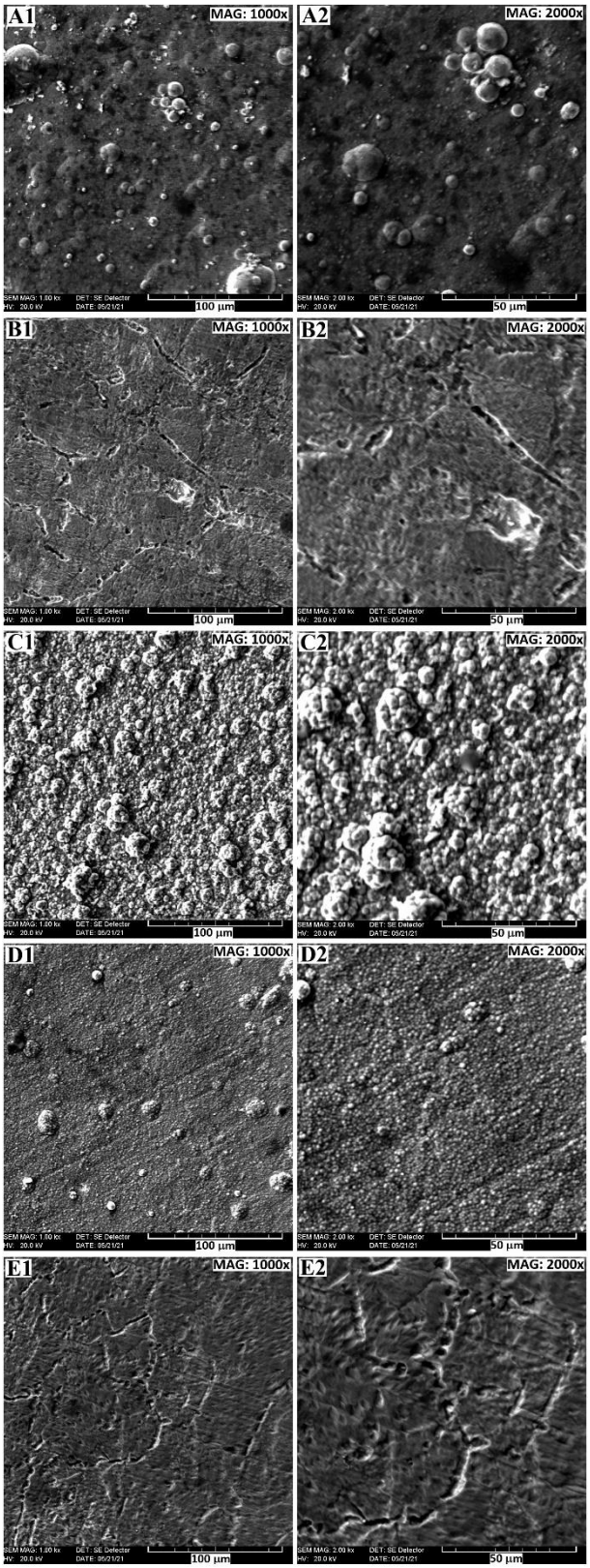

Figure 2. SEM micrographs of the as-coated samples at pH 8 (A1 and A2), pH 8.5 (B1 and B2), pH 9 (C1 and C2), pH 9.5 (D1 and D2), and pH 10 (E1 and E2), respectively.

Figure 3 depicts the results of the XRD analysis of the coated samples. The results revealed that the coatings formed at pH = 8 and pH = 9 consist of phases of cobalt (JCPDS No. 01-1254), nickel (JCPDS No. 04-0850), lanthanum oxide (JCPDS No. 02-0688), and cerium oxide (JCPDS No. 34-0394). The presence of sharper peaks for La_2O_3 and CeO_2 at pH = 9, compared to pH = 8, indicates a higher percentage of these particles in the coating. The presence of substrate peaks (JCPDS No. 87-0721) in the spectrum for coatings formed at pH = 8.5 and pH = 10 indicates the incoherence and non-uniformity of the coatings under these conditions. These results align with the EDS findings.

Figures 4a and 4b show the microscopic image of the cross-sectional view and the corresponding line scan analysis of the Ni-Co-La_2O_3-CeO_2 coating at pH = 9, respectively. The thickness of this monolayer composite coating is approximately 21.7 µm. The line scan analysis confirmed the presence of Ni, Co, and ceramic particles (La_2O_3 and CeO_2) in the coating. The presence of O, La, and Ce throughout the composite coating thickness confirmed the proper distribution of ceramic particles in this coating.

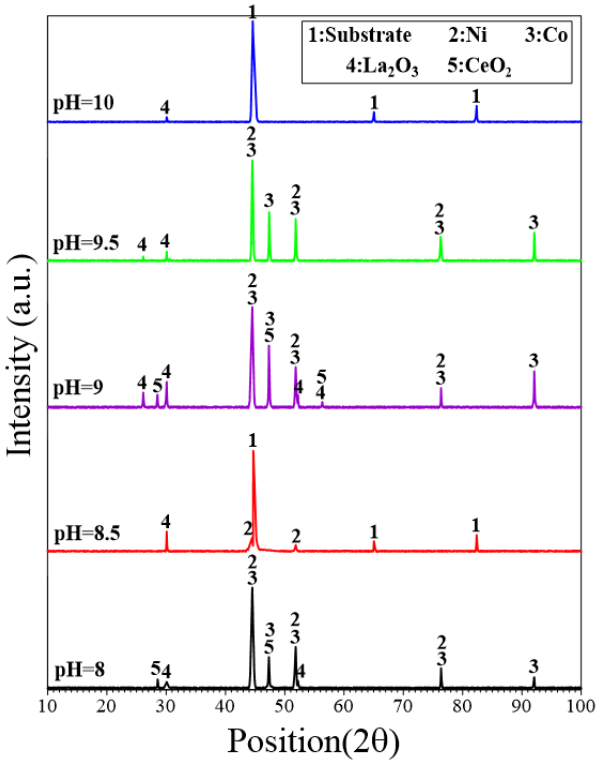

Figure 3. X-ray diffraction patterns of the samples coated at different pHs.

The potentiodynamic polarization curves of the samples coated at different pH values in a 3.5% sodium chloride solution are shown in Figure 5. The data from these curves were analyzed using Corrview software, and the results are presented in Table 4. The Stern-Geary

relationship (Equation 1) was used to calculate the polarization resistance.

$$R_p = \frac{\beta_a \beta_c}{2.303 i_{corr}(\beta_a + \beta_c)} \quad (1)$$

where R_p is the polarization resistance, i_{corr} is the corrosion current density, and β_c and β_a are the slopes of the cathodic and anodic regions of the Tafel curve, respectively (García-Galvan et al., 2021; Goyal et al., 2019; Surani-Yancheshmeh & Ghorbani, 2024). The results indicated that the coating created at pH 9 has the highest polarization resistance (41,064 Ω) and the lowest corrosion current density (0.8 μA·cm^{-2}), resulting in higher corrosion resistance for the coating formed at this pH. With an increase in pH from 9 to 9.5, the polarization resistance decreased sharply, indicating a decrease in corrosion resistance in this case. The significant increase in current density for the coatings formed at pH 8 and pH 10 is due to the lack of formation of a uniform coating on the surface of the substrate.

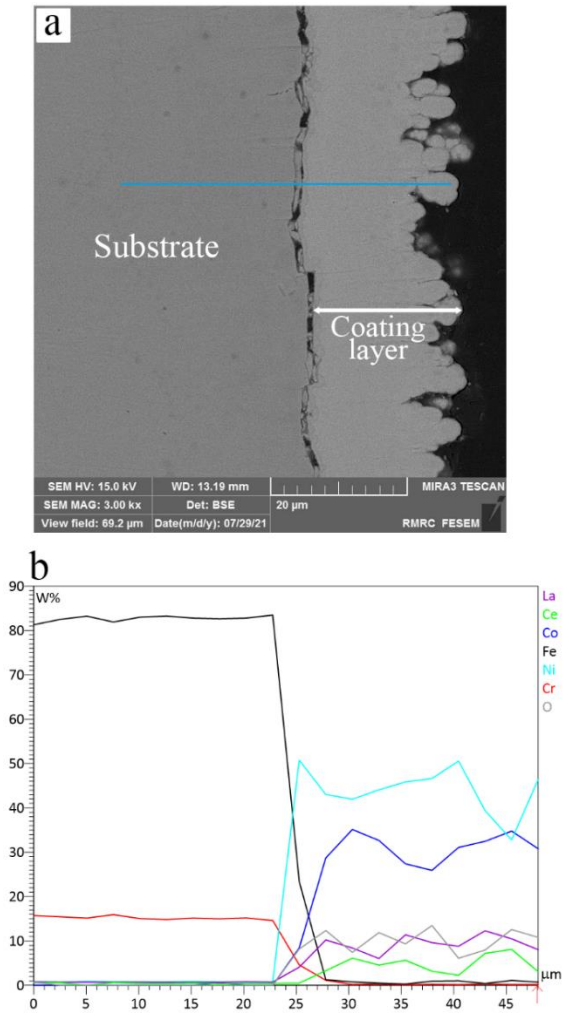

Figure 4. (a) FESEM cross-section micrograph and (b) EDS line scan of the coated sample at pH 9

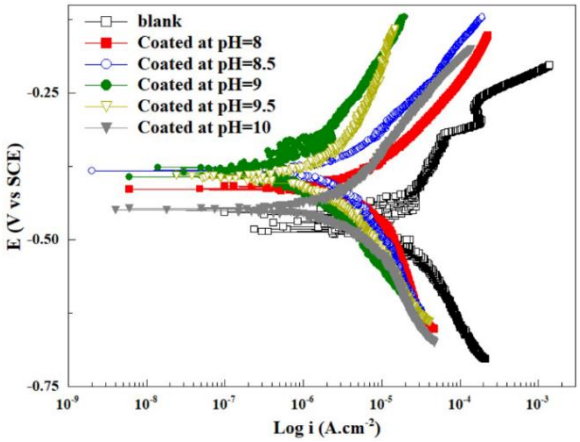

Figure 5. Potentiodynamic polarization curves for Ni-Co-La_2O_3-CeO_2 coating at different pHs

The improvement in the corrosion resistance of the coating deposited at pH 9 can be attributed to the higher concentration of oxide particles (La_2O_3 and CeO_2) present in this coating. In contrast, the corrosion current density for coatings formed at other pH levels is higher due to the lower amount of oxide particles. The uniform distribution of these particles in the coating results in the creation of many galvanic microcells (Shozib et al., 2022). Ceramic particles have higher corrosion resistance and a nobler corrosion potential than the matrix, so these particles act as the cathode while the surrounding matrix serves as the anode. The formation of these galvanic microcells uniformizes the distribution of corrosion current on the coating surface, reducing localized corrosion (Zadeh et al., 2016). Therefore, increasing the concentration and distribution of these particles within the coating shifts the corrosion mechanism from localized corrosion to uniform corrosion (Makarava et al., 2022).

TABLE 4. Electrochemical data derived from potentiodynamic polarization curves of uncoated and coated samples

Sample	blank	Coated at pH=8	Coated at pH=8.5	Coated at pH=9	Coated at pH=9.5	Coated at pH=10
E_{corr} (mV)	-461	-396	-391	-372	-397	-418
i_{corr} (μA.cm^{-2})	17.35	6.05	2.51	0.8	2.04	4.21
β_c (mV.dec^{-1})	229	279.1	165.8	152.2	176.8	265.9
β_a (mV.dec^{-1})	229.3	125.6	132.1	150.4	257.1	175.2
R_p (Ω.cm^2)	2867	6219	12721	41064	22298	10894

The Nyquist curves obtained from electrochemical impedance tests for the uncoated sample and samples coated at pH levels 8, 8.5, 9, 9.5, and 10 are shown in Figure 6. Figures 7a and 7b display the Bode and Bode-

phase diagrams for the tested samples, respectively. As seen, the Bode-phase vs. frequency plots show two distinct peaks for the coated samples. This suggests that the corrosion process of the coated samples can be described by two-time constants, confirmed by the presence of two loops in the Nyquist plots. The first time constant, related to high frequencies, is attributed to the coating/electrolyte interface, while the second, associated with low frequencies, refers to the substrate/electrolyte interface conditions. In contrast, the uncoated sample shows only one-time constant at low frequencies, indicative of the substrate's corrosion process (Kaveh et al., 2023). All EIS curves were plotted in the frequency range of 0.01 Hz to 100 KHz. Data from these diagrams were extracted using Powersuite software and imported into Zview software for analysis. The equivalent circuit proposed by the software for the samples is shown in Figure 8, where R_s represents the solution resistance between the reference electrode and the samples, R_{ct} the charge transfer resistance of the substrate, R_{coat} the resistance of the coating to the penetration of the corrosive environment, and CPE the constant phase element used instead of the simple capacitor. CPE for the double layer and coating are represented as CPE_{dl} and CPE_{coat}, respectively. The constant phase element is used in place of an ideal capacitor to account for the roughness of the electrode surface, heterogeneous reactions, and uneven current distribution during the corrosion process (Xia et al., 2022).

The constant phase element consists of two components: admittance (CPE-T) and power index (CPE-P). The power index ranges between 0.5 and 1, with greater deviation from 1 indicating more inhomogeneity and surface roughness (Dhillon & Kant, 2017; Murariu et al., 2017; Onyeji et al., 2018). The deviation of the Nyquist curve shape from a semicircle indicates surface roughness and non-uniformity during the corrosion process. The results from the EIS curve analysis in Zview software are presented in Table 5. Higher admittance values indicate more porosity in the coating.

Admittance has its lowest value at pH 9, suggesting that the coating's protective properties are best at this pH. As pH increases from 9 to 9.5, admittance values rise, and consequently, corrosion resistance decreases.

The higher solution resistance (25.2 Ω·cm²) at pH 9 could be due to the more effective formation of the composite coating at this pH. Additionally, the double layer capacitance for the coating formed at this pH is lower than in other cases, indicating less corrosive solution penetration to the metal/coating interface (Pajkossy & Jurczakowski, 2017; Ryl et al., 2019; Shanaghi et al., 2023). These results are in complete agreement with the results obtained from Tafel polarization.

One of the most important parameters obtained from the impedance analysis is the charge transfer resistance. This parameter serves as a criterion for the corrosion rate under the coating for the coated samples. An increase in this resistance indicates a decrease in the transfer of aggressive ions through the coating to the surface of the substrate. The value of this parameter is higher for the sample coated at pH = 9 than for the other samples. This can be attributed to the higher percentage of oxide particles in this coating. In fact, the inert properties of these particles increase the charge transfer resistance, and by blocking the charge transfer sites and passivating the surface, they act as a deterrent against aggressive ions. Therefore, these particles force the aggressive ions to move in zigzag paths toward the surface of the substrate, consequently, access to the substrate by the aggressive ions becomes more difficult.

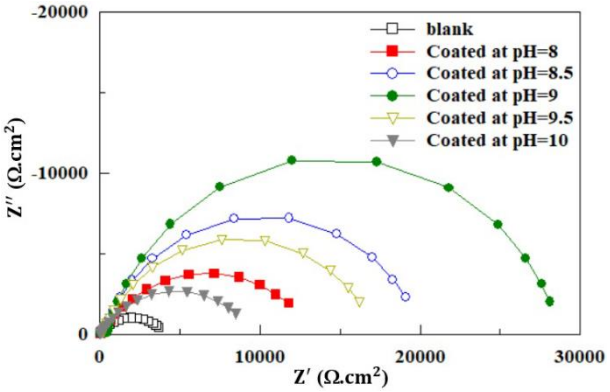

Figure 6. Nyquist curves for Ni-Co-La_2O_3-CeO_2 coating at different pHs

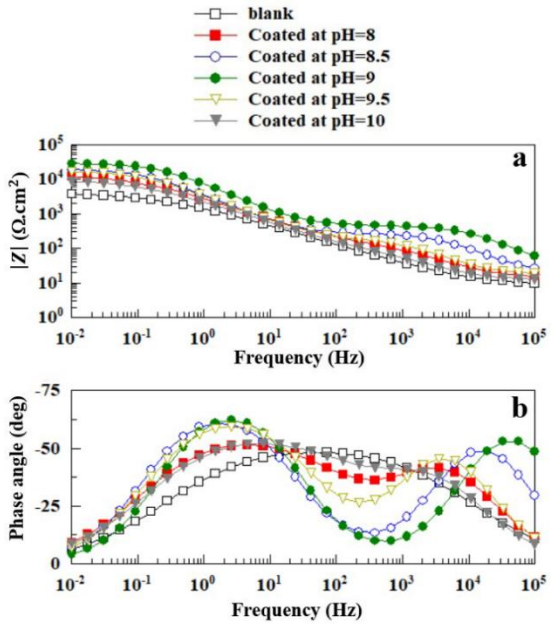

Figure 7. (a) Bode and (b) Bode-phase curves for Ni-Co-La_2O_3-CeO_2 coating at different pHs

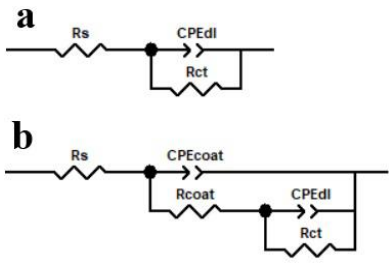

Figure 8. Equivalent electrical circuit used for the (a) uncoated and (b) coated samples

TABLE 5. Electrochemical data derived from impedance curves of uncoated and coated samples

	blank	Coated at pH=8	Coated at pH=8.5	Coated at pH=9	Coated at pH=9.5	Coated at pH=10
R_s ($\Omega.cm^2$)	8.23	14.2	19.4	25.2	17.5	11.7
R_{ct} ($\Omega.cm^2$)	4089	13214	19840	28318	17060	9446
CPE-$T_{dl}\times10^6$ ($\Omega^{-1}.cm^{-2}.S^n$)	190	88.7	62.5	27.4	65.5	98.4
CPE-P_{dl} ($\Omega^{-1}.cm^{-2}.S^n$)	0.58	0.65	0.81	0.84	0.77	0.63
R_{coat} ($\Omega.cm^2$)	-	137	247	429	177	102
CPE-$T_{coat}\times10^6$ ($\Omega^{-1}.cm^{-2}.S^n$)	-	10.2	80.6	0.186	3.62	25.4
CPE-P_{coat} ($\Omega^{-1}.cm^{-2}.S^n$)	-	0.77	0.854	0.87	0.84	0.74

4. CONCLUSION(S)

AISI 430 stainless steel was coated with electroless Ni-Co-La_2O_3-CeO_2 coating. The effect of plating bath pH on the microstructure and corrosion resistance of the formed coatings was investigated. The results showed that the Ni-Co-La_2O_3-CeO_2 deposit obtained in a bath with pH = 9 was uniform. Moreover, the coating formed at this pH had the highest amount of oxide particles compared to the other coatings.

The results of the potentiodynamic polarization test in 3.5 wt% NaCl aqueous solution showed that the sample coated in a bath with pH = 9 had the highest charge transfer resistance (41062 $\Omega.cm^2$) compared to the uncoated (2867 $\Omega.cm^2$), coated samples at pH=8 (6219 $\Omega.cm^2$), pH=8.5 (12721 $\Omega.cm^2$), pH=9.5 (22298 $\Omega.cm^2$) and pH=10 (10894 $\Omega.cm^2$).

ACKNOWLEDGEMENT

The authors would like to acknowledge Shahid Bahonar University of Kerman for all supports throughout this research.

REFRENCES

1. Algailani, H., Mahmoud, A., & Al-Kaisy, H. (2020). Fabrication of Ni-ZrO_2 nanocomposite coating by electroless deposition technique. *Engineering and Technology Journal*, *38*(5). https://doi.org/10.30684/etj.v38i5a.491
2. Amin, M. A., Saracoglu, M., El-Bagoury, N., Sharshar, T., Ibrahim, M. M., Wysocka, J., Krakowiak, S., & Ryl, J. (2016). Microstructure and corrosion behaviour of carbon steel and ferritic and austenitic stainless steels in NaCl solutions and the effect of p-nitrophenyl phosphate disodium salt. *International Journal of Electrochemical Science*, *11*(12). https://doi.org/10.20964/2016.12.17
3. Ansari, M. I., Julka, S., & Thakur, D. G. (2017). Enhancement of surface properties with influence of bath pH on electroless Ni-P-ZnO/Al_2O_3 nano-composite deposits for defence applications. *Journal of Molecular Liquids*, *247*. https://doi.org/10.1016/j.molliq.2017.09.030
4. Bhattacharjee, S. (2016). DLS and zeta potential - What they are and what they are not? In *Journal of Controlled Release*. 235. https://doi.org/10.1016/j.jconrel.2016.06.017
5. Chen, K., Wang, J., Zhang, L., Wang, H., An, X., Li, Y., Zhang, J., Shen, Z., & Zeng, X. (2022). A high-resolution study of the different surface state effects on the corrosion behaviors of a ferritic steel and an austenitic steel in supercritical water. *Corrosion Science*, *209*. https://doi.org/10.1016/j.corsci.2022.110757
6. Chintada, V. B., Koona, R., & Raju Bahubalendruni, M. V. A. (2021). State of art review on nickel-based electroless coatings and materials. In *Journal of Bio- and Tribo-Corrosion*. *7(4)*. https://doi.org/10.1007/s40735-021-00568-7
7. Deepthi, Y. P., & Krishna, M. (2018). Optimization of electroless copper coating parameters on graphite particles using taguchi and grey relational analysis. *Materials Today: Proceedings*, *5(5)*. https://doi.org/10.1016/j.matpr.2018.02.183
8. Dhillon, S., & Kant, R. (2017). Theory for electrochemical impedance spectroscopy of heterogeneous electrode with distributed capacitance and charge transfer resistance. *Journal of Chemical Sciences*, *129*(8). https://doi.org/10.1007/s12039-017-1335-x
9. Elkhoshkhany, N., Hafnway, A., & Khaled, A. (2017). Electrodeposition and corrosion behavior of nano-structured Ni-WC and Ni-Co-WC composite coating. *Journal of Alloys and Compounds*, *695*. https://doi.org/10.1016/j.jallcom.2016.10.290
10. Exbrayat, L., Rébéré, C., Ndong Eyame, R., Steyer, P., & Creus, J. (2017). Corrosion behaviour in saline solution of pulsed-electrodeposited zinc-nickel-ceria nanocomposite coatings. *Materials and Corrosion*, *68*(10). https://doi.org/10.1002/maco.201709419
11. Fayomi, O. S. I., Akande, I. G., & Sode, A. A. (2019). Corrosion prevention of metals via electroless nickel coating: A review. *Journal of Physics: Conference Series*, *1378*(2). https://doi.org/10.1088/1742-6596/1378/2/022063
12. García-Galvan, F. R., Fajardo, S., Barranco, V., & Feliu, S. (2021). Experimental apparent stern–geary coefficients for AZ31B Mg alloy in physiological body fluids for accurate corrosion rate determination. *Metals*, *11*(3). https://doi.org/10.3390/met11030391
13. Goyal, A., Pouya, H. S., Ganjian, E., Olubanwo, A. O., & Khorami, M. (2019). Predicting the corrosion rate of steel in cathodically protected concrete using potential shift. *Construction and Building Materials*, *194*. https://doi.org/10.1016/j.conbuildmat.2018.10.153
14. Imanian Ghazanlou, S., Farhood, A. H. S., Hosouli, S., Ahmadiyeh, S., & Rasooli, A. (2018). Pulse and direct electrodeposition of Ni–Co/micro and nanosized SiO_2 particles. *Materials and Manufacturing Processes*, *33*(10). https://doi.org/10.1080/10426914.2017.1364748

15. Julka, S., Ansari, M. I., & Thakur, D. G. (2016). Effect of pH on mechanical, physical and tribological properties of electroless Ni-P-Al_2O_3 composite deposits for marine applications. *Journal of Marine Science and Application*, *15*(4). https://doi.org/10.1007/s11804-016-1385-3

16. Kaveh, M., Sajjadnejad, M., Mohassel, A., & Setoudeh, N. (2023). Influence of B_4C nanoparticles on corrosion characteristics of Ni matrix nanocomposite coatings fabricated via pulse electroplating technique. *Advanced Ceramics Progress*, *9(3)*, 16-30. https://doi.org/10.30501/acp.2024.429141.1141

17. Kumar, S., Banerjee, T., & Patel, D. (2020). Tribological characteristics of electroless multilayer coating: A review. *Materials Today: Proceedings*, *33*. https://doi.org/10.1016/j.matpr.2020.04.207

18. Loosli, F., & Stoll, S. (2017). Effect of surfactants, pH and water hardness on the surface properties and agglomeration behavior of engineered TiO_2 nanoparticles. *Environmental Science: Nano*, *4*(1). https://doi.org/10.1039/c6en00339g

19. Makarava, I., Esmaeili, M., Kharytonau, D. S., Pelcastre, L., Ryl, J., Bilesan, M. R., Vuorinen, E., & Repo, E. (2022). Influence of CeO_2 and TiO_2 particles on physicochemical properties of composite nickel coatings electrodeposited at ambient temperature. *Materials*, *15*(16). https://doi.org/10.3390/ma15165550

20. Mosavi, A., & Ebrahimifar, H. (2020). Investigation of oxidation and electrical behavior of AISI 430 steel coated with Mn–Co–CeO_2 composite. *International Journal of Hydrogen Energy*, *45*(4). https://doi.org/10.1016/j.ijhydene.2019.11.183

21. Mousavi Anijdan, S. H., Sabzi, M., Zadeh, M. R., & Farzam, M. (2018). The effect of electroless bath parameters and heat treatment on the properties of Ni-P and Ni-P-Cu composite coatings. *Materials Research*, *21*(2). https://doi.org/10.1590/1980-5373-MR-2017-0973

22. Murariu, A. C., Pleșu, N., Perianu, I. A., & Tară-Lungă-Mihali, M. (2017). Investigations on corrosion behaviour of WC-CrC-Ni coatings deposited by HVOF thermal spraying process. *International Journal of Electrochemical Science*, *12*(2). https://doi.org/10.20964/2017.02.60

23. Onyeji, L., Mohammed, S., & Kale, G. (2018). Electrochemical response of micro-alloyed steel under potentiostatic polarization in CO_2 saturated brine. *Corrosion Science*, *138*. https://doi.org/10.1016/j.corsci.2018.04.001

24. Pajkossy, T., & Jurczakowski, R. (2017). Electrochemical impedance spectroscopy in interfacial studies. In *Current Opinion in Electrochemistry*. *1(1).* https://doi.org/10.1016/j.coelec.2017.01.006

25. Pancrecious, J. K., Ulaeto, S. B., Ramya, R., Rajan, T. P. D., & Pai, B. C. (2018). Metallic composite coatings by electroless technique–a critical review. In *International Materials Reviews*. *63(8).* https://doi.org/10.1080/09506608.2018.1506692

26. Ryl, J., Burczyk, L., Zielinski, A., Ficek, M., Franczak, A., Bogdanowicz, R., & Darowicki, K. (2019). Heterogeneous oxidation of highly boron-doped diamond electrodes and its influence on the surface distribution of electrochemical activity. *Electrochimica Acta*, *297*. https://doi.org/10.1016/j.electacta.2018.12.050

27. Sadeghi, S., & Ebrahimifar, H. (2021). Effect of electrolyte pH on microstructure, corrosion behavior, and mechanical behavior of Ni-P-W-TiO_2 electroplated coatings. *Journal of Materials Engineering and Performance*, 30(4). https://doi.org/10.1007/s11665-021-05462-4

28. Saravanan, I., Elayaperumal, A., Devaraju, A., Karthikeyan, M., & Raji, A. (2020). Wear behaviour of electroless Ni-P and Ni-P-TiO_2 composite coatings on En8 steel. *Materials Today: Proceedings*, *22*. https://doi.org/10.1016/j.matpr.2019.12.007

29. Sarkar, S., Baranwal, R. K., Banerjee, S., Prakash, A., Mandal, R., & Majumdar, G. (2018). Parametric optimization of process parameters on the response of microhardness of electroless Ni-P coating. *Journal of Molecular and Engineering Materials*, *06*(01n02). https://doi.org/10.1142/s225123731850003x

30. Shahbaznejad, H., & Ebrahimifar, H. (2021). A study on the oxidation and electrical behavior of crofer 22 APU solid oxide fuel cell interconnects with Ni-Co-CeO_2 composite coating. *Journal of Materials Science: Materials in Electronics*, 32(6). https://doi.org/10.1007/s10854-021-05470-z

31. Shajahan, S., & Basu, A. (2020). Corrosion, oxidation and wear study of electro-co-deposited ZrO_2-TiO_2 reinforced Ni-W coatings. *Surface and Coatings Technology*, *393*. https://doi.org/10.1016/j.surfcoat.2020.125729

32. Shanaghi, A., Souri, A. R., & Forghani, W. (2023). Comparative study of anodized titanium surfaces: The effect of low voltage on the morphology, performance, and corrosion resistance of the double layer. *Advanced Ceramics Progress*, 9(2), 1-7. https://doi.org/10.30501/acp.2023.383589.1116

33. Shozib, I. A., Ahmad, A., Abdul-Rani, A. M., Beheshti, M., & Aliyu, A. A. (2022). A review on the corrosion resistance of electroless Ni-P based composite coatings and electrochemical corrosion testing methods. In *Corrosion Reviews* (Vol. 40, Issue 1). https://doi.org/10.1515/corrrev-2020-0091

34. Shozib, I. A., Ahmad, A., Rahaman, M. S. A., Abdul-Rani, A. M., Alam, M. A., Beheshti, M., & Taufiqurrahman, I. (2021). Modelling and optimization of microhardness of electroless Ni-P-TiO_2 composite coating based on machine learning approaches and RSM. *Journal of Materials Research and Technology*, *12*. https://doi.org/10.1016/j.jmrt.2021.03.063

35. Surani-Yancheshmeh, H., & Ghorbani, M. (2024). Corrosion studies on pulse reverse Ni–Mo coatings electrodeposited on Cu substrate. *Electrochimica Acta*, *478*. https://doi.org/10.1016/j.electacta.2024.143828

36. Wang, L., Chen, M., Liu, H., Jiang, C., Ji, V., & Moreira, F. (2017). Optimisation of microstructure and corrosion resistance of Ni-Ti composite coatings by the addition of CeO_2 nanoparticles. *Surface and Coatings Technology*, *331*. https://doi.org/10.1016/j.surfcoat.2017.10.049

37. Wu, T., Ma, M., Ding, K., Nan, X., Wang, Z., Wei, X., & Zhu, X. (2023). Effect of Y_2O_3 nanoparticles on the microstructure and corrosion resistance of electrodeposited Ni-Mo-Y_2O_3 nanocomposite coatings. *International Journal of Electrochemical Science*, 18(6). https://doi.org/10.1016/J.IJOES.2023.100095

38. Xia, D. H., Deng, C. M., Macdonald, D., Jamali, S., Mills, D., Luo, J. L., Strebl, M. G., Amiri, M., Jin, W., Song, S., & Hu, W. (2022). Electrochemical measurements used for assessment of corrosion and protection of metallic materials in the field: A critical review. In *Journal of Materials Science and Technology 112*. https://doi.org/10.1016/j.jmst.2021.11.004

39. Yu, Y., Shironita, S., Souma, K., & Umeda, M. (2018). Effect of chromium content on the corrosion resistance of ferritic stainless steels in sulfuric acid solution. *Heliyon*, 4(11). https://doi.org/10.1016/j.heliyon.2018.e00958

40. Zadeh, K. M., Shakoor, R. A., & Bahgat Radwan, A. (2016). Structural and electrochemical properties of electrodeposited Ni-P nanocomposite coatings containing mixed ceramic oxide particles. *International Journal of Electrochemical Science*, *11*(8). https://doi.org/10.20964/2016.08.42

Advanced Ceramics Progress: Vol. 10, No. 2, (Spring 2024) 17-22

Materials and Energy Research Center
MERC

Contents lists available at ACERP

Advanced Ceramics Progress

Journal Homepage: www.acerp.ir

Original Research Article

Effects of Sintering Temperature on the Densification, Microstructure, and Micro-hardness of Intermetallic Ti-Cu Alloy Prepared through Mechanical Alloying and Microwave-assisted Sintering Method

Mohammad Reza Akbarpour [a,*], Fatemeh Sadat Torknik [b], Touraj Ebadzadeh [c]

[a] *Professor, Department of Materials Engineering, University of Maragheh, P.O. Box: 83111-55181, Maragheh, Iran.*
[b] *PhD, Department of Semiconductors, Materials and Energy Research Center, Karaj, Iran.*
[c] *Professor, Department of Ceramic, Materials and Energy Research Center, Karaj, Iran.*
* Corresponding Author Email: akbarpour@maragheh.ac.ir (M.R. Akbarpour) URL: https://www.acerp.ir/article_210129.html

ARTICLE INFO

Article History:
Received: 14 November 2023
Revised: 07 October 2024
Accepted: 25 November 2024

Keywords:
Mechanical Alloying,
Sintering,
Densification,
Ti-Cu Alloy

ABSTRACT

Microwave sintering has emerged as a promising technique for the fabrication of Ti-based alloys, offering unique advantages over conventional sintering methods. The selective and volumetric heating capabilities of microwaves can result in rapid densification, microstructural refinement, and enhanced properties in Ti-Cu alloy systems. Therefore, this study aimed to synthesize an intermetallic alloy of Ti-50 at. % Cu through high-energy mechanical milling and a microwave-assisted sintering method. The objective was to expedite the sintering process of the Ti-Cu alloy using microwave assistance and analyze how this method influences the phases formed and the properties of the alloy. A Ti-50 at. % Cu powder mixture was milled for 30 hours under an argon atmosphere, then uniaxially compacted to form green samples, which were subsequently sintered by microwave heating. This method allowed for rapid consolidation without significant grain growth within a short sintering period. The effects of the sintering method and temperature on microstructure and mechanical properties were studied. The density of the sintered samples increased with rising temperatures, with the highest density of 6.54 g/cm³ obtained at 900°C. Microstructural examination revealed that the Ti3Cu4 and TiCu phases primarily formed, with an average grain size of approximately 28 nm. A high micro-hardness of ~880 HV was achieved for the dense alloy prepared using this method.

https://doi.org/10.30501/acp.2024.425053.1138

1. INTRODUCTION

A number of outstanding characteristics, including light weight, high strength, low elastic moduli, biocompatibility, and corrosion resistance, have led titanium (Ti) and titanium-based alloys to find application in several biomedical fields (Mahmoudi et al., 2022; Moniri Javadhesari et al., 2019; Zhang et al., 2019). The Ti-Cu alloy is one of the fastest-growing alloys based on Ti. It has found application in dentistry and orthopedics as a promising material. The addition of Cu to Ti renders it harder, stronger, more wear-resistant, and enhances its bio-corrosion resistance, antibacterial activity, and biocompatibility (Akbarpour et al., 2022). Research has been conducted on binary Ti-Cu alloys with different Cu fractions over many years. Using various heat treatments, researchers have identified four intermetallic compounds in the Ti-Cu system: Ti_2Cu, TiCu, Ti_2Cu_3, and TiCu. The Ti_2Cu intermetallic compound is particularly important in Ti-rich alloys, on which numerous structural studies have been conducted (Alqattan et al., 2021; Kikuchi et al., 2003; Yuan et al., 2022). In recent years, it has been noted that the Ti-50

Please cite this article as: Akbarpour, M. R., Torknik, F. S. & Ebadzadeh, T. (2024). Effects of Sintering Temperature on the Densification, Microstructure, and Micro-hardness of Intermetallic Ti-Cu Alloy Prepared through Mechanical Alloying and Microwave-assisted Sintering Method, *Advanced Ceramics Progress*, 10(2), 17-22. https://doi.org/10.30501/acp.2024.425053.1138

at.% Cu alloy is being considered as a replacement for the conventional dental cast alloy Ti-Ag, which has a higher cost (Shon et al., 2010). Various methods such as casting, semi-solid processing, and powder metallurgy (PM) have been employed (Akbarpour et al., 2022). Despite casting being a common method of producing Ti-Cu alloys, it has some disadvantages, including undesirable segregation and challenges related to evaporation and oxidation (Liu et al., 2022; Moniri Javadhesari et al., 2020b). Powder metallurgy is a manufacturing technique used in many industries when lower processing temperatures are needed. By reducing both the processing temperature and time, this technique can effectively mitigate issues commonly encountered with casting. This technology involves blending, compacting, and sintering metal and ceramic powders. To fabricate dense components, conventional sintering of Ti-Cu alloys has been the focus of more research than other variations of PM. Zhang et al. investigated the eutectoid sintering of a blend of Ti and Cu powders (Zhang et al., 2019). During sintering, they observed flaky Ti2Cu precipitates forming at grain boundaries (β-sintering). As Cu content increases in Ti-Cu alloys, density increases accordingly due to the higher ductility and diffusion rates of the Cu powder (J. Liu et al., 2014). Shon et al. synthesized Ti-Cu alloy by high-frequency induction heating (HFIH) and investigated its mechanical and microstructural properties. They synthesized nanostructured TiCu powders through high-energy ball milling of micron-sized Ti and Cu powders. The consolidation of the milled powder was achieved using both induced and applied currents in their work. Several factors influence the structural properties, densification, and overall characteristics of Ti-Cu alloys prepared by the PM method, such as milling time (Akbarpour et al., 2016, 2020), Cu content (J. Liu et al., 2014) , and sintering method and temperature (Akbarpour et al., 2020, 2023; D. Zhang et al., 2019).

Akbarpour et al. prepared Ti-Cu alloy by conventional powder metallurgy and studied the effects of sintering temperature on the densification, hardness, and antibacterial activity of the alloy (Akbarpour et al., 2020). According to their results, the densest microstructure and highest densification of TiCu powders were achieved at a sintering temperature of 900 °C. A multi-phase structure consisting of TiCu and Ti2Cu3 phases with a high microhardness of 1000 HV was obtained for the Ti-50 at.% Cu alloy (Akbarpour et al., 2020). Studies on Ti-50 at.% Cu alloy have revealed an ultra-high hardness of 10 GPa, acceptable toughness, high antibacterial properties, excellent cell viability with MG-63 osteosarcoma cells, and a high osteoblast formation rate (Moniri Javadhesari et al., 2020a). Therefore, this alloy shows significant potential for use in biomedical applications due to its superior properties.

The sintering process plays a crucial role in determining the microstructural evolution, phase stability, and overall properties of the final Ti-Cu alloy product. Microwave sintering stands out as a particularly compelling method for the fabrication of Ti-based alloys, offering a unique set of advantages over traditional sintering techniques. The inherent ability of microwaves to selectively and volumetrically heat the material allows for rapid and uniform heating of alloys, overcoming the challenges posed by the low thermal conductivity of titanium. This selective heating mechanism leads to more efficient energy transfer and significantly reduced processing times compared to conventional methods. The rapid heating and cooling rates achievable with microwave sintering can also play a crucial role in the microstructural evolution of Ti-Cu alloys. The fast heating rates can suppress the formation of undesirable intermetallic phases, while the quick cooling minimizes the growth of detrimental microstructural features. This, in turn, results in a more homogeneous and stable microstructure, which directly translates to enhanced mechanical properties such as increased strength, hardness, and wear resistance. To date, microwave sintering of Ti-Cu alloys has not been extensively reported in the literature, presenting an opportunity for further research and development in this area. While the unique advantages of microwave-assisted processing have been well-documented for other metallic systems, the specific application of this technology to Ti-Cu alloys remains relatively unexplored.

In this research, the high-energy mechanical alloying and microwave-assisted sintering method are used to synthesize the Ti-50 at% Cu alloy. The effects of the microwave sintering method and the sintering temperature on the microstructure and mechanical properties of the alloy are investigated.

2. MATERIALS AND METHODS

This research used elemental copper powder with a particle size below 20 μm and a purity of 99.7%, as well as titanium powder with a particle size below 70 μm and a purity of 99.5%. A planetary ball mill (Retsch 400MA) was operated at 300 RPM for the milling of the Ti-50 at.% Cu powder mixture. The milling process was conducted in a high-chromium carbon steel vial with a ball-to-powder weight ratio (BPR) of 10:1 at room temperature for 30 hours. To accelerate the milling process, 0.5 wt.% stearic acid was added to the mixture. The processed powder was compacted at 1 GPa and then sintered by microwave heating at temperatures of 700 °C, 800 °C, and 900 °C under argon gas.

X-ray diffraction (XRD) was performed using a Philips diffractometer (CuKα radiation: λ = 0.154 nm) to determine the grain size. The average grain size and microstrain were calculated from the broadening of the XRD peaks using the Scherrer equation (Fernández et al., 2019). For analysis of powder morphology and the microstructure of sintered materials, scanning electron microscopes (SEMs, Philips XL30 and Mira3 XMU)

equipped with energy-dispersive spectroscopy (EDS) were used. Additionally, for precise microstructural analysis of the samples, transmission electron microscopy (TEM, FEG Philips CM200) was employed. A Vickers indenter (QV-1000DAT) was used to measure the microhardness of the samples at a load of 30 kg with a dwell period of 15 seconds.

3. RESULTS AND DISCUSSION

3.1. Morphology and microstructure of the mechanically-milled powder

The Ti-50 at. % Cu powder mixture was mechanically milled for 30 hours until the synthesis of the TiCu intermetallic phase. Figure 1a shows SEM micrographs of the 30-hour milled powder, where a relatively equiaxed and spherical morphology of the powder can be observed. Figure 1b presents a bright-field TEM micrograph of the milled material, revealing a fine-grained structure after 30 hours of milling. The mean grain size, obtained by the intercept method from the TEM micrographs, was approximately 8 nm. The XRD pattern of the milled Ti-Cu alloy is also shown in Figure 1c. This pattern displays a broadened peak corresponding to the (111) planes of the TiCu phase, confirming the synthesis of the TiCu phase powder during 30 hours of milling, as noted in a previous study (Moniri Javadhesari et al., 2019).

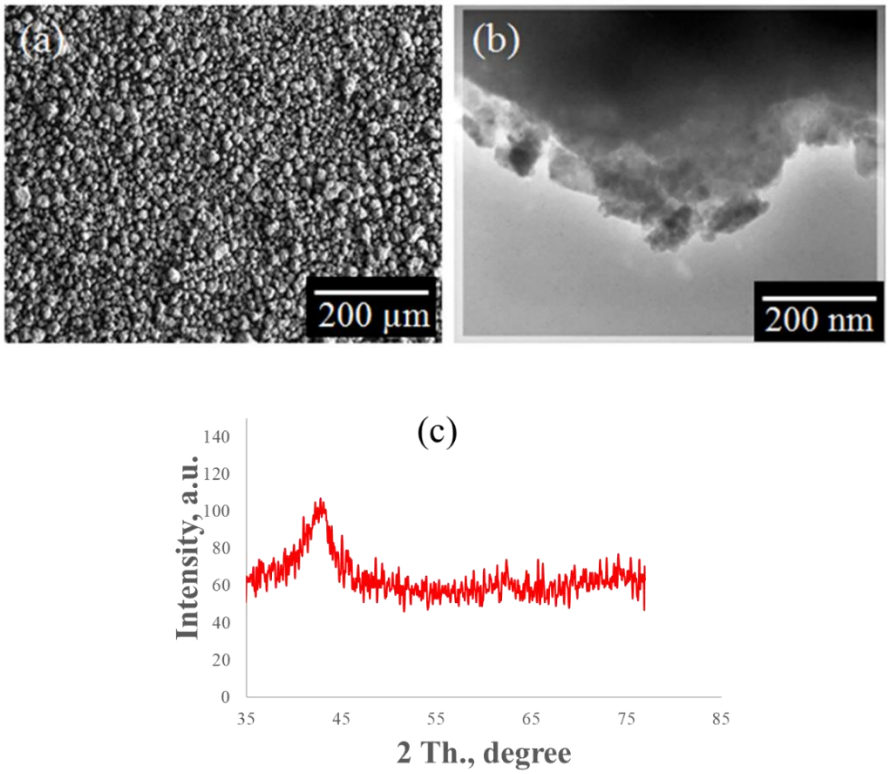

Figure 1. (a) SEM micrograph, (b) TEM micrograph, and (c) XRD pattern of 30h- mechanically alloyed Ti-Cu alloy.

3.2. Microstructure of bulk Ti-50 at.%Cu alloy

The TiCu powder was cold compacted and effectively sintered using a microwave-assisted heating method at processing temperatures ranging from 700 to 900 °C. Figure 2 shows SE and BSE SEM images of the samples sintered at different temperatures. As depicted in the figure, the porosity of the sintered sample decreases as the sintering temperature increases. At 900 °C, a nearly fully dense alloy was obtained. The BSE images also reveal microstructures consisting of two distinct phases and their distribution. Figure 3 displays a high-magnification BSE micrograph and chemical analysis of the alloy, showing the different phases of the sintered sample microstructure at 900 °C. This indicates the dual-phase structure developed during microwave-assisted sintering. XRD analysis supports the coexistence of the Ti3Cu4 and TiCu phases.

Figure 4 presents the XRD pattern of the sintered sample at various temperatures. The sample comprises the dominant phases of Ti_3Cu_4 and TiCu, which formed at high temperatures during sintering. The complex phase structure developed during microwave sintering of this alloy differs from the phases formed during vacuum sintering, as reported in previous studies (Akbarpour et al., 2016; Moniri Javadhesari et al., 2020a). In sintered TiCu powder processed by high-frequency induction heating, as conducted by In-Jin Shon et al. (Shon et al., 2010), the major phase of TiCu and various minor phases such as Cu2Ti, Cu_4Ti_3, and Cu_3Ti were reported. This difference in phase formation can be attributed to the

different heating methods, which influence atomic diffusion behavior and the thermodynamics of phase formation. Table 1 summarizes the microstructural features of the microwave-sintered Ti-Cu alloy. The sample grain size remained within the nanoscale region, increasing from 23 nm to 28 nm with rising sintering temperatures. Microstrain also decreased during the sintering process, although a significant amount of strain remained in the sintered sample. This may be due to the complex phase structure and the varying thermal behaviors of the phases (Akbarpour et al., 2022).

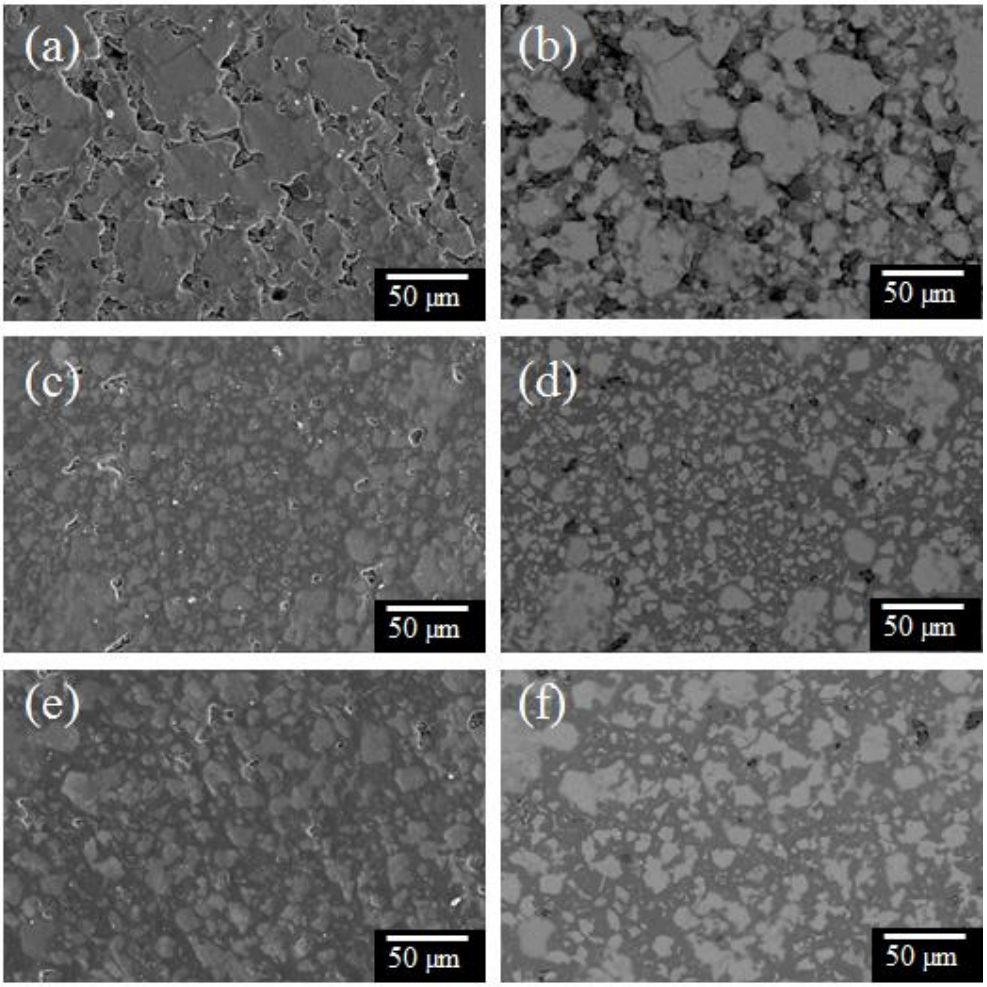

Figure 2. BSE and SE SEM micrographs of the Ti-Cu alloy sintered at different temperatures of (a, b) 700 °C, (c, d) 800 °C, and (e, f) 900 °C.

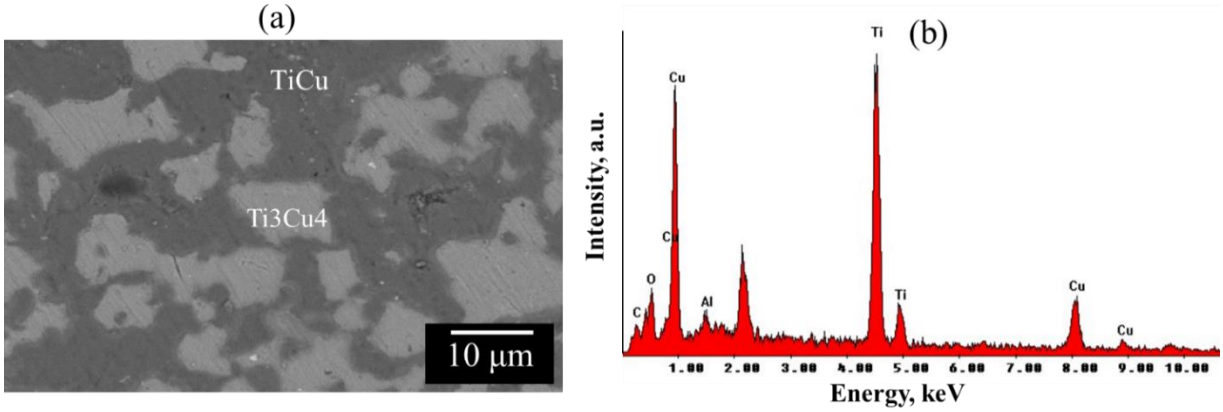

Figure 3. (a) High-magnification BSE micrograph and (b)EDS of the Ti-Cu alloy sintered at 900 °C.

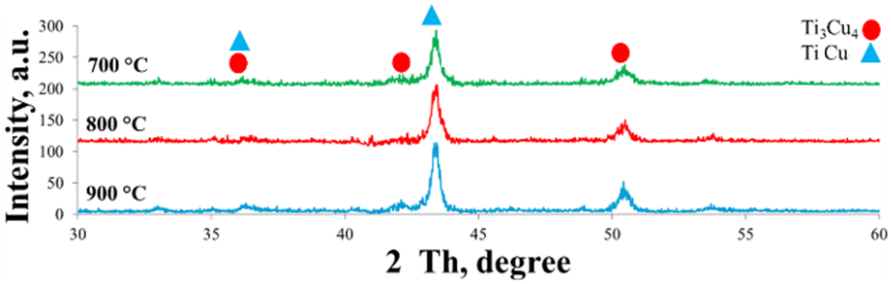

Figure 4. XRD patterns of the Ti-Cu alloy sintered at different temperatures.

Table 1. Density, grain size and microstrain of the Ti-Cu alloy sintered at different temperatures.

Temperature, °C	700	800	900
Density, g/cm^3	5.70	6.30	6.54
Grain size, nm	23	25	28
Microstrain, %	0.43	0.39	0.35

The transmission electron microscopy (TEM) image and selected area electron diffraction (SAED) pattern of the Ti-Cu alloy sintered at 900 °C are presented in Figure 5. The image confirms the nanocrystalline structure of the sintered TiCu alloy, with a grain size of 30 nm. The average grain size was obtained, which is slightly larger than the value obtained from X-ray diffraction (XRD). Additionally, the SAED pattern confirms the formation of the Ti_3Cu_4, TiCu, and Ti_2Cu phases.

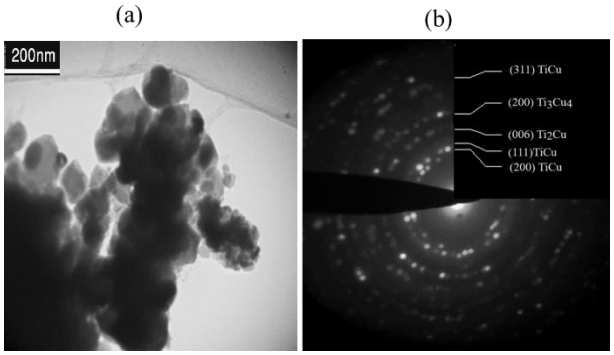

Figure 5. (a) TEM micrograph and (b) SAED pattern of the synthesized alloy.

3.3. Micro-hardness

Vickers micro-hardness measurements were performed on the polished surface of the TiCu. Figure 6 shows the microhardness as a function of sintering temperature. As shown, the microhardness increases with increasing temperature, which is related to the decreasing porosity with temperature, as shown in Table 1. The measured microhardness value of the sintered TiCu powder at 900 °C was approximately 880 HV, which is a very high value for a Ti-Cu alloy. The hardness value obtained for the TiCu vacuum-sintered alloy in this research is approximately 26 percent higher than the value reported by Shon et al. for TiCu produced by high-energy milling and high-frequency induction heating (Shon et al., 2010). The hardness achieved through microwave-assisted sintering in this study was lower than that of the conventionally sintered alloy (10 GPa) (Moniri Javadhesari et al., 2020a). The variation in the hardness of the Ti-Cu alloy prepared by different methods is attributed to the phases formed, their inherent hardness values, and the volume fraction of these phases in the microstructure of the sample. The hardness of the various phases in this system has been reported in the literature (Akbarpour et al., 2022; Moniri Javadhesari et al., 2020a).

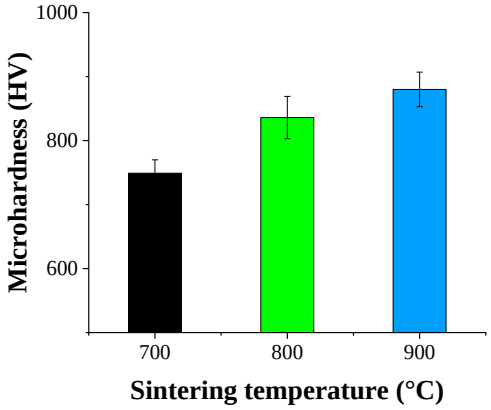

Figure 6. Microhardness as a function of sintering temperature.

4. CONCLUSION(S)

In this research, a Ti-50 at% Cu alloy was produced by high-energy mechanical alloying of elemental micron-sized Ti and Cu powders, followed by a microwave-assisted sintering process at different temperatures. The densification, microstructure, and mechanical properties of the synthesized alloy were characterized. In this method, rapid consolidation of the Ti-Cu alloy was achieved without significant grain growth, and it occurred in a short sintering time. The effects of the sintering method and temperature on the microstructure and mechanical properties were studied. The sintering density increased with temperature, and the highest

density of 6.54 g/cm³ was obtained at 900°C. Microstructural studies showed a nanocrystalline structure for the alloy, consisting mainly of Ti_3Cu_4 and TiCu phases as the major phases, with Ti_2Cu as a minor phase and a grain size of approximately 28 nm. Mechanical tests revealed a high microhardness of 880 HV for the dense Ti-Cu alloy.

ACKNOWLEDGEMENTS

The author wishes to acknowledge University of Maragheh for the all support throughout this research work.

REFERENCES

1. Akbarpour, M. R., & Hesari, F. A. (2016). Characterization and hardness of TiCu-Ti2Cu3 intermetallic material fabricated by mechanical alloying and subsequent annealing. *Materials Research Express*, *3*(4). https://iopscience.iop.org/article/10.1088/2053-1591/3/4/045004

2. Akbarpour, M. R., Mirabad, H. M., Hemmati, A., & Kim, H. S. (2022). Processing and microstructure of Ti-Cu binary alloys: A comprehensive review. *Progress in Materials Science*, *127*(January), 100933. https://doi.org/10.1016/j.pmatsci.2022.100933

3. Akbarpour, M. R., & Moniri Javadhesari, S. (2020). Densification and Mechanical and Antibacterial Properties of Low-Cost Powder Metallurgy TiCu Intermetallic Alloy as a Potential Biomedical Material. *JOM*, *72*(9), 3262–3268. https://doi.org/10.1007/s11837-020-04234-0

4. Akbarpour, M. R., & Moniri Javadhesari, S. (2023). Characterization of Flowability and Compaction Behavior of Biomedical Ti-Cu Intermetallic Alloy Synthesized by Mechanical Alloying Method. *Advanced Ceramics Progress*, *9*(2), 8–15. https://doi.org/10.30501/acp.2023.387236.1118

5. Alqattan, M., Alshammari, Y., Yang, F., Peters, L., & Bolzoni, L. (2021). Biomedical Ti–Cu–Mn alloys with antibacterial capability. *Journal of Materials Research and Technology*, *10*, 1020–1028. https://doi.org/10.1016/j.jmrt.2020.12.044

6. Fernández, H., Ordoñez, S., Pesenti, H., González, R. E., & Leoni, M. (2019). Microstructure homogeneity of milled aluminum A356–Si3N4 metal matrix composite powders. *Journal of Materials Research and Technology*, *8*(3), 2969–2977. https://doi.org/10.1016/j.jmrt.2019.05.004

7. Kikuchi, M., Takada, Y., Kiyosue, S., Yoda, M., Woldu, M., Cai, Z., Okuno, O., & Okabe, T. (2003). Mechanical properties and microstructures of cast Ti–Cu alloys. *Dental Materials*, *19*(3), 174–181. https://doi.org/10.1016/S0109-5641(02)00027-1

8. Liu, J., Li, F., Liu, C., Wang, H., Ren, B., Yang, K., & Zhang, E. (2014). Effect of Cu content on the antibacterial activity of titanium-copper sintered alloys. *Materials Science & Engineering. C, Materials for Biological Applications*, *35*, 392–400. https://doi.org/10.1016/j.msec.2013.11.028

9. Liu, W., Chen, X., Ahmad, T., Zhou, C., Xiao, X., Wang, H., & Yang, B. (2022). Microstructures and mechanical properties of Cu–Ti alloys with ultrahigh strength and high ductility by thermo-mechanical treatment. *Materials Science and Engineering: A*, *835*, 142672. https://doi.org/10.1016/j.msea.2022.142672

10. Mahmoudi, P., Akbarpour, M. R., Lakeh, H. B., Jing, F., Hadidi, M. R., & Akhavan, B. (2022). Antibacterial Ti–Cu implants: A critical review on mechanisms of action. *Materials Today Bio*, *17*(September), 100447. https://doi.org/10.1016/j.mtbio.2022.100447

11. Moniri Javadhesari, S., Alipour, S., & Akbarpour, M. R. (2019). Microstructural characterization and enhanced hardness, wear and antibacterial properties of a powder metallurgy SiC/Ti-Cu nanocomposite as a potential material for biomedical applications. *Ceramics International*, *45*(8), 10603–10611. https://doi.org/10.1016/j.ceramint.2019.02.127

12. Moniri Javadhesari, S., Alipour, S., & Akbarpour, M. R. (2020a). Biocompatibility, osseointegration, antibacterial and mechanical properties of nanocrystalline Ti-Cu alloy as a new orthopedic material. *Colloids and Surfaces B: Biointerfaces*, *189*(August 2019), 110889. https://doi.org/10.1016/j.colsurfb.2020.110889

13. Moniri Javadhesari, S., Alipour, S., & Akbarpour, M. R. (2020b). Effects of SiC nanoparticles on synthesis and antimicrobial activity of TiCu nanocrystalline powder. *Ceramics International*, *46*(1), 114–120. https://doi.org/10.1016/j.ceramint.2019.08.240

14. Shon, I. J., Kim, N. R., Du, S. L., Ko, I. Y., Cho, S. W., & Kim, W. (2010). Rapid consolidation of nanostructured TiCu compound by high frequency induction heating and its mechanical properties. *Materials Transactions*, *51*(11), 2129–2131. https://doi.org/10.2320/matertrans.M2010251

15. Yuan, Y., Luo, R., Ren, J., Zhang, L., Jiang, Y., & He, Z. (2022). Design of a new Ti-Mo-Cu alloy with excellent mechanical and antibacterial properties as implant materials. *Materials Letters*, *306*, 130875. https://doi.org/10.1016/J.MATLET.2021.130875

16. Zhang, D., Qiu, D., Gibson, M. A., Zheng, Y., Fraser, H. L., StJohn, D. H., & Easton, M. A. (2019). Additive manufacturing of ultrafine-grained high-strength titanium alloys. *Nature*, *576*(7785), 91–95. https://doi.org/10.1016/j.matlet.2021.130875

17. Zhang, Z., Zheng, G., Li, H., Yang, L., Wang, X., Qin, G., & Zhang, E. (2019). Anti-bacterium influenced corrosion effect of antibacterial Ti-3Cu alloy in Staphylococcus aureus suspension for biomedical application. *Materials Science & Engineering. C, Materials for Biological Applications*, *94*, 376–384. https://doi.org/10.1016/j.msec.2018.09.057

Advanced Ceramics Progress: Vol. 10, No. 2, (Spring 2024) 23-31

Materials and Energy Research Center
MERC

Contents lists available at ACERP

Advanced Ceramics Progress

Journal Homepage: www.acerp.ir

Original Research Article

Corrosion Studies on the Hydroxyapatite-Gelatin-Mono Layered Graphene Oxide Nanocomposite Coating on SS316L

Hurieh Mohammadzadeh *, Robabeh Jafari

Assistant professor, Department of Materials Science and Engineering, Faculty of Engineering, Urmia University, Urmia, Iran.

* Corresponding Author Email: h.mohamadzadeh@urmia.ac.ir (Hurieh Mohammadzadeh) URL: https://www.acerp.ir/article_209820.html

ARTICLE INFO

Article History:
Received: 02 August 2024
Revised: 16 November 2024
Accepted: 02 December 2024

Keywords:
Nanocomposite,
Coating,
Single-layer Graphene Oxide/ Hydroxyapatite/ Chitosan,
Corrosion

ABSTRACT

Stainless steel 316L (SS316L) is a good candidate for metal implants due to its excellent tensile strength and high corrosion resistance. However, its surface needs to be improved to enhance biocompatibility, bioactivity, and antimicrobial functions. Among bioceramics, hydroxyapatite ($Ca_{10}(PO_4)_6(OH)_2$) is widely used in medical applications due to its mineral composition, which is similar to the natural hard tissues of the body, and its biomimetic morphology. Chitosan possesses attractive biological properties such as good biodegradability, non-toxicity, biocompatibility, and cellular bioavailability. Graphene oxide demonstrates antibacterial activity against bacteria, fungi, and viruses, which can help limit cancer-causing infections in surgeries. Accordingly, an HA-based nanocomposite (HA-CS-GO) was deposited on SS316L sheets by electrophoretic deposition. Nanoparticle HA was synthesized via the sol-gel method. The coating was applied at 80V for 1 minute. To study the products and coating, various analyses were employed, including XRD, SEM, FTIR, electrochemical impedance spectroscopy (EIS), and polarization analysis. The results confirmed the successful synthesis of HA. The nanocomposite coating (thickness ~12.7 µm) was properly deposited on SS316L. The corrosion resistance improved with the coating; the current density decreased from 7.6 to 1.4 $\mu A \cdot cm^{-2}$. The mechanism of corrosion was evaluated by EIS data. The corresponding equivalent circuit was proposed, and the dielectric capacitor and resistance values were estimated.

https://doi.org/10.30501/acp.2024.466016.1154

1. INTRODUCTION

Biomaterials, as substances engineered to interact with biological systems for medical purposes, are produced in various forms such as soft and hard tissues, scaffolds, implants, etc., and can be absorbable or non-absorbable in the body. Additionally, they may have neutral, bioactive, biostable, or biodegradable properties (Dvorsky et al., 2020; Hudecki et al., 2018). The properties that a biomaterial must possess to be used as an implant include biocompatibility, corrosion resistance, non-toxicity, excellent mechanical properties, and the absence of foreign body reactions (Eliaz, 2019). Different materials, including metallic components, polymers, ceramics, or composite materials, can be used as biomaterials. Metallic components include Ti and its alloys (Liao et al., 2022), stainless steels (Verma et al., 2023), and Mg and its alloys (Saadati et al., 2021b), which are chosen for their high mechanical properties, good corrosion resistance, and biocompatibility in physiological environments (Harun et al., 2018). Among these alloys, stainless steel is particularly effective in bone stabilization and other orthopedic, medical, and dental applications due to its excellent mechanical properties, high corrosion resistance, and affordability (Logesh et al., 2022; Wadood, 2021). Therefore, to enhance biocompatibility by increasing corrosion

Please cite this article as: Mohammadzadeh, H. & Jafari, R. (2024). Corrosion Studies on the Hydroxyapatite-Gelatin-Mono Layered Graphene Oxide Nanocomposite Coating on SS316L, *Advanced Ceramics Progress*, 10(2), 23-31. https://doi.org/10.30501/acp.2024.466016.1154

resistance, bioactive and biocompatible ceramic coatings are developed. Hydroxyapatite (HA), a synthetic bioceramic, with the chemical formula $Ca_{10}(PO_4)_6(OH)_2$ is a ceramic biomaterial (Kuo & Du, 2022) with outstanding bio-features such as biocompatiblity (Modolon et al., 2021a) and similarity to the hard tissues in the body of mammals. Due to its strong bonding with bone tissue (Baslayici et al., 2022), HA and its composites are widely used in medical applications like implants (Choi et al., 2020) because of their high surface-to-volume ratio, reactivity (Modolon et al., 2021), biomimetic morphology, and osteogenesis induction, to name a few (Asadipour et al., 2019; Das & Chakraborti, 2021). One of the common methods for HA synthesis is sol-gel (Chen et al., 2011).

Ceramics are often used in combination with natural polymers, such as chitosan, to form a uniform and non-porous structure. Among natural polymers, there is a growing interest from researchers worldwide in chitosan (CS), which is a linear and cationic polysaccharide (Zhang et al., 2022). Due to the presence of amino groups in its structure, CS possesses attractive physicochemical and biological properties such as biocompatibility, biodegradability, hydrophilicity, non-toxicity, and high cellular bioavailability. Moreover, CS has acceptable mechanical strength, good thermal stability, and can combine with metals and proteins due to its specific chemical structure (Saadati et al., 2021a).

Graphene and its derivatives have exhibited antibacterial activities against bacteria, fungi, and viruses (Zahra et al., 2023). Graphene oxide (GO) can be synthesized by chemically oxidizing graphite. GO, a unique material, is composed of a single monomolecular layer of graphite with various oxygen-containing functionalities (e.g., carbonyl, carboxyl, and hydroxyl groups) that help disperse GO in polymeric solutions and enhance its hydrophilicity (Guo et al., 2023; Nair et al., 2022). GO is a biocompatible, carbon-based material, which is efficiently used in nanocomposite materials, polymer composite materials, biomedical applications, and catalysis (Naderi & Nadri, 2022; Sahoo et al., 2023). Additionally, GO exhibits a hydrophilic nature, which is vital for biological functionality by improving cell adhesion, cell viability, and boosting cell proliferation (Staneva et al., 2021).

Several methods have been employed to deposit and form ceramic/polymeric base coatings over metal substrates, including electrochemical deposition (Perju et al., 2022), electrophoretic (EPD) (Akram et al., 2023), sputtering (Monai et al., 2023), sol-gel (Shanmugapriya et al., 2022), immersion (Khalid et al., 2013), plasma spray (Vahabzadeh et al., 2015), hot isostatic press (Onoki & Hashida, 2006), deposition pulsed laser (Dhinasekaran et al., 2021). Among these approaches, EPD has become popular for a variety of emerging applications in both academic and industrial sectors due to its simplicity, short processing time, cost-effectiveness, and ability to deposit a wide variety of materials and combinations (Sorkhi et al., 2019). Asgar et al. coated GO on titanium alloy (Ti6Al4V) by EPD and reported an improvement in corrosion resistance due to the GO coating (Asgar et al., 2019). It has been reported that GO in HA/CC/GO coatings (deposited by EPD) on AZ91D increased corrosion resistance by removing surface cracks (Askarnia et al., 2021). Shi et al. deposited GO–CS–HA nanocomposites on a Ti substrate as orthopedic-related implants via electrophoretic deposition and studied the microstructure and corrosion behavior of the coating (Shi et al., 2016). In another study, the HA-GO nanocomposite coating was applied to a Ti substrate through EPD to improve biomedical functionality (Fardi et al., 2020). It has been reported that the mechanical properties and corrosion resistance of the coating can be improved with GO (Pan et al., 2023).

Due to the importance and attractiveness of HA and GO for biological applications, numerous studies have been conducted on their composites as coatings over implant metals. However, the coating of GO in combination with HA and CS needs further study to examine the morphology, microstructure, and corrosion behavior of the coating in the body environment. Given the lack of systematic research into HA-CS-GO coatings on SS316L sheets, the current research aims to study the features of the HA-CS-GO coating in detail.

2. MATERIALS AND METHODS

2.1. MATERIALS

For the coating material, npHA was synthesized. Moreover, some chemicals were used for coating setup including the electrolyte. For this purpose, ethanol 99.9%, di-phosphorus pentoxide (P_2O_5, Ghatran-Shimi, Iran), calcium nitrate ($Ca(NO_3)_2.4H_2O$, Sigma-Aldrich), deionized water, acetic acid (CH_3COOH), chitosan, gelatin and ascorbic acid (Sigma-Aldrich), single-layer graphene oxide (GO), magnesium nitrate ($Mg(NO_3)_2.6H_2O$, Merck), and isopropyl alcohol (C_3H_8O, Sigma-Aldrich) were purchased. The SS316L sheets (Table 1) were substrates, which were sandblasted and cut into the dimensions of 20×10 mm^2.

TABLE 1. The chemical composition of SS316L sheets.

Fe	Cr	Ni	C	Mn	P	S	Si	Mo	N
Balance	17.1	12.2	0.03	2.02	0.045	0.03	0.75	2.2	0.1

2.2. SYNTHESIS OF nHA

To synthesize npHA by the sol-gel approach, the Ca/P molar ratio was set to 10:3. Then, 1.67 M of $Ca(NO_3)_2{\cdot}4H_2O$ and 0.5 M of P_2O_5 were prepared in separate beakers by dissolving them in pure ethanol for 0.5 h. The P_2O_5 solution was gradually added to the $Ca(NO_3)_2{\cdot}4H_2O$ solution and mixed for 3 h to form a gel. The gel product was heated at 60 °C for 24 h to dehumidify. The resulting powder was calcined at 650 °C for 3 h to produce the white-colored HA nanopowder.

2.3. COATING

Coating of HA-CS-GO was performed on SS316L sheets using the EPD approach. For EPD, CS (0.5 g/L), GO (0.015 g/L), Gel (5 g/L), and HA (0.5 g/L) were dispersed in the electrolyte suspension. CS and Gel were dissolved in a mixture of ethanol and deionized water (80/20 volume ratio) with 0.25 cc acetic acid and ethanol. HA nanopowder was added to this suspension. After 5 h of stirring, GO was added to the solution and mixed for an additional 1 h. An ultrasonic probe was employed to disperse the suspension for 5 min. Finally, the electrolyte was stirred for another 5 h using a magnetic stirrer. The SS316L sheets were degreased in a 10 wt.% NaOH solution at 60 °C for 0.5 h, followed by immersion in an acetone solution in an ultrasonic bath for 1 h. They were then placed in hydrochloric acid for 1 min, washed with distilled water, and dried.

For coating by EPD, a two-electrode (SS316L, 20×10 mm^2) cell was used for the substrate and anode. The distance between the electrodes was set to 1 cm. To stabilize the electrolyte, it was kept at room temperature for 3 days. Before coating, it was dispersed for 2 h. The coating process was performed at 80 V for 1 min.

2.4. ANALYSIS

The chemical analysis was performed using X-ray diffraction (XRD) with a PHILIPS XRD apparatus (PW1730, Netherlands, Cu Kα, λ=1.5418 Å, step size=0.05°, time per step=1 s). The crystallite size was determined from the XRD pattern using X'Pert-Pro software.

A scanning electron microscope (SEM, Zeiss Sigma 300 - Germany) equipped with EDS was used for the microstructural study of the synthesized powders and coating. The Fourier transform infrared (FTIR) spectra of npHA and GO were collected with an FTIR spectrophotometer (Thermo Nicolet NEXUS 670 FTIR, Thermo Scientific, USA) in absorption mode over the wavelength range of 400-4000 cm^{-1}.

Potentiodynamic polarization tests (scanning speed of 1 mV/s and voltage from -1 to 0.9 mV) and electrochemical impedance spectroscopy (EIS, frequency range from 100 kHz to 10 mHz) were employed at room temperature to study the corrosion response of the samples in simulated body fluid (SBF) using a Potentiostat/Galvanostat/Impedance Analyzer (Metrohm DropSens, μStat-I 400s). For this purpose, G3-89 1999 ASTM standards were followed, where the counter, reference, and working electrodes were a platinum (Pt) plate, a KCl-saturated calomel (Ag/AgCl) electrode, and the coated samples, respectively. The EIS data were analyzed using the equivalent circuit simulated by ZView software.

3. RESULTS AND DISCUSSION

3.2. SYNTHESIZED NANOMATERIALS

Figure 1(a) illustrates the X-Ray Diffraction (XRD) pattern of the synthesized npHA, which was in accordance with the reference code JCPDS no. 09-0432. The average crystallite size of the synthesized npHA was calculated through the Debye-Scherrer equation (Eq. 1) from five major peaks to be 24.4 nm. The parameters of this equation are D, κ, λ, β, and θ, which are representatives of the crystallite size, constant coefficient (0.94), wavelength (1.54 Å), Bragg angle width, and Bragg angle, respectively(Modolon et al., 2021b).

$$D = \frac{\kappa\lambda}{\beta\cos\theta} \quad (1)$$

Figure 1(b) shows the FTIR spectrum of the npHA product. The chemical groups OH^- and CO_3^{2-}, characteristic of nonstoichiometric HA, were found in the FTIR spectrum due to the synthesis route (Gheisari et al., 2015). There is a relatively wide absorption band at 3560 cm^{-1} showing the stretching vibration of the hydroxyl functional group (OH^-). The absorption peaks at 3440 and 2921 cm^{-1} correspond to the stretching and bending vibrations of water absorption bonds (Kesmez, 2020; Priyam et al., 2019). Two peaks at 4515 and 1460 cm^{-1} are associated with the asymmetric stretching of the CO_3^{2-} group. Accordingly, the C from organic materials is not completely decomposed and may instead dissolve in the crystal (Mujahid et al., 2015). he peaks that occurred at 1039, 972, 729, 571 cm^{-1}, and 449 cm^{-1} correspond to the asymmetric bending and stretching vibrations of the phosphate group PO_4^{3-} (Prasanna & Venkatasubbu, 2018).

Figure 1(c) illustrates the microstructure of the produced nP-HA powder. According to the SEM images and measurements by ImageJ software, HA particles were spherical with an average size of ~31.7 nm, which agglomerated to form clusters with an average diameter ranging from 210 nm to 4.1 μm.

Figure 2(a) shows the FTIR spectra of GO to study the compositions and bonding. There is a broad peak at 3439 cm^{-1}, which corresponds to the stretching vibrations of the hydroxyl (-OH) and water bonds. The absorption at 1718 cm^{-1} shows the stretching vibrations of the carbonyl group (C=O). The peak at 1620 cm^{-1} relates to C=C stretching vibrations. The peaks at 1213 and 1049 cm^{-1} correspond to C-O stretching vibrations (Jeyaseelan et al., 2021; Kusrini et al., 2020).

Figure 2(b) shows the SEM images of GO, while the corresponding molecular structure is illustrated in Figure

2(c). The SEM image in Figure 2(b) reveals that the nano-sheets of GO are very smooth. GO has a metastable nature, causing the sheets to fold at the edges. This deviation from thermodynamic stability arises from the oxygen-containing functional groups in the basal planes and sp^3 carbons, as shown in Figure 2(e) (Al-Gaashani et al., 2019). The covalence bonding between C atoms and the functional chemical groups of -OH, -O and =O is shown in Figure 2(c).

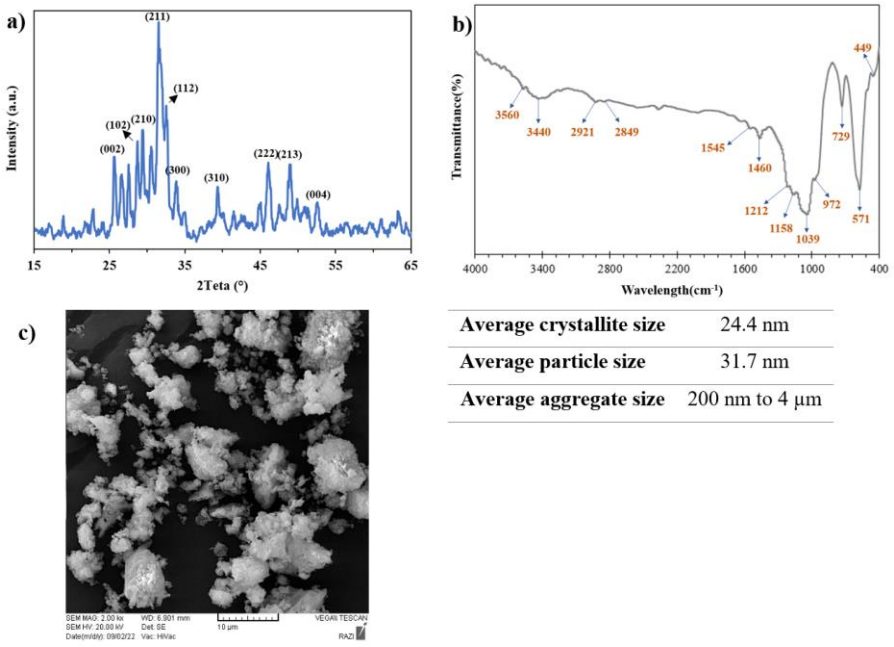

Average crystallite size	24.4 nm
Average particle size	31.7 nm
Average aggregate size	200 nm to 4 μm

Figure 1. XRD pattern, b) FTIR spectrum, and c) the microstructure of npHA synthesized by sol-gel method.

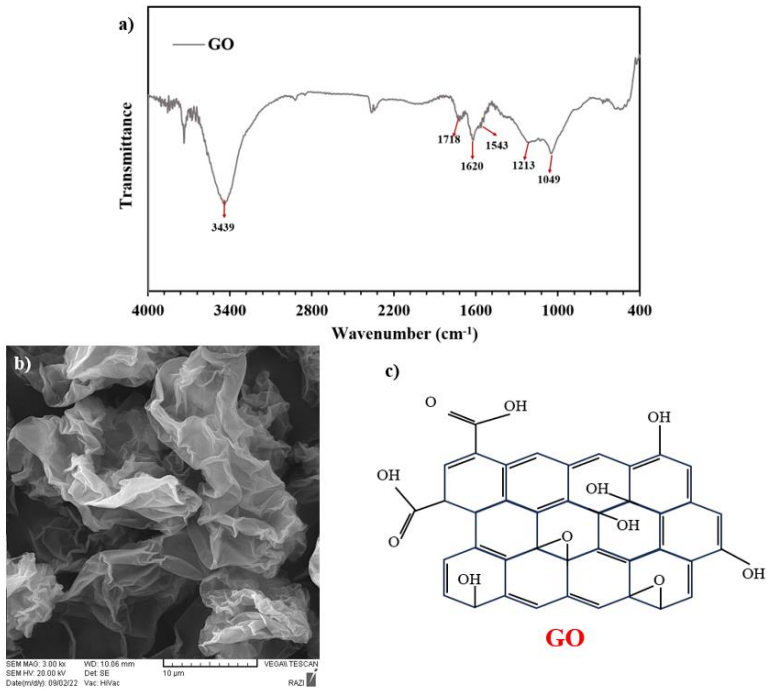

Figure 2. a) FTIR spectrum, b) the SEM images of GO and c) the atomic structures of GO molecules.

3-2- Coating Morphology

Figure 3(a)-(d) shows the microstructure and morphology of the outer surface of the HA-CS-GO coating on the SS316L substrate. A uniform coat is formed over the substrate, as shown in the OM image of the coating surface in Figure 3(a), although some microcracks are observed (pointed to by the red hollow arrow). The SEM images of the coating surface in

Figures 3(b) and (c) show the morphology of the coating microstructure and its constituents. In Figure 3(b), the coating appears relatively uniform; however, at higher magnification (Figure 3(c)), detailed components are discernible. Additionally, the agglomerations of npHA are shown by the blue patterned arrow, which are formed due to the function of CS as a binder phase. The GO sheets are visible in the coating, as indicated by the green patterned arrow in Figure 3(c). According to Figure 3(d), which shows the cross-section of the coated sample, the average coating thickness was measured from at least 10 different positions to be 12.7 ± 2.1 µm.

The GO sheets can be readily covered by hydrogen bonding (Figure 4) to stabilize HA molecules electrostatically (Saadati et al., 2021b). As Figure 4 shows, the CS and HA molecules can bond together by forming connections between Ca^{2+} on HA and the primary and secondary –OH and NH_2 groups of CS (Dantas et al., 2019; Venkatesan & Kim, 2010). Moreover, the electrically charged GO can absorb Ca^{2+} from the molecules of HA and react with CS molecules to form inter- and intra-molecular hydrogen bonding. Accordingly, electrostatic attractions and hydrogen bonding form between GO and HA/CS structures.

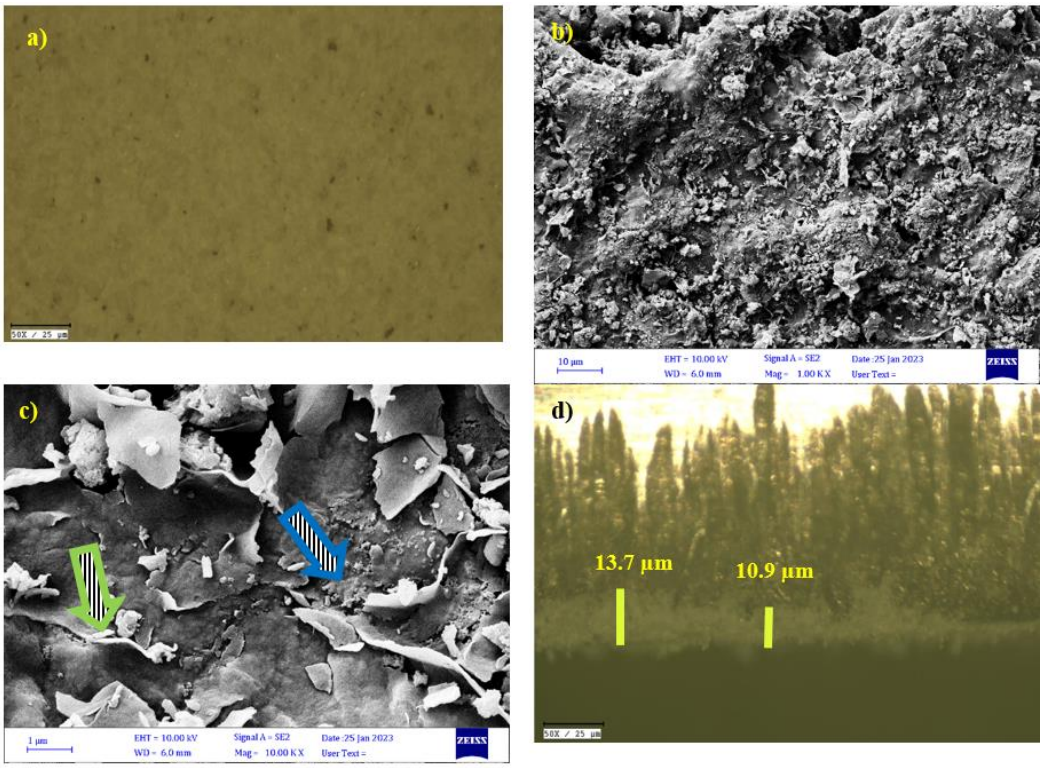

Figure 3. OM images of a) coating surface, and b) coating cross section, and c, and d) SEM images of coting surface. (Yellow and red solid arrows show the sub-micro pores, and GO sheet, respectively. The red hollow, and blue patterned arrows point to the micro crack, and npHA agglomerations, respectively.

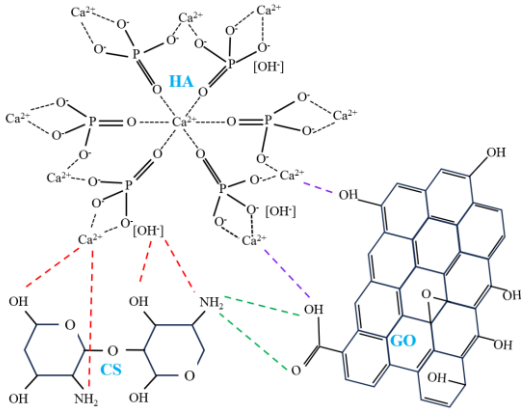

Figure 4. The structure of the GO, HA and CS molecules and their iner-molecular bonds and connections.

3-3-CORROSION BEHAVIOR

In order to evaluate the corrosion behavior of the coating on the corrosion performance, the corrosion properties of the coated SS316L sheet were assessed through potentiodynamic polarization and electrochemical impedance spectroscopy (EIS) analyses in the SBF solution. Figure 5 shows the polarization curves of the substrate and the coated sample, and the electrochemical data for corrosion rate (current density) and corrosion potential, derived from the Tafel extrapolation lines, are presented for comparison. According to the results, the coated sample exhibited lower i_{corr} and higher E_{corr} than the uncoated SS316L sheet. This can be attributed to the very restricted access of the corrosive agents from the electrolyte to the substrate due to the coating. The coating has improved the corrosion resistance. The connection of GO with HA molecules creates a more compact and adhesive structure in the coating microtexture, which enhances corrosion resistance (Arul Xavier Stango & Vijayalakshmi, 2021).

To evaluate the corrosion mechanism and electrochemical features of the coating in the SBF, electrochemical impedance spectroscopy (EIS) analysis was employed. The results of the EIS test, including Nyquist, phase, and Bode plots, are presented for the coated sample in SBF in Figures 6(a) to (c). The Nyquist plot in Figure 6(a) shows a small semicircle at high frequency and a broader semicircle at low frequency, respectively. These semicircles in the Nyquist plot can be related to the reactions at the coating-SBF and the SBF-metal interfaces (Hafedh et al., 2017). Moreover, there are two peaks in the frequency ranges of 10,000 to 100,000 Hz and 0.1 to 10 Hz in the phase plot (Figure 6(b)), which correspond to the two semicircles of the Nyquist plot. The Bode plot in Figure 6(c) confirms the Nyquist and phase results and shows the total resistance value to be 53083 $\Omega.cm^2$. The capacitance of the coating was proposed by estimating the dielectric properties of the material through the equivalent electric circuit (EEC) that was fitted to the experimental EIS data. Accordingly, the experimental data from the EIS analysis were simulated by Zview software modeling, and the obtained EEC is shown in Figure 6(d). The acquired fitting shows excellent correspondence to the EIS data; in Figures 6(a) to (c), the lines and points represent the estimated model and experimental data, respectively. This model includes various elements in the electric circuit, such as the resistances and capacitances of R1, R2, R3, CPE1, and CPE2. The CPE (constant phase element) does not represent an ideal capacitor. This occurs due to the non-parallel double layer and the roughness of the interfaces. R1 represents the electrolyte resistance. R2 and R3 are the resistances of the nanocomposite coating and the charge transfer (double-layer) resistance at the metal/electrolyte interface, respectively. CPE1 and CPE2 correspond to the capacitances of the double layer at the substrate/electrolyte interface and the coating/electrolyte interface, respectively. Figure 6(e) presents the electrochemical parameters obtained from modeling the EIS results and shows the estimated charge transfer resistance at the interface to be 104,607 $\Omega \cdot cm^2$, indicating considerable resistance against progressing corrosion.

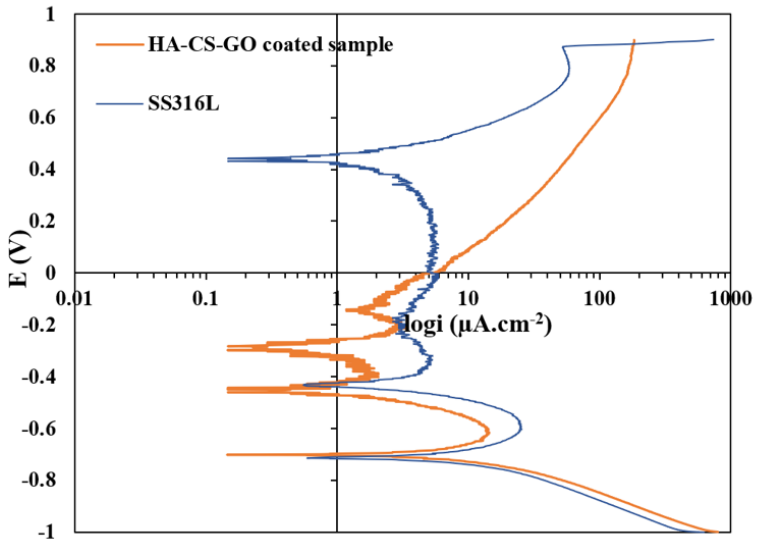

Samples	E_{corr} (V)	I_{corr} (µ.cm^{-2})
SS316LC	-0.714	706
Coated sample (HA-CS-GO)	-0.461	1.4

Figure 5. The polarization curves of E vs logi for the bare substrate and HA-CS -GO coated sample, and the resulted data from the Tafel extrapolation.

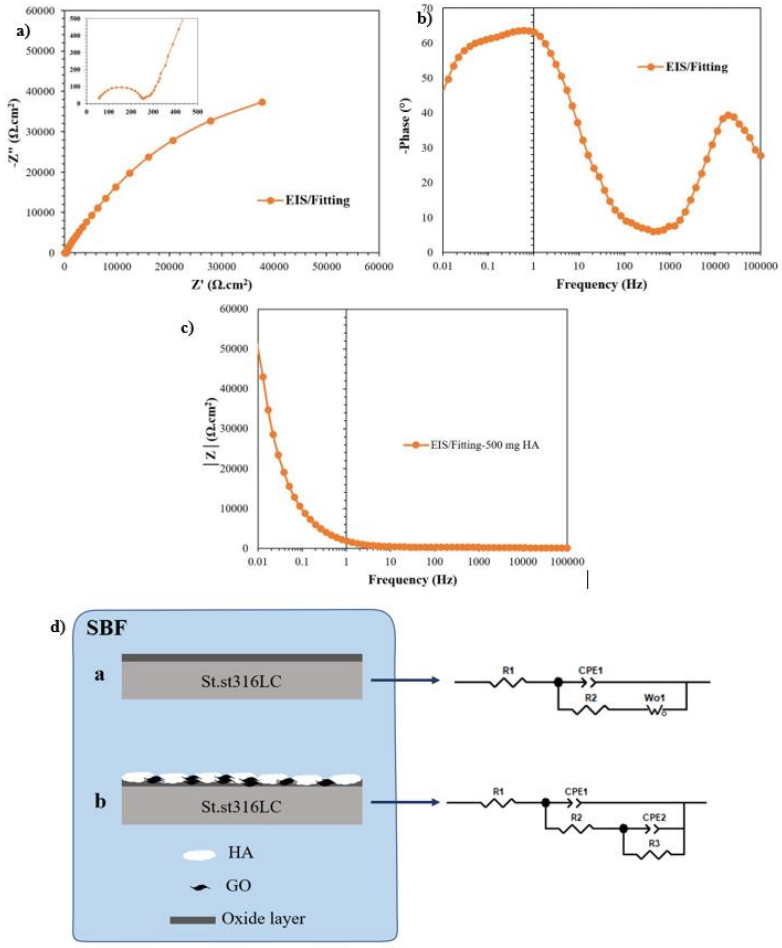

Samples	R1(Ω.cm²)	CPE1 (µF)	R2(Ω.cm²)	CPE2(µF)	R3(Ω.cm²)
Coated sample (HA-CS-GO)	43.82	2.3E-7	226.4	1.6E-4	104607

Figure 6. a) Nyquist, b) phase, and c) Bode plots with the fitted lines of the EEC mathematical model for the coated sample, and d) a schematic simulation of the electrochemical events and its representative EEC model, e) the electrochemical parameters obtained from modeling of the EIS results.

4. CONCLUSION(S)

The nano-composite coating, consisting of npHA, CS, and reduced and functionalized graphene oxide (GO), was applied to an SS316L sheet using the electrophoretic deposition (EPD) method to evaluate the morphology and corrosion performance of the coating in biological environments. The following results were obtained. Additionally, npHA was synthesized by the sol-gel method, and the features of the product were evaluated.

- The particle size and crystallite size of the synthesized HA nanoparticles with spherical morphology were 31.7 nm and 24.4 nm, respectively.
- The properties of GO were examined and confirmed by FTIR spectroscopy and SEM images.
- The microstructure and thickness of the HA-CS-GO nano-composite coating were evaluated by SEM and Optical Microscopy (OM) imaging.
- A uniform HA-CS-GO coating with an average thickness of 12.7 µm was properly deposited onto the SS316L substrate by the EPD method.
- The corrosion behavior of the material before and after deposition was studied by polarization analysis, which confirmed the improved resistance to corrosion due to the coating. The current density for SS316L decreased from 7.6 to 1.4 $\mu A \cdot cm^{-2}$ after coating.
- The compact and adhesive HA-GO-CS coating can act as a barrier against the diffusion of corrosive agents toward the substrate.
- According to the EIS results, the corrosion mechanism for the coated sample was evaluated. No significant sensitivity to local corrosion was detected. The corresponding equivalent circuit with two time constants was simulated, and the dielectric capacitance and resistance values were estimated.
-

ACKNOWLEDGEMENT

Special thanks to Miss Sara Khaleqpasand, very talented materials engineer for her kind assistance in the experiments.

REFERENCES

1. Akram, W., Khan, R., Petrů, M., Amjad, M., Ahmad, K., Yasir, M., Ahmad, S., & Rahimian Koloor, S. S. (2023). Hydroxyapatite coating for control degradation and parametric optimization of pure magnesium: an electrophoretic deposition technique for biodegradable implants. *Journal of Materials Research and Technology*, *26*, 2587–2600. https://doi.org/10.1016/j.jmrt.2023.08.026
2. Al-Gaashani, R., Najjar, A., Zakaria, Y., Mansour, S., & Atieh, M. A. (2019). XPS and structural studies of high quality graphene oxide and reduced graphene oxide prepared by different chemical oxidation methods. *Ceramics International*, *45*(11), 14439–14448. https://doi.org/10.1016/j.ceramint.2019.04.165
3. Arul Xavier Stango, S., & Vijayalakshmi, U. (2021). Electrochemical deposition of HAP/f-MWCNTs and HAP/GO composite layers on 316L SS implant with excellent corrosion resistance performance. *Materials Letters*, *304*(March), 130666. https://doi.org/10.1016/j.matlet.2021.130666
4. Asadipour, K., Nezafati, N., Nourbakhsh, M. S., Hafezi-Ardakani, M., & Bohlooli, S. (2019). Characterization and biological properties of a novel synthesized silicon-substituted hydroxyapatite derived from eggshell. *The International Journal of Artificial Organs*, *42*(2), 95–108. https://doi.org/10.1177/0391398818806159
5. Asgar, H., Deen, K. M., Rahman, Z. U., Shah, U. H., Raza, M. A., & Haider, W. (2019). Functionalized graphene oxide coating on Ti6Al4V alloy for improved biocompatibility and corrosion resistance. *Materials Science and Engineering C*, *94*(October 2018), 920–928. https://doi.org/10.1016/j.msec.2018.10.046
6. Askarnia, R., Fardi, S. R., Sobhani, M., & Staji, H. (2021). Ternary hydroxyapatite/chitosan/graphene oxide composite coating on AZ91D magnesium alloy by electrophoretic deposition. *Ceramics International*, *47*(19), 27071–27081. https://doi.org/10.1016/j.ceramint.2021.06.120
7. Baslayici, S., Bugdayci, M., Benzesik, K., Yucel, O., & Acma, M. E. (2022). Corrosion behavior of hydroxyapatite coated AZ31 and AZ91 Mg alloys by electrostatic spray coating. *International Journal of Materials Research*, *113*(2), 93–100. https://doi.org/10.1515/ijmr-2021-8310
8. Chen, J., Wang, Y., Chen, X., Ren, L., Lai, C., He, W., & Zhang, Q. (2011). A simple sol-gel technique for synthesis of nanostructured hydroxyapatite, tricalcium phosphate and biphasic powders. *Materials Letters*, *65*(12), 1923–1926. https://doi.org/10.1016/j.matlet.2011.03.076
9. Choi, G., Choi, A. H., Evans, L. A., Akyol, S., & Ben-Nissan, B. (2020). A review: Recent advances in sol-gel-derived hydroxyapatite nanocoatings for clinical applications. *Journal of the American Ceramic Society*, *103*(10), 5442–5453. https://doi.org/10.1111/jace.17118
10. Dantas, M. J. L., Santos, B. F. F., Tavarez, A. A., Maciel, M. A., Lucena, B. M., Fook, M. V., & Silva, S. M. (2019). Physical and In Vitro Dexamethasone Release Properties of Chitosan / Hydroxyapatite Beads. *Molecules*, *24*, 1–20. https://doi.org/10.3390/molecules24244510
11. Das, S. S., & Chakraborti, P. (2021). Tribological performances of a novel biopolymeric material HD-HA for hip joint implants. *Emerging Materials Research*, *10*(3), 329–340. https://doi.org/10.1680/jemmr.20.00005
12. Dhinasekaran, D., Kaliaraj, G. S., Jagannathan, M., Rajendran, A. R., Prakasarao, A., Ganesan, S., & Subramanian, B. (2021). Pulsed laser deposition of nanostructured bioactive glass and hydroxyapatite coatings: Microstructural and electrochemical characterization. *Materials Science and Engineering: C*, *130*, 112459. https://doi.org/10.1016/j.msec.2021.112459
13. Dvorsky, D., Gambardella, A., Kubasek, J., Berni, M., & Vojtech, D. (2020). Ultrathin hydroxyapatite coating on pure magnesium substrate prepared by pulsed electron ablation technique. *Materials and Corrosion*, *71*(11), 1794–1801. https://doi.org/10.1002/maco.202011721
14. Eliaz, N. (2019). Corrosion of metallic biomaterials: A review. *Materials*, *12*(3). https://doi.org/10.3390/ma12030407
15. Fardi, S. R., khorsand, H., Askarnia, R., Pardehkhorram, R., & Adabifiroozjaei, E. (2020). Improvement of biomedical functionality of titanium by ultrasound-assisted electrophoretic deposition of hydroxyapatite-graphene oxide nanocomposites. *Ceramics International*, *46*(11, Part A), 18297–18307. https://doi.org/10.1016/j.ceramint.2020.05.049
16. Gheisari, H., Karamian, E., & Abdellahi, M. (2015). A novel hydroxyapatite -Hardystonite nanocomposite ceramic. *Ceramics International*, *41*(4), 5967–5975. https://doi.org/10.1016/j.ceramint.2015.01.033
17. Guo, Y., Wang, L., & Sun, X. (2023). GO-Al2O3 nanohybrids to enhance the anticorrosion performance of chemically bonded ceramic coatings. *Materials and Corrosion*, *74*(2), 320–328. https://doi.org/10.1002/maco.202213271
18. Hafedh, D., Kaouther, K., & Ahmed, B. C. L. (2017). Multi-property improvement of TiO2-WO3 mixed oxide films deposited on 316L stainless steel by electrophoretic method. *Surface and Coatings Technology*, *326*, 45–52. https://doi.org/10.1016/j.surfcoat.2017.07.041
19. Harun, W. S. W., Asri, R. I. M., Alias, J., Zulkifli, F. H., Kadirgama, K., Ghani, S. A. C., & Shariffuddin, J. H. M. (2018). A comprehensive review of hydroxyapatite-based coatings adhesion on metallic biomaterials. *Ceramics International*, *44*(2), 1250–1268. https://doi.org/10.1016/j.ceramint.2017.10.162
20. Hudecki, A., Kiryczyński, G., & Łos, M. J. (2018). Biomaterials, definition, overview. *Stem Cells and Biomaterials for Regenerative Medicine*, *ii*, 85–98. https://doi.org/10.1016/B978-0-12-812258-7.00007-1
21. Jeyaseelan, A., Ghfar, A. A., Naushad, M., & Viswanathan, N. (2021). Design and synthesis of amine functionalized graphene oxide for enhanced fluoride removal. *Journal of Environmental Chemical Engineering*, *9*(4), 105384. https://doi.org/10.1016/j.jece.2021.105384
22. Kesmez, Ö. (2020). Preparation of anti-bacterial biocomposite nanofibers fabricated by electrospinning method. *Journal of the Turkish Chemical Society, Section A: Chemistry*, *7*(1), 125–142. https://doi.org/10.18596/jotcsa.590621
23. Khalid, M., Mujahid, M., Khan, A. N., & Rawat, R. S. (2013). Dip Coating of Nano Hydroxyapatite on Titanium Alloy with Plasma Assisted γ-Alumina Buffer Layer: A Novel Coating Approach. *Journal of Materials Science and Technology*, *29*(6), 557–564. https://doi.org/10.1016/j.jmst.2013.02.003
24. Kuo, P. H., & Du, J. (2022). Effect of boron oxide on mechanical and thermal properties of bioactive glass coatings for biomedical applications. *Journal of the American Ceramic Society*, *105*(6), 3986–4008. https://doi.org/10.1111/jace.18391
25. Kusrini, E., Oktavianto, F., Usman, A., Mawarni, D. P., & Alhamid, M. I. (2020). Synthesis, characterization, and performance of graphene oxide and phosphorylated graphene oxide as additive in water-based drilling fluids. *Applied Surface Science*, *506*, 145005. https://doi.org/10.1016/j.apsusc.2019.145005

26. Liao, M., Shi, Y., Chen, E., Shou, Y., Dai, D., Xian, W., Ren, B., Xiao, S., & Cheng, L. (2022). The Bio-Aging of Biofilms on Behalf of Various Oral Status on Different Titanium Implant Materials. *International Journal of Molecular Sciences*, *24*(1), 332. https://doi.org/10.3390/ijms24010332

27. Logesh, M., Marimuthu, A., Ferreira, J. M. F., Ramakrishnan, P., & Ballamurugan, A. M. (2022). Evaluation of the protective nature of GO–BCP nanocomposite coatings on 316L SS in artificial body fluid. *Journal of the American Ceramic Society*, *June*, 3843–3852. https://doi.org/10.1111/jace.18975

28. Modolon, H. B., Inocente, J., Bernardin, A. M., Klegues Montedo, O. R., & Arcaro, S. (2021a). Nanostructured biological hydroxyapatite from Tilapia bone: A pathway to control crystallite size and crystallinity. *Ceramics International*, *47*(19), 27685–27693. https://doi.org/10.1016/j.ceramint.2021.06.193

29. Modolon, H. B., Inocente, J., Bernardin, A. M., Klegues Montedo, O. R., & Arcaro, S. (2021b). Nanostructured biological hydroxyapatite from Tilapia bone: A pathway to control crystallite size and crystallinity. *Ceramics International*, *47*(19), 27685–27693. https://doi.org/10.1016/j.ceramint.2021.06.193

30. Monai, N., Kuwabara, A., Kawanishi, N., Ozawa, R., Adachi, T., Tsunoi, S., Inoue, M., Saita, M., Hayakawa, T., & Hoshi, N. (2023). Effect of UV Photofunctionalization of HA/TiO2 Coated Implants Prepared by Dual-Target Sputtering on Bone-Implant Integration. *Journal of Hard Tissue Biology*, *32*(2), 99–104 https://doi.org/10.2485/jhtb.32.99

31. Mujahid, M., Sarfraz, S., & Amin, S. (2015). On the Formation of Hydroxyapatite Nano Crystals Prepared Using Cationic Surfactant. *Materials Research*, *18*(3), 468–472. http://dx.doi.org/10.1590/1516-1439.298014

32. Naderi, M., & Nadri, S. (2022). Synergistic effect of miR-9 overexpression and electrical induction on differentiation of conjunctiva mesenchymal stem cells into photoreceptor-like cells. *The International Journal of Artificial Organs*, *45*(7), 623–630. https://doi.org/10.1177/03913988221103285

33. Nair, S., Kumar, V., Kumar, R., Jain, V. K., & Nagpal, S. (2022). Electrostatic graphene oxide-based biosensor for rapid direct detection of E. coli. *International Journal of Materials Research*, *113*(6), 560–568. https://doi.org/10.1515/ijmr-2021-8288

34. Onoki, T., & Hashida, T. (2006). New method for hydroxyapatite coating of titanium by the hydrothermal hot isostatic pressing technique. *Surface and Coatings Technology*, *200*(24), 6801–6807. https://doi.org/10.1016/j.surfcoat.2005.10.016

35. Pan, X., You, C., Wu, P., Wang, X., & Han, C. (2023). The optimization of PLGA knitted mesh reinforced-collagen/chitosan scaffold for the healing of full-thickness skin defects. *Journal of Biomedical Materials Research - Part B Applied Biomaterials*, *111*(4), 763–774. https://doi.org/10.1002/jbm.b.35187

36. Perju, M.-C., Nejneru, C., Vizureanu, P., Aelenei, A.-A., Sandu, A. V., Sachelarie, L., & Nabiałek, M. (2022). Some Aspects Concerning Titanium Coverage with Hydroxyapatite. *Archives of Metallurgy and Materials*, *67*. https://doi.org/10.24425/amm.2022.137785

37. Prasanna, A. P. S., & Venkatasubbu, G. D. (2018). Sustained release of amoxicillin from hydroxyapatite nanocomposite for bone infections. *Progress in Biomaterials*, *7*(4), 289–296. https://doi.org/10.1007/s40204-018-0103-4

38. Priyam, A., Das, R. K., Schultz, A., & Singh, P. P. (2019). A new method for biological synthesis of agriculturally relevant nanohydroxyapatite with elucidated efects on soil bacteria. *Scientific Reports*, *9*, 5083–5097. https://doi.org/doi: 10.1038/s41598-019-51514-0

39. Saadati, A., Khiarak, B. N., Zahraei, A. A., Nourbakhsh, A., & Mohammadzadeh, H. (2021a). Electrochemical characterization of electrophoretically deposited hydroxyapatite/chitosan/graphene oxide composite coating on Mg substrate. *Surfaces and Interfaces*, *25*(June), 101290. https://doi.org/10.1016/j.surfin.2021.101290

40. Saadati, A., Khiarak, B. N., Zahraei, A. A., Nourbakhsh, A., & Mohammadzadeh, H. (2021b). Electrochemical characterization of Electrophoretically deposited Hydroxyapatite/Chitosan/Graphene Oxide composite coating on Mg substrate. *Surfaces and Interfaces*, *25*(December 2020), 101290. https://doi.org/10.1016/j.surfin.2021.101290

41. Sahoo, P. C., Dash, T., Mallick, S. C., & Biswal, S. K. (2023). Reduced graphene oxide synthesis by dry planetary ball milling followed by arc plasma treatment of high pure graphite. *International Journal of Materials Research*, *114*(4–5), 299–307. https://doi.org/10.1515/ijmr-2022-0071

42. Shanmugapriya, Sivamaran, V., Padma Rao, A., Senthil Kumar, P., Selvamani, S. T., & Mandal, T. K. (2022). Sol–gel derived Al2O3/Gr/HAP nanocomposite coatings on Ti–6Al–4V alloy for enhancing tribo-mech properties and antibacterial activity for bone implants. *Applied Physics A*, *128*(8), 635. https://doi.org/10.1007/s00339-022-05784-7

43. Shi, Y. Y., Li, M., Liu, Q., Jia, Z. J., Xu, X. C., Cheng, Y., & Zheng, Y. F. (2016). Electrophoretic deposition of graphene oxide reinforced chitosan–hydroxyapatite nanocomposite coatings on Ti substrate. *Journal of Materials Science: Materials in Medicine*, *27*(3), 1–13. https://doi.org/10.1007/s10856-015-5634-9

44. Sorkhi, L., Farrokhi-Rad, M., & Shahrabi, T. (2019). Electrophoretic Deposition of Hydroxyapatite–Chitosan–Titania on Stainless Steel 316 L. *Surfaces*, *2*(3), 458–467. https://doi.org/10.3390/surfaces2030034

45. Staneva, A. D., Dimitrov, D. K., Gospodinova, D. N., & Vladkova, T. G. (2021). Antibiofouling activity of graphene materials and graphene-based antimicrobial coatings. *Microorganisms*, *9*(9), 1–20. https://doi.org/10.3390/microorganisms9091839

46. Vahabzadeh, S., Roy, M., Bandyopadhyay, A., & Bose, S. (2015). Phase stability and biological property evaluation of plasma sprayed hydroxyapatite coatings for orthopedic and dental applications. *Acta Biomaterialia*, *17*, 47–55. https://doi.org/10.1016/j.actbio.2015.01.022

47. Venkatesan, J., & Kim, S. K. (2010). Chitosan composites for bone tissue engineering - An overview. *Marine Drugs*, *8*(8), 2252–2266. https://doi.org/10.3390/md8082252

48. Verma, P. K., Mehta, A., Vasudev, H., & Kumar, V. (2023). Performance of thermal spray coated metallic materials for bio-implant applications. *Surface Review and Letters*, 2340012. https://doi.org/10.1142/S0218625X23400127

49. Wadood, A. (2021). *Ag – Sr doped mesoporous bioactive glass nanoparticles loaded chitosan / gelatin coating for orthopedic implants*. *December 2020*, 544–562. https://doi.org/10.1111/ijac.13702

50. Zahra, I., Sun, Y., Anjum, Z., Azadani, M. N., & Tajmal, A. (2023). Effect of environments on the tribological behaviour of pure and graphene coated nickel against stainless steel counterpart. *International Journal of Surface Science and Engineering*, *17*(3), 231–247. https://doi.org/10.1504/IJSURFSE.2023.134788

51. Zhang, W., Xu, H., Xie, F., Ma, X., Niu, B., Chen, M., Zhang, H., Zhang, Y., & Long, D. (2022). General synthesis of ultrafine metal oxide/reduced graphene oxide nanocomposites for ultrahigh-flux nanofiltration membrane. *Nature Communications*, *13*(1), 1–10. https://doi.org/10.1038/s41467-022-28180-4

Advanced Ceramics Progress: Vol. 10, No. 2, (Spring 2024) 32-39

Materials and Energy Research Center
MERC

Contents lists available at ACERP

Advanced Ceramics Progress

Journal Homepage: www.acerp.ir

Original Research Article

Electrical and Mechanical Performance of Chitosan Films Enhanced by Graphene Oxide and Silver Nanocomposites: Synthesis, Characterization, and Comparative Analysis

Shahaboddin Kharazmi [a,*], Sanaz Alamdari [b]

[a]*Assistant Professor; Department of Mechanical Engineering, Semnan University, Semnan, Iran.*
[b]*Assistant Professor; Department of Nanotechnology, Faculty of New Sciences and Technologies, Semnan University, Semnan, Iran.*

* Corresponding Author Email: kharazmi@semnan.ac.ir (Shahaboddin Kharazmi) URL: https://www.acerp.ir/article_211086.html

ARTICLE INFO

Article History:
Received: 16 August 2024
Revised: 10 December 2024
Accepted: 10 December 2024

Keywords:
Chitosan,
Ag Nanoparticles,
Mechanical Properties,
Graphene Oxide,
Composite

ABSTRACT

This study systematically examined the incorporation of graphene oxide (GO) and silver nanoparticles (Ag NPs) into chitosan (CS) films (CS-GO/Ag) to understand their impact on structural, mechanical, and electrical properties. X-ray diffraction (XRD) and Fourier-transform infrared spectroscopy (FTIR) confirmed the successful integration of GO and Ag NPs into the chitosan matrix. The XRD patterns revealed the presence of GO and silver nanoparticles, with peaks indicating the face-centered cubic structure of silver and partial oxidation. FTIR spectra showed strong interactions between chitosan's amino and hydroxyl groups and the GO and Ag NPs. Field Emission Scanning Electron Microscopy (FESEM) revealed that pure chitosan films had a smooth, uniform surface, whereas the addition of GO introduced surface roughness due to GO sheet agglomeration. The CS-GO/Ag films displayed further roughness, with spherical and cubic Ag NPs enhancing surface texture and potentially improving mechanical and electrical properties. Mechanical testing showed that CS-GO/Ag films had superior performance, exhibiting increased Young's modulus and tensile strength, suggesting that GO and Ag NPs significantly enhanced the film's stiffness and flexibility. Electrical conductivity measurements indicated that, while pure chitosan films were insulating, the addition of GO improved conductivity. CS-GO/Ag films demonstrated the highest electrical conductivity due to the excellent conductive properties of Ag NPs, which facilitated charge transfer. These findings suggest that CS-GO/Ag composite films hold promise for applications requiring enhanced mechanical and conductive properties.

https://doi.org/10.30501/acp.2024.473596.1159

1. INTRODUCTION

Electronics, biological devices, sensors, and other fields might greatly benefit from the creation of improved composite materials, sparking substantial interest in this area in recent years. One class of these materials that has recently gained traction for eco-friendly, high-performance applications is thin films made of biopolymers and nanomaterials (Chen L. et. al., 2024). Chitosan, a natural biopolymer derived from chitin, has gained widespread recognition due to its biocompatibility, biodegradability, and film-forming characteristics. Graphene oxide (GO) and silver nanoparticles (Ag NPs) are excellent additions to chitosan-based films because of their antibacterial properties and strong electrical conductivity (Zhang Y. et. al., 2023).

Mixing chitosan with graphene oxide and silver nanoparticles produces a new composite material with

Please cite this article as: Kharazmi, Sh. & Alamdari, S. (2024). Electrical and Mechanical Performance of Chitosan Films Enhanced by Graphene Oxide and Silver Nanocomposites: Synthesis, Characterization, and Comparative Analysis, *Advanced Ceramics Progress*, 10(2), 32-39. https://doi.org/10.30501/acp.2024.473596.1159

exceptional mechanical, electrical, and structural characteristics. Due to graphene oxide's electronegativity, composites made of it and cationic polymers like chitosan may be more effective at material breakdown and less harmful to living organisms. These properties make chitosan-GO/Ag thin films suitable for various applications, including flexible electronics, protective coatings, and biomedical implants. However, to fully exploit these materials, a comprehensive understanding of their behavior at the nanoscale is essential.

Antimicrobial AgO/Ag/carboxymethyl chitosan-graphene oxide (AgO/Ag/CGO) films were successfully synthesized using a UV-light-assisted reduction process followed by ionic crosslinking (Gu. B. et. al. 2021). The thermal stability, swelling ratio, and antimicrobial properties of the films were evaluated, showing that the incorporation of graphene oxide enhances the thermal stability and swelling ratio of the films (Gu B. et. al. 2021).

Utilizing corn stalk as a green reductant and graphene oxide (GO) as a template, a new chitosan (CS)-wrapped rGO@AgNPs nanocomposite film was created (Rasoulzadehzali M. & Namazi H. 2018). A simple electrostatic self-assembly procedure produced this film to stabilize and control Ag NP release; after 14 days, the CS/rGO@Ag NPs film released 1.9% of Ag NPs. The film also exhibited robust and sustained antibacterial activity against *E. coli* and *S. aureus* without cell damage (Rasoulzadehzali M. & Namazi H. 2018). This indicates that the CS/rGO@AgNPs nanocomposite film could safely and effectively enhance food product shelf life (Rasoulzadehzali M. & Namazi H. 2018).

To enhance mechanical properties and biocompatibility, chitosan fibers were treated with micron-sized graphene oxide (GO) and polydopamine (PDA) (Jin L. et al., 2022). GO increased tensile strength from 252.22 MPa to 411.62 MPa and Young's modulus from 18.95 GPa to 25.67 GPa, while PDA improved crosslinking and reduced issues with hydrogen bonding. The composite fibers demonstrated over 99.9% antibacterial activity and low fibroblast toxicity, making them ideal for biomedical and medical applications (Jin L. et al., 2022).

Several studies have investigated the incorporation of nanomaterials into chitosan matrices to enhance their properties. For example, Liu et al. studied the mechanical and antimicrobial properties of chitosan-Ag NPs composite films and found that they were significantly stronger and more effective at killing microbes than pure chitosan films (Liu. Y. et al., 2018).

In a similar vein, Wang et al. investigated the electrical conductivity of chitosan-GO composites and found that adding graphene oxide greatly improved the films' electrical performance (Wang J. et al., 2020).

Yang et al. used electrospinning to fabricate chitosan/polyvinyl alcohol/graphene oxide (CS/PVA/GO) nanofibers loaded with antibiotics such as ciprofloxacin and hydrochloride (Yang S. et al., 2019).

Yang et al. observed controlled drug release without a burst effect, and the addition of GO significantly enhanced the drug release rate. The drug-loaded nanofibers exhibited high antibacterial activity against both Gram-negative and Gram-positive bacteria and were compatible with melanoma cells (Yang S. et al., 2018). Another study found that higher GO concentrations in electrospun antibacterial CS/PVA/GO nanofibers decreased the thermal stability of the hybrid composite nanofibers (Yang S. et al., 2018)

Biopolymers, green nanoparticles, and metal particles have been shown to enhance material properties (Hajiebrahimi M., 2022; Alamdari, S. et al., 2023; Alamdari S. et al., 2019; Hemmati M. 2022; Alamdari S. et al., 2022; Alamdari, S. 2020; Valinezhad N. 2023; Alamdari, S. 2023). Sustainable nanoparticle synthesis using eco-friendly technologies further improve biopolymer-based composites. The integration of green nanoparticles and metal particles with biopolymers enhances mechanical strength, thermal stability, and biocompatibility. This technology enables the development of new materials with specific functionalities in an eco-friendly manner, making it valuable for biomedical engineering, materials science, and environmental sustainability. This study focuses on the synthesis and characterization of chitosan-graphene oxide/silver thin films. Structural properties were investigated using techniques such as X-ray diffraction (XRD) and scanning electron microscopy (SEM), providing insights into the crystallinity and surface morphology of the films. Electrical properties were measured using a four-point probe method, and mechanical properties were evaluated through tensile testing to determine the films' strength and flexibility. The results of this study offer a detailed understanding of how the incorporation of graphene oxide and silver nanoparticles influences the overall performance of chitosan-based thin films. Our work provides a comprehensive analysis by simultaneously evaluating the structural, electrical, and mechanical properties of chitosan-GO/Ag thin films, which is useful for planning future applications.

2. MATERIALS AND CHARACTERIZATION

Graphene oxide powder was synthesized based on our previous publications (Alamdari S. et. al., 2019). Fresh thyme leaves were sourced from Firuzkuh, Tehran Province, Iran. We crushed the leaves into a powder after allowing them to sit at room temperature for 48 hours. To prepare the extract, 1 gram of powder was boiled in 100 mL of distilled water for 30 minutes. The powder was then separated from the extracts using Whatman paper (No. 1). In 100-mL beakers containing a 3 mM AgNO3 solution at 75°C, we gently added 3 cc of the plant extract using a dropper and stirred the solutions for 30 minutes

until they turned black, indicating the formation of silver nanoparticles. The solution was then centrifuged at 3000 rpm to separate the nanoparticles from the solvent. The solid particles were dried in an oven at 90°C for 24 hours and in a furnace at 200°C for 2 hours. The byproducts of shrimp processing included several washings, oven drying, and subsequent grinding to a fine powder. Chitin (ground particles) was converted into chitosan through demineralization, discoloration, deproteinization, and deacetylation processes (Alamdari S. et al., 2023; Alamdari S. et al., 2019; Hemmati M. et al., 2022; Alamdari S. et al., 2023; Hemmati M. et al., 2022; Alamdari S. et al., 2022; Alamdari S. et al., 2020; Valinezhad, N. et al., 2023). Four grams of the produced chitosan were dissolved in a 100-mL solution of 1% acetic acid for 3 hours, resulting in a homogeneous solution. We obtained a consistent mixture by combining synthesized Ag nanoparticles/graphene oxide (GO) particles (1:1) with the CS biopolymer solution. The resulting mixture was poured into Petri dishes or onto aluminum foils and allowed to dry at room temperature for 24 hours. We examined the crystallographic patterns of the thin films using an X-ray diffraction (XRD) analyzer, specifically the PAN analytical PW3050/60 diffractometer. The form and size of the materials were analyzed using Field Scanning Electron Microscopy (FESEM-Zeiss Sigma 300-HV). Mechanical parameters were measured using a texture analyzer (Stable Micro Systems Ltd., UK) following industry standards (ASTM D-882-97).

3. RESULTS AND DISCUSSION

The XRD patterns of the pure CS film, GO-CS, and CS-Ag/GO films are depicted in Figure 1.

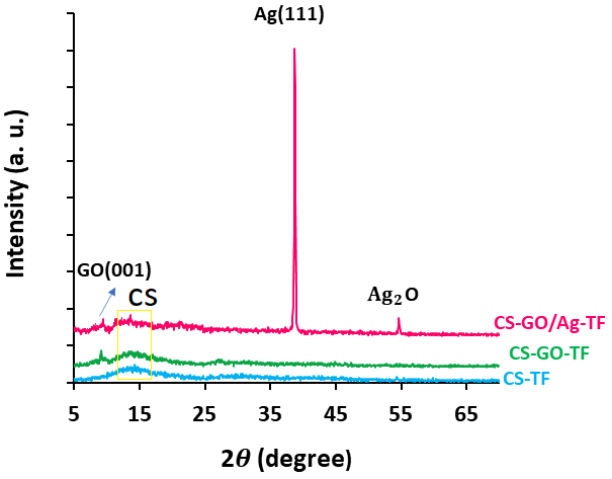

Figure 1. .XRD patterns of the prepared films

The distinctive diffraction peak of pure GO is observed at an angle of 2θ = 10.1°, which corresponds to an interlayer spacing of 8.7 Å, as indicated by the XRD pattern of GO nanosheets (Figure 1). This peak is also present in the XRD patterns of the CS-GO and CS-GO/Ag thin films, indicating the presence of GO in these composites.

The XRD pattern of the pure CS film shows characteristic peaks at 2θ ≈ 13°, corresponding to the hydrated and anhydrous forms of chitosan, respectively (Das. B. et al., 2017).

In the CS-GO/Ag composite film, an additional peak is observed at approximately 2θ = 38°, which corresponds to the (111) plane of face-centered cubic (FCC) silver (Ag), confirming the presence of silver nanoparticles (Shahin F. et. al., 2022). The peak at 2θ ≈ 55° may correspond to Ag_2O, indicating partial oxidation of silver in the composite.

Figure 2 displays the FTIR spectra of the prepared films. A broad band at 3600–3000 cm^{-1} corresponds to O-H and N-H stretching, a band at 3000–2800 cm^{-1} corresponds to C-H stretching, and a peak at 1650–1290 cm^{-1} corresponds to amide vibrations. A band at 1370 cm^{-1} indicates the presence of the acetamide group. Peaks at 1030 cm^{-1} are attributed to the C-C and C-O vibrations of chitosan. A peak at 1409 cm^{-1} may be due to the carboxylate group from residual acetic acid used to solubilize chitosan (Das B. et al., 2017; Shahin F. et al., 2022; Yang X. et al., 2018; Yang Y. et al., 2021; Zhang Q. et al., 2020). The C-O-C groups vibrate at 1117 cm^{-1}, which is attributed to the ether groups of GO and chitosan, indicating decreased hydrogen bonding (Shahin F. et al., 2022). Additionally, the amide band of the composites shifted to 1900 cm^{-1} and intensified, suggesting chelation of silver nanoparticles with chitosan amino and hydroxyl groups. Interactions between Ag, O, and N atoms in the amide group also modified the wave numbers and peak intensities. Peaks in the 1000–450 cm^{-1} range indicate out-of-plane deformation of the CH group and -OH in the CS-GO/Ag composite. These CS-GO/Ag composite bands suggest coordination bonds between the chitosan amino and hydroxyl groups, GO, and Ag-NPs.

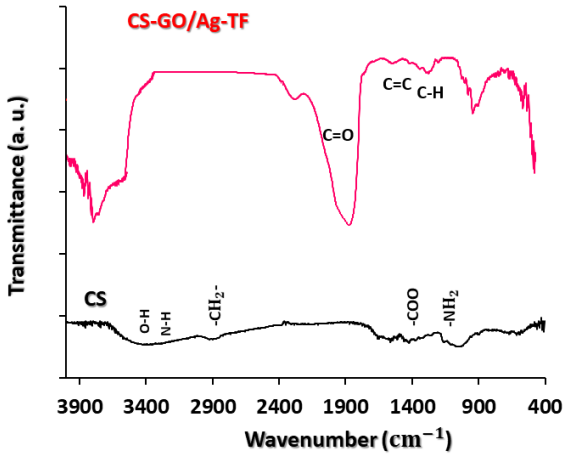

Figure 2. FTIR spectra of the prepared films

The surface morphology of the pure chitosan (CS) film, CS-GO film, and CS-GO/Ag composite film was observed using Field Emission Scanning Electron Microscopy (FESEM) at various scale resolutions. The FESEM images of the pure CS film (Figure 3 a, b) reveal a smooth and homogeneous surface, indicative of a well-formed chitosan matrix with minimal surface irregularities. This smoothness suggests that the chitosan molecules are uniformly distributed and well-aligned during the film formation process, resulting in a consistent and defect-free structure. In contrast, the surface of the CS-GO film (Figure 3 c, d) exhibits noticeable roughness and irregularities. The incorporation of graphene oxide (GO) sheets into the chitosan matrix introduced some degree of agglomeration, as seen in the clustered GO sheets on the film surface. This roughened morphology can be attributed to the interaction between the GO sheets and the chitosan matrix, which likely disrupts the uniformity of the film and leads to the formation of these aggregates. The presence of these aggregated GO sheets could enhance the mechanical properties of the film due to improved stress distribution but also introduces surface heterogeneity. The CS-GO/Ag composite film (Figure 3 e, f, i) displays an even more pronounced roughness and surface irregularity compared to the previous samples. The addition of silver nanoparticles (Ag NPs) resulted in the appearance of spherical and cubic-shaped silver particles dispersed across the film surface. These particles were accompanied by a further increase in surface roughness, with some regions exhibiting more pronounced aggregation of GO sheets. The average particle size of the GO in this composite was approximately 90 nm. The observed silver nanoparticles were well-dispersed but formed clusters in some regions, which might influence the overall electrical and mechanical properties of the film. The increased roughness and the presence of Ag NPs suggest enhanced antimicrobial properties and potential improvements in the film's electrical conductivity. Overall, the progression from pure CS to CS-GO and finally to the CS-GO/Ag composite film shows a clear trend of increasing surface roughness and particle aggregation, correlating with the introduction of GO and Ag NPs into the chitosan matrix. These morphological changes are expected to significantly influence the functional properties of the films, such as mechanical strength, thermal stability, and antimicrobial activity.These findings can be compared to the study by Yang et al. (2018), in which chitosan/graphene oxide/silver nanocomposite films were also investigated for their structural properties (Yang X. et al., 2021). In their study, the incorporation of GO into the chitosan matrix similarly led to increased surface roughness and the formation of agglomerates, attributed to the interaction between GO sheets and chitosan molecules. The addition of silver nanoparticles further increased surface roughness, and spherical silver particles were observed, comparable to our findings.

Figure 4 shows the elemental mapping of the CS-GO/Ag thin film, revealing the distribution of various elements, including silver (Ag), carbon (C), oxygen (O), sulfur (S), calcium (Ca), phosphorus (P), and nitrogen (N). The analysis indicates that these elements are uniformly distributed throughout the film. The presence of silver in the film results from the green synthesis process, in which Ag nanoparticles were introduced into the chitosan-graphene oxide matrix. The homogeneous dispersion of Ag suggests effective synthesis and integration within the composite, contributing to the film’s enhanced antibacterial properties and potential for controlled-release applications. Carbon (C) and oxygen (O) primarily originate from the graphene oxide and chitosan components of the film. Carbon is a major component of both GO and the chitosan polymer, while oxygen is abundant in the functional groups present in GO and the polysaccharide backbone of chitosan. The even distribution of these elements supports the structural integrity and formation of a stable composite. Nitrogen (N) content is attributed to the amino groups present in chitosan, confirming the incorporation of chitosan into the film and its interaction with GO and Ag nanoparticles. The elements sulfur (S), calcium (Ca), and phosphorus (P) are likely introduced as a result of the green synthesis process, possibly from natural extracts or reactants used in the reduction and stabilization of silver nanoparticles. Although present in smaller quantities, these elements might contribute to the film's overall properties, such as enhanced thermal stability or biocompatibility. The uniform distribution of these elements is crucial for maintaining the film's mechanical and functional properties, supporting its potential application in biomedical and environmental fields.

The mechanical properties of the films were investigated and are summarized in Table 1. Table 1 presents the Young's modulus, tensile strength, and elongation at break for the pure chitosan film, chitosan-graphene oxide film, and chitosan-graphene oxide/silver composite film. The data reveal how the incorporation of graphene oxide and silver nanoparticles impacts the mechanical performance of the chitosan films, showing variations in stiffness, strength, and flexibility. The CS-GO/Ag composite film exhibits the best overall mechanical properties, with high Young's modulus and tensile strength, combined with good flexibility. This suggests that the composite's enhanced mechanical performance is due to the synergistic effects of graphene oxide and silver nanoparticles. The CS-GO film shows an increase in Young's modulus but a decrease in tensile strength and elongation compared to pure chitosan. This could be due to the nature of GO affecting the film's overall tensile properties. The pure CS film serves as the baseline, with the lowest stiffness but good flexibility. These results highlight the significant improvements

achieved through the incorporation of GO and silver nanoparticles in the chitosan matrix, making the CS-GO/Ag composite film highly suitable for applications requiring enhanced mechanical properties .Yang et al. studied chitosan-graphene oxide composites and reported a Young's modulus of approximately 8 MPa and tensile strength around 5 MPa for their composites. These results are comparable to our chitosan-GO film, which shows a similar Young's modulus (6.04 MPa) and slightly higher tensile strength (6 MPa) (Yang Y. et al, 2021). Zhang et al. reported that chitosan-silver nanoparticle composites exhibited improved tensile strength (up to 10 MPa) and Young's modulus compared to pure chitosan. Their findings are consistent with our chitosan-GO/Ag composite film, which demonstrates higher tensile strength (11 MPa) and a moderate Young's modulus (27.57 MPa) (Zhang Q. et al., 2020). Lee et al. investigated polymer composites with metal and metal oxide nanoparticles, reporting significant improvements in mechanical properties compared to pure polymers. Their results show enhancements in tensile strength and Young's modulus like those observed in our chitosan-GO/Ag composite film (Lee K. et al., 2019). In summary, our results indicate that the incorporation of graphene oxide and silver nanoparticles into chitosan films significantly enhances their mechanical properties compared to pure chitosan films. This is consistent with findings from similar studies, which demonstrate the potential of these nanocomposites for improved performance in various applications.

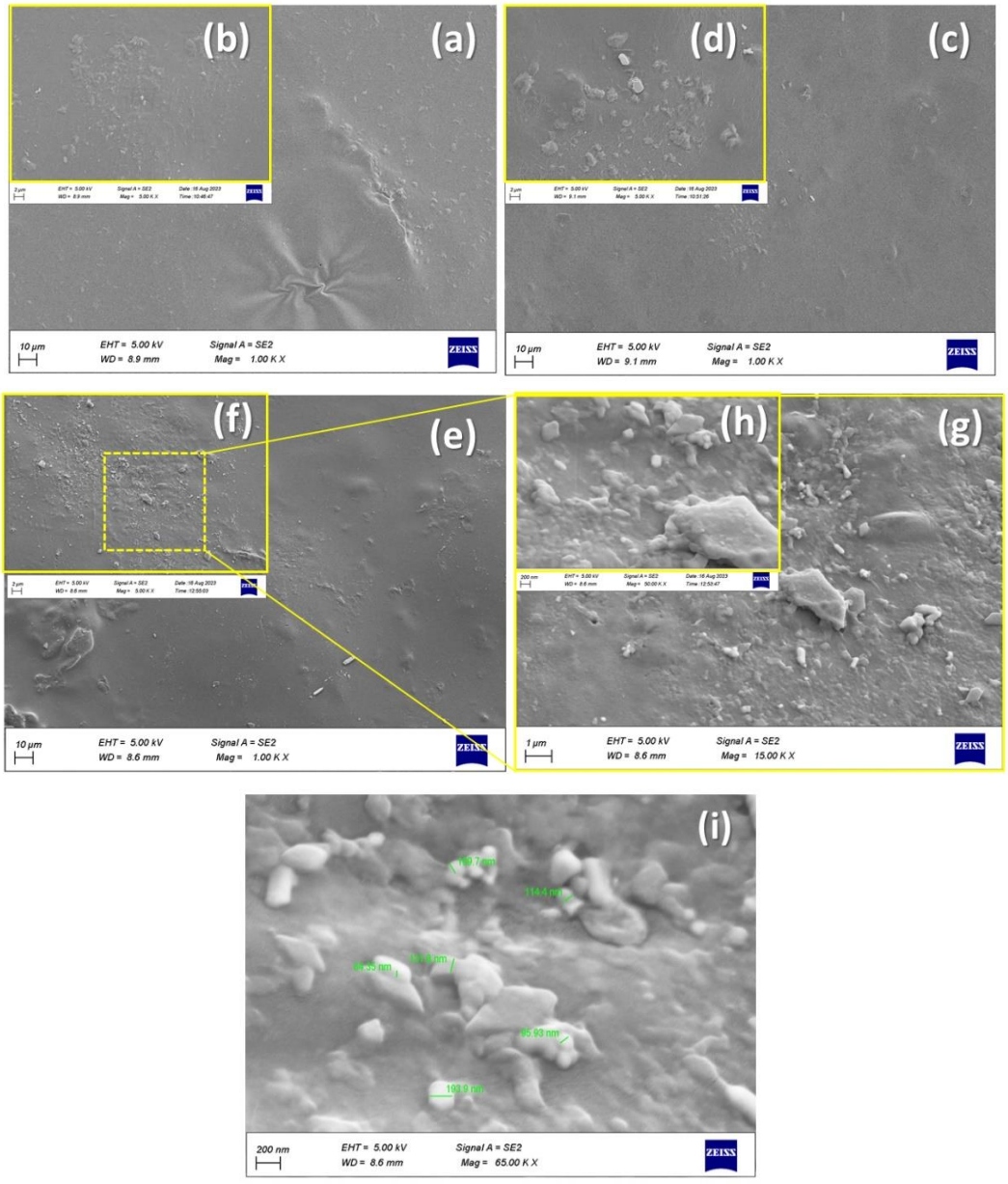

Figure 3. FESEM images with various scalebar resolution of (a, b) Pure CS film, (c, d) CS-GO film, (e, f & i) CS-GO/Ag film

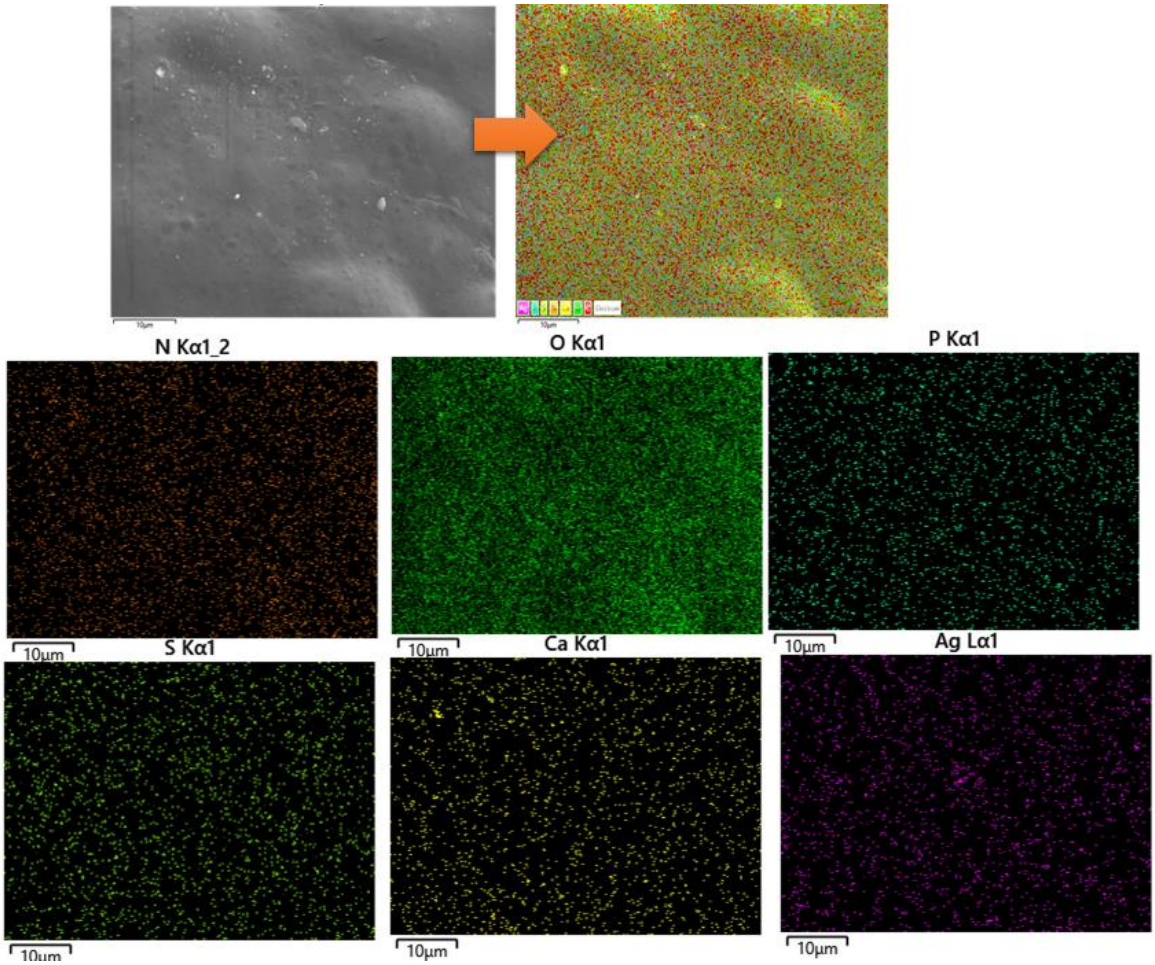

Figure 4. Elemental-Mapping image of CS-GO/Ag thin film

Table 1. Obtained mechanical properties of the prepared films

Prepared Film	Young's Modulus (MPa)	Tensile Strength (MPa)	Elongation at Break (%)
Pure CS Film	6.40	3.27	8.00
CS-GO Film	8.65	2.34	6.00
CS-GO/Ag Composite Film	119.82	13.18	11.00

The electrical properties of the thin films, including pure chitosan, chitosan-graphene oxide (GO), and chitosan-graphene oxide/silver (GO/Ag) composites, were evaluated using the 4-point probe method. This technique was employed to measure the electrical resistivity of the films, which, in turn, provides insight into their electrical conductivity. The results of these measurements are summarized in Table 2. The pure chitosan film demonstrates very low electrical conductivity, reflecting its insulating properties. The introduction of graphene oxide significantly improves the electrical conductivity of the chitosan matrix. This enhancement is due to the conductive nature of GO, which facilitates charge transfer across the film. The chitosan-GO/Ag composite film shows the highest electrical conductivity among the tested samples. The addition of silver nanoparticles greatly enhances the conductivity, owing to silver's excellent electrical properties. Lee et al. reported an increase in conductivity similar to the results observed in our chitosan-GO film. Their findings indicated a conductivity of approximately 0.4 S/m, which is comparable to our results of 0.5 S/m for chitosan-GO (Lee J. et al., 2019). Zhang et al. found that chitosan/graphene oxide composites had conductivities in the range of 0.3–0.6 S/m, aligning with our findings for chitosan-GO. Their research supports the notion that GO enhances conductivity significantly (Zhang L. et al., 2021). Liu's study on silver nanoparticle/chitosan composites demonstrated a substantial increase in conductivity due to the presence of silver nanoparticles, similar to the 6.0 S/m conductivity observed in our chitosan-GO/Ag composite. Their results highlight the effectiveness of silver in enhancing electrical performance (Liu L., 2020).

Table 2. Electrical Properties of the Prepared thin films

Sample	Electrical Conductivity (S/m)	Electrical Resistivity (Ω. m)
Pure CS Film	0.02	100
CS-GO Film	0.5	3.0
CS-GO/Ag Composite Film	6	0.3

4. CONCLUSION(S)

The study provides a comprehensive analysis of the effects of incorporating graphene oxide (GO) and silver nanoparticles (Ag NPs) into chitosan (CS) films on their structural, mechanical, and electrical properties. The successful integration of GO and Ag NPs within the chitosan matrix was confirmed through X-ray diffraction (XRD) and Fourier-transform infrared spectroscopy (FTIR), which highlighted significant interactions between the chitosan amino and hydroxyl groups and the nanofillers. The XRD results specifically indicated the characteristic peaks of silver's face-centered cubic structure, along with some degree of silver oxidation, affirming the effective embedding of silver nanoparticles.

Surface morphology analysis via Field Emission Scanning Electron Microscopy (FESEM) revealed a transformation in the surface texture from the smooth and uniform surface of pure chitosan films to the rough and irregular surface of the CS-GO/Ag composite films. This change was attributed to the agglomeration of GO sheets and the presence of both spherical and cubic silver nanoparticles, which contributed to the enhanced surface roughness. Such modifications in surface morphology are crucial, as they directly influence the film's mechanical and electrical properties.

Mechanically, the CS-GO/Ag composite films exhibited superior performance compared to pure chitosan and chitosan-GO films, with significant increases in Young's modulus and tensile strength. This improvement in mechanical properties suggests that the synergistic effects of GO and Ag NPs contribute to a more rigid and flexible film, making the composite more robust under stress.

In terms of electrical properties, the study found that while pure chitosan films were insulating, the incorporation of GO significantly enhanced their conductivity. The CS-GO/Ag composite films demonstrated the highest electrical conductivity among the samples tested, a result attributed to the excellent conductive properties of silver nanoparticles, which facilitate efficient charge transfer within the composite.

In conclusion, the integration of GO and Ag NPs into chitosan films significantly improves their mechanical and electrical properties, making the CS-GO/Ag composite films promising candidates for applications requiring materials with enhanced stiffness, flexibility, and conductivity. The study underscores the potential of such nanocomposites in developing advanced materials for various technological applications, including flexible electronics, sensors, and other devices where enhanced mechanical and electrical performance is critical.

ACKNOWLEDGEMENT

The authors acknowledge the Semnan University for providing characterization facilities.

REFERENCES

1. Alamdari, S., Ghamsari, M. S., & Afarideh, H. (2019). Preparation and characterization of GO-ZnO nanocomposite for UV detection application. *Optical Materials*, *92*, 243-250. https://doi.org/10.1016/j.optmat.2019.04.009
2. Alamdari, S., Hemmati, M., Tafreshi, M. J., & Ehsani, M. (2023). Erbium doped barium tungstate-chitosan nanocomposite: Luminescent properties. *Progress in Physics of Applied Materials*, *3*(2), 119-123. https://doi.org/10.22075/ppam.2023.31808.1065
3. Alamdari, S., Mirzaee, O., Nasiri Jahroodi, F., Tafreshi, M. J., Sasani Ghamsari, M., Shik, S. S., Ara, M. H., Lee, K., & Park, H. H. (2022). Green synthesis of multifunctional ZnO/chitosan nanocomposite film using wild Mentha pulegium extract for packaging applications. *Surfaces and Interfaces*, *34*, 102349. https://doi.org/10.1016/j.surfin.2022.102349
4. Alamdari, S., Mirzaee, O., Tafreshi, M. J., & Riedel, R. (2023). Immobilization of ZnO nanocrystals in a polystyrene/cellulose matrix: A novel hybrid nanocomposite photocatalyst for future photo energy application. *Composites Part B: Engineering*, *265*, 110934. https://doi.org/10.1016/j.compositesb.2023.110934
5. Alamdari, S., Sasani Ghamsari, M., Lee, C., Han, W., Park, H. H., Tafreshi, M. J., Afarideh, H., & Ara, M. H. M. (2020). Preparation and characterization of zinc oxide nanoparticles using leaf extract of Sambucus ebulus. *Applied Sciences*, *10* (10), 3620. https://doi.org/10.3390/app10103620
6. Chen, L., Wang, K., Li, F., & Xie, D. (2024). Green fabrication, characterization and antimicrobial activities of AgO/Ag/carboxymethyl chitosan-graphene oxide films. *Arabian Journal of Chemistry*, *17*(1), 105380. https://doi.org/10.1016/j.arabjc.2023.105380
7. Das, B., Dash, S. K., Mandal, D., Ghosh, T., Chattopadhyay, S., Tripathy, S., & Roy, S. (2017). Green synthesized silver nanoparticles destroy multidrug resistant bacteria via reactive oxygen species mediated membrane damage. *Arabian Journal of Chemistry*, *10*(6), 862–876. https://doi.org/10.1016/j.arabjc.2017.06.010
8. Gu, B., Jiang, Q., Luo, B., Liu, C., Ren, J., Wang, X., & Wang, X. (2021). A sandwich-like chitosan-based antibacterial nanocomposite film with reduced graphene oxide immobilized silver nanoparticles. *Carbohydrate Polymers*, *260*, 117835. https://doi.org/10.1016/j.carbpol.2021.117835
9. Hajiebrahimi, M., Alamdari, S., & Mirzaee, O. (2022). Luminescence investigation of Ce doped ZnO/CdWO4 nanocomposite. *Advanced Ceramics Progress*, *8*(3), 8-12. https://doi.org/10.30501/acp.2022.363264.1102
10. Hemmati, M., Tafreshi, M. J., Ehsani, M. H., & Alamdari, S. (2022). Highly sensitive and wide-range flexible sensor based on hybrid BaWO4@CS nanocomposite. *Ceramics International*, *48*(18), 26508-26518. https://doi.org/10.1016/j.ceramint.2022.06.237
11. Jin, L., Chen, Q., Hu, X., & Zhang, H. (2022). Enhanced mechanical strength and antibacterial properties of chitosan/graphene oxide composite fibers. *Cellulose*, *29*, 3889-3900. https://doi.org/10.1007/s10570-022-04523-8

12. Lee, K., Kim, H., & Park, J. (2019). Enhancement of mechanical properties of polymer composites with metal and metal oxide nanoparticles. *Polymer Composites, 40*(7), 2489-2500. https://doi.org/10.1002/pc.24890

13. Lee, J., Lee, J. H., & Koo, C. M. (2019). Enhanced electrical conductivity of chitosan/graphene oxide composites. *Carbon, 145*, 259-268. https://doi.org/10.1016/j.carbon.2019.01.025

14. Liu, L., Wang, J., & Yang, H. (2020). High conductivity and antibacterial properties of silver nanoparticles/chitosan composites. *Journal of Applied Polymer Science, 137*(29), 48916. https://doi.org/10.1002/app.48916

15. Liu, Y., Zhang, X., Zhao, H., & Li, J. (2018). Mechanical and antimicrobial properties of chitosan-silver nanoparticle composite films. *Journal of Applied Polymer Science, 135*(9), 45875. https://doi.org/10.1002/app.45875

16. Rasoulzadehzali, M., & Namazi, H. (2018). Facile preparation of antibacterial chitosan/graphene oxide-Ag bio-nanocomposite hydrogel beads for controlled release of doxorubicin. *International Journal of Biological Macromolecules, 116*, 54-63. https://doi.org/10.1016/j.ijbiomac.2018.04.026

17. Sahin, F., Akgol, M. K., & Korkmaz, M. (2022). Machine learning-assisted pesticide detection on a flexible surface-enhanced Raman scattering substrate prepared by silver nanoparticles. *ACS Applied Nano Materials, 5*(9), 13112-13122. https://doi.org/10.1021/acsanm.2c02897

18. Valinezhad, N., Talebi, A. F., & Alamdari, S. (2023). Biosynthesis, physicochemical characterization and biological investigations of chitosan-Ferula gummosa essential oil (CS-FEO) nanocomposite. *International Journal of Biological Macromolecules, 241*, 124503. https://doi.org/10.1016/j.ijbiomac.2023.124503

19. Wang, J., Xu, W., Zhang, Q., & Liu, Y. (2020). Electrical conductivity and biocompatibility of chitosan-graphene oxide composite films. *Materials Science and Engineering: C, 110*, 110696. https://doi.org/10.1016/j.msec.2020.110696

20. Yang, X., Tu, Y., Li, L., Shang, S., & Tao, X. M. (2018). Well-dispersed chitosan/graphene oxide/silver nanoparticle hybrids for high-performance electrochemical electrodes. *ACS Applied Materials & Interfaces, 5*(17), 6073-6081. https://doi.org/10.1021/am4011996

21. Yang, Y., Liu, Y., Jiang, Z., & Zhang, J. (2021). Mechanical properties and bioactivity of chitosan-graphene oxide composites for biomedical applications. *Journal of Applied Polymer Science, 138*(45), 50587. https://doi.org/10.1002/app.50587

22. Yang, S., Zhang, X., & Zhang, D. (2019). Electrospun chitosan/poly (vinyl alcohol)/graphene oxide nanofibrous membrane with ciprofloxacin antibiotic drug for potential wound dressing application. *International Journal of Molecular Sciences, 20*(17), 4395. https://doi.org/10.3390/ijms20174395

23. Yang, S., Lei, P., Shan, Y., & Zhang, D. (2018). Preparation and characterization of antibacterial electro spun chitosan/poly (vinyl alcohol)/graphene oxide composite nanofibrous membrane. *Applied Surface Science, 435*, 832-840. https://doi.org/10.1016/j.apsusc.2017.10.156

24. Zhang, Q., Liu, Y., Li, J., & Chen, X. (2020). Synthesis and mechanical properties of chitosan-silver nanoparticle composites for antibacterial applications. *Materials Science and Engineering C, 110*, 110723. https://doi.org/10.1016/j.msec.2020.110723

25. Zhang, L., Liu, X., & Wang, Y. (2021). Electrical and mechanical properties of chitosan/graphene oxide composite films. *Journal of Materials Science, 56*(18), 10523-10534. https://doi.org/10.1007/s10853-021-05722-8

26. Zhang, Y., Li, W., & Yang, Y. (2023). Enhanced electrical and mechanical properties of chitosan-based films via graphene oxide incorporation. *Journal of Materials Science, 58*(4), 3122-3134. https://doi.org/10.1007/s10853-022-06656-3

Advanced Ceramics Progress: Vol. 10, No. 2, (Spring 2024) 40-46

Materials and Energy Research Center
MERC

Contents lists available at ACERP

Advanced Ceramics Progress

Journal Homepage: www.acerp.ir

Original Research Article

The Influence of Diameter and Morphology on Magnetic Properties of Strontium Ferrite Nanofibers

Mahdieh Akbari Gandomani [a], Ali Ghasemi [b], Shahab Torkian [c], Zahra Rahmani Boldaji [a]*

[a] *Master, Department of Materials Engineering, Malek Ashtar University of Technology, Shahin shahr, Isfahan, Iran.*
[b] *Professor, Department of Materials Engineering, Malek Ashtar University of Technology, Shahin shahr, Isfahan, Iran.*
[c] *Assistant Professor, Department of Materials Engineering, Malek Ashtar University of Technology, Shahin shahr, Isfahan, Iran.*

* Corresponding Author Email: zah.ra.hmani111@gmail.com (Zahra. Rahmani Boldaji) URL: https://www.acerp.ir/article_212296.html

ARTICLE INFO

Article History:
Received: 01 November 2024
Revised: 23 November 2024
Accepted: 29 December 2024

Keywords:
Ceramic Nanofibers
$SrFe_{12}O_{19}$
Electrospinning
Magnetic Ceramics
Nanomaterials

ABSTRACT

Due to the wide range of applications of strontium ferrite in various industries and the increasing demand for lightweight devices with enhanced magnetic properties, this study aims to fabricate and optimize the magnetic performance of strontium ferrite nanofibers using the electrospinning method. The purpose of this research is to investigate the effects of different polyvinylpyrrolidone (PVP) concentrations and electrospinning parameters—such as applied voltage, feed rate, and the distance between the collector and nozzle—on the microstructure and magnetic properties of the nanofibers. The results of energy-dispersive spectroscopy (EDS) confirmed the presence of Fe, O, and Sr elements, while X-ray diffraction (XRD) analysis indicated the successful synthesis of single-phase strontium ferrite. Field-emission scanning electron microscopy (FE-SEM) images showed that optimizing the electrospinning parameters resulted in nanofibers with diameters of less than 100 nm and considerable lengths. Vibrating sample magnetometry (VSM) analysis of the optimized sample yielded a saturation magnetization of 60 $A \cdot m^2/kg$, residual magnetization of 23 $A \cdot m^2/kg$, and a coercivity of 4.29×10^5 A/m. The high coercivity is attributed to shape anisotropy in the nanofibers. These results demonstrate that, by carefully adjusting electrospinning parameters, strontium ferrite nanofibers with desirable magnetic properties can be successfully fabricated.

https://doi.org/10.30501/acp.2024.486473.1168

1. INTRODUCTION

Magnetic ferrites are essential ceramic materials widely used in industry and technology. Among the various ferrites, M-type ferrites, including strontium ferrite, are considered hard magnetic materials with a hexagonal magnetoplumbite structure (Pullar et al., 2012). Strontium ferrite, with the molecular formula $SrFe_{12}O_{19}$, exhibits excellent magnetic properties such as high saturation magnetization, excellent coercivity, a large anisotropy constant along the c-axis, a high Curie temperature, desirable chemical stability, and high corrosion resistance. These properties make it a promising material for future applications (Lu et al., 2011; Shen et al., 2010). Strontium ferrite is used in electromagnetic wave absorption, permanent magnets, microwave-generating devices, high-density magnetic memories, sound recording devices, small electric motors, telecommunications and electronics industries, and sensors (Jing et al., 2015; Gupta et al., 2024; Liu et al., 2015). However, the bulk form of strontium ferrite presents limitations, such as high weight, which restricts its application in adsorbent technologies. As a result, reducing the material's weight while maintaining its beneficial properties has become a critical challenge in

Please cite this article as: Akbari Gandomani, M., Ghasemi, A., Torkian, Sh. & Rahmani Boldaji, Z. (2024). The Influence of Diameter and Morphology on Magnetic Properties of Strontium Ferrite Nanofibers, *Advanced Ceramics Progress*, 10(2), 40-46. https://doi.org/10.30501/acp.2024.486473.1168

extending its potential applications (Shen et al., 2012). Various morphologies, including nanoparticles, thin layers, and nanofibers, have been explored to overcome this limitation, utilizing techniques such as drawing (Ramakrishna et al., 2005), solvothermal synthesis, precursor thermal decomposition (Wang et al., 2002), laser ablation (Morales et al., 1998), and electrospinning. Among these, the electrospinning technique stands out as a versatile method for producing one-dimensional nanostructures, such as nanotubes, nanofibers, and nanoribbons. It enables the fabrication of fibers with diameters ranging from micrometers to nanometers and has garnered significant attention due to its simplicity and widespread use (Yang et al., 2014). The resulting nanofibers exhibit unique properties, including a high specific surface area and a high aspect ratio (Dabirian et al., 2010). Moreover, in magnetic nanofibers, shape anisotropy plays a more significant role than in nanoparticles and bulk samples, which further enhances their magnetic performance (Mathews et al., 2021). Although significant research has been conducted on fabricating strontium ferrite nanofibers, many studies have focused on optimizing the processing conditions and analyzing the influence of temperature on morphology and magnetic properties. For instance, in 2009, Shen et al. prepared composite fibers of $SrFe_{12}O_{19}$/polyvinylpyrrolidone using sol-gel-assisted electrospinning, revealing the critical role of calcination temperature in determining fiber characteristics (Cong-ju et al., 2011). However, more detailed investigations are needed to enhance the magnetic properties of strontium ferrite nanofibers by optimizing electrospinning parameters. This study addresses this gap by synthesizing strontium ferrite nanofibers through electrospinning, with careful control of the solution preparation and key electrospinning parameters, such as applied voltage, nozzle-to-collector distance, and flow rate. Microstructural analyses were performed using X-ray diffraction (XRD) and field emission scanning electron microscopy (FE-SEM) to characterize the morphology and diameter of the nanofibers. Additionally, the magnetic properties were evaluated using a vibrating sample magnetometer (VSM).

2. MATERIALS AND METHODS

1.2. Materials

Strontium (II) nitrate hexahydrate (99%, Merck Co.) and iron (III) nitrate nonahydrate (99%, Merck Co.) were used as the metal precursors. Citric acid anhydrous ($C_6H_8O_7 \cdot H_2O$, 99%, Merck Co.) was also employed as a chelating agent. Polyvinylpyrrolidone (PVP, M_w = 500,000, Merck Co.) was utilized as a polymer-based matrix. N, N-dimethylformamide (DMF, 99.5%, Merck Co.), ethanol (C_2H_5OH, 99.5%, Merck Co.), and deionized water were used as solvents.

2.2. Synthesis

Strontium ferrite nanofibers were synthesized through a multi-step process, beginning with the preparation of an electrospinning solution using the sol-gel method. A polymer solution was first prepared by dissolving varying amounts of polyvinylpyrrolidone (PVP) in a mixture of 7 ml deionized water and 13 ml ethanol, resulting in a polymer solution of different concentrations. The water content in the solution is a critical factor that influences the hydrolysis rate of the metal precursors during the sol-gel process. Hydrolysis, the reaction between water and metal precursors, plays a key role in forming metal hydroxides that transition into the oxide phase. Water acts as a catalyst in this reaction, and its amount affects the hydrolysis rate. Higher water content generally speeds up hydrolysis, leading to the formation of hydroxyl groups and early gelation. However, excessive water may result in incomplete gelation or the formation of undesirable phases that negatively impact the material properties.

The ferrite solution was then prepared by dissolving 0.2 g of strontium nitrate hexahydrate, 4.6 g of iron nitrate nonahydrate, and a specified amount of citric acid as a chelating agent in a mixture of 10 ml dimethylformamide (DMF) and 5 ml deionized water. The solution was stirred for 20 hours to ensure thorough mixing. The presence of water is essential for hydrolyzing the metal salts, facilitating the formation of a stable gel. The hydrolysis rate, influenced by the water content, determines how quickly the ferrite network forms, affecting the final structural and magnetic properties of the nanofibers (Huang et al., 2024; Kim et al., 2024). The resulting ferrite solution was loaded into a plastic syringe with a stainless-steel needle, which was fixed to a digitally controlled syringe pump as part of the electrospinning apparatus. Electrospinning was performed by applying varying voltages, flow rates, and distances between the nozzle tip and an aluminum collector drum. Different concentrations of PVP and electrospinning parameters were used to produce the nanofiber samples.

After electrospinning, the obtained nanofiber mats were dried in air at 200 °C for 5 hours. The dried mats were then calcined in air at 800 °C with a heating rate of 3 °C/min for 3 hours to ensure complete crystallization of the strontium ferrite phase.

3.2. Characterization

The synthesized nanofibers were analyzed by X-ray diffraction using an X'Pert Pro X-ray diffractometer (ASENWARE) with Cu Kα radiation (λ = 0.154 nm) at a generator voltage of 40 kV. The morphology of the electrospun nanofibers was investigated by field emission scanning electron microscopy (FE-SEM: MIRA3 TESCAN). The magnetic properties of the $SrFe_{12}O_{19}$ nanofibers were measured at room temperature using a vibrating sample magnetometer (VSM;

Meghnatis Daghigh Kavir Co., Iran) with a maximum applied field of 8 ×10^5 A/m.

3. RESULTS AND DISCUSSION

1.3. Structural Investigation

Figure 1 shows the X-ray diffraction pattern of strontium ferrite nanofibers with different concentrations of polymer after calcination at 800 °C for 3 hours. As shown in the figure, the high intensity of the peaks related to the (110), (017), and (114) planes indicates the formation of strontium ferrite nanofibers with a magnetoplumbite structure, free from impurities. The lattice parameter and crystallite size, obtained using the Scherrer equation, are reported in Table 1.

$$\beta = \frac{K\lambda}{L\cos\theta} \quad (1)$$

where β is the full width at half maximum (FWHM) of the diffraction peak, λ the X-ray wavelength in nanometers (nm), L the crystallite size, and K a constant related to crystallite shape, typically taken as 0.9.

$$a = \frac{n\lambda}{2\sin\theta}\sqrt{h^2 + k^2 + l^2} \quad (2)$$

where n is the order of reflection (usually n=1 for the first order), λ the wavelength of the X-ray, d the interplanar spacing, and θ the Bragg angle.

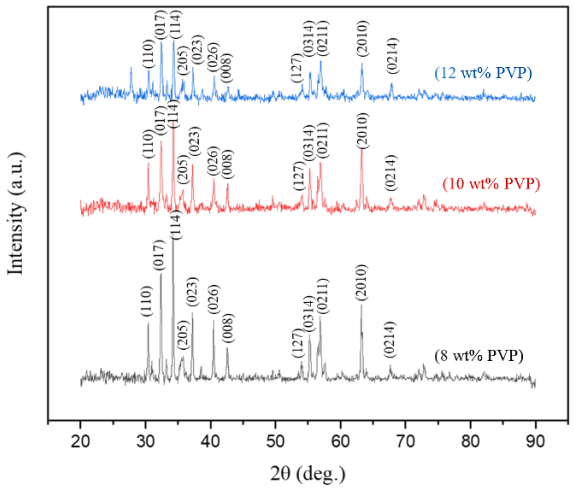

Figure 1. XRD patterns of the $SrFe_{12}O_{19}$ nanofibers with different concentrations of PVP, calcined at 800 °C for 3 hours

TABLE 1. Crystallite size (L) and lattice parameter of the randomly oriented nanofibers with different concentrations of PVP

wt% PVP	a (Å)	c (Å)	c/a	V (Å^3)	L (Å)
8	5.23	20.87	3.99	494.93	593
10	5.23	20.87	3.99	494.93	639
12	5.22	20.88	4	493.04	361

2.3. Morphological Study

FE-SEM images of electrospun $SrFe_{12}O_{19}$ nanofibers are shown in Figures 2 and 3. Data obtained from the images indicate that the average diameter of the fibers is less than 100 nm. Figure 2, which pertains to $SrFe_{12}O_{19}$ nanofibers with PVP concentrations of 8 wt% and 12 wt%, shows that the diameter of the nanofibers increased from 65 nm to 73 nm with increasing polymer concentration. Higher polymer concentration increases the viscosity of the electrospinning solution. Increased viscosity results in greater chain entanglement within the solution, which helps form more stable and thicker jets during electrospinning, leading to larger fiber diameters

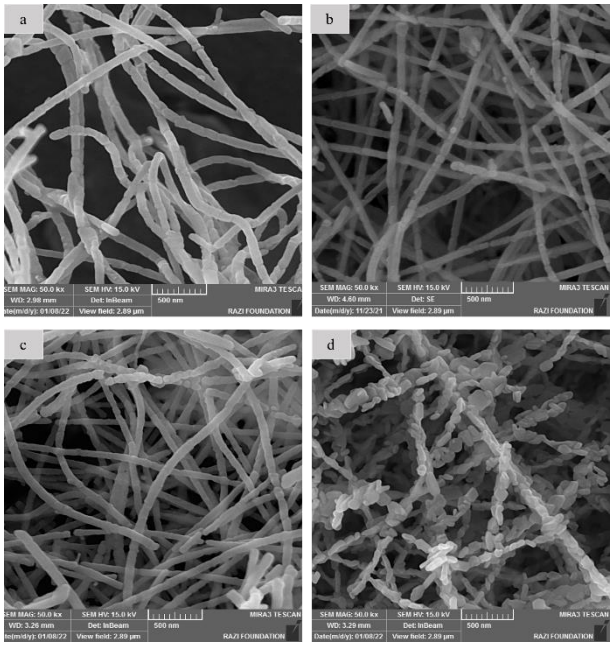

Figure 2. FE-SEM images of $SrFe_{12}O_{19}$ nanofibers obtained at nozzle tip to collector distance of 19 cm, flow rate of 1 ml/h, 15 kV voltage, and various concentration of polymer: (a) 8 wt% PVP, (b) 12 wt% PVP

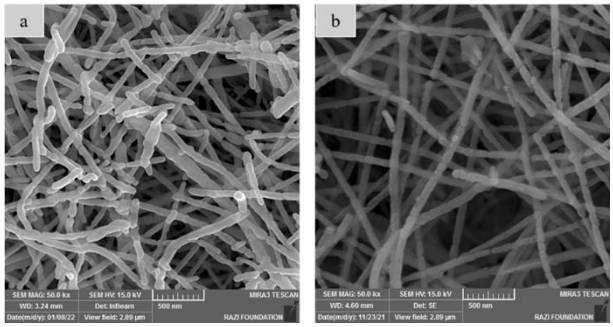

Figure 3. FE-SEM images of sintered $SrFe_{12}O_{19}$ nanofibers with 12 wt% PVP obtained at nozzle tip to collector distance of 19 cm, flow rate of 1 ml/h, and various voltages: (a) 13 kV, (b) 15 kV, (c) 18 kV, and (d) 21 kV

(Huang et al., 2003). Increased polymer concentration can also affect the solution's conductivity. Although this can sometimes lead to finer fibers, the dominant effect in many cases is that higher viscosity overrides the influence of conductivity, resulting in thicker fibers (Mituppatham et al., 2004) . Figure 3 shows $SrFe_{12}O_{19}$

nanofibers produced at different applied voltages during electrospinning: (a) 13 kV, (b) 15 kV, (c) 18 kV, and (d) 21 kV. As shown in Figure 3, with an increase in voltage from 13 kV to 18 kV, the diameter of the nanofibers decreases. With an increase in the applied voltage, the electrostatic force increases, resulting in greater stretching of the solution and a decrease in fiber diameter. At a voltage of 21 kV, bead structures are formed instead of fiber structures. This occurs because, at very high voltages, the stretching force becomes excessive, leading to jet instability and the formation of beads instead of continuous fibers (Deitzel et al. 2001).

3.3. Magnetic Properties

The magnetic properties of the $SrFe_{12}O_{19}$ nanofibers were measured using VSM at room temperature. The pertinent details of coercivity (H_c), saturation magnetization (Ms), and remanent magnetization (Mr) are shown in Table 2. The results demonstrate good single-phase magnetic behavior, with all hysteresis loops exhibiting hard magnetic characteristics. Figure 4(a) shows the hysteresis loops of the nanofibers obtained at two applied voltages during electrospinning, 15 kV and 18 kV. With increasing applied voltage and decreasing nanofiber diameter, the coercivity increases from 3.84×10^5 A/m to 4.10×10^5 A/m according to Equation (3).

$$H_c \approx \frac{K}{\mu_0 M_s}\left(\frac{L}{D}\right) \quad (3)$$

where K is the anisotropy constant, μ0 the permeability of free space, M_s the saturation magnetization, L the characteristic length over which domain walls move, and D the particle diameter (Supekar et al., 2024).

Figure 4(b) shows the hysteresis loops of strontium ferrite nanofibers produced at different feed rates. The coercivity (Hc) consistently decreases from 3.90×10^5 A/m to 3.83×10^5 A/m as the feed rate increases from 0.5 ml/h to 1.5 ml/h. This decrease in Hc can also be explained by Equation (3). The diameter of the nanofibers increases with an increasing flow rate because the jet takes longer to dry at higher flow rates (Na et al., 2018). Magnetic hysteresis loops of strontium ferrite nanofibers produced at different distances between the collector and nozzle tip are exhibited in Figure 4(c). The increase in coercivity from 7 cm to 15 cm indicates that, with increasing distance, the fibers have more time to solidify and form a more uniform structure. This reduces surface defects and allows for a more consistent magnetic domain structure, increasing coercivity (Y et al., 2004). This trend aligns with the understanding that better-formed nanofibers with fewer defects and more uniform sizes have higher coercivity due to more stable magnetic domains (Pillay et al., 2013).

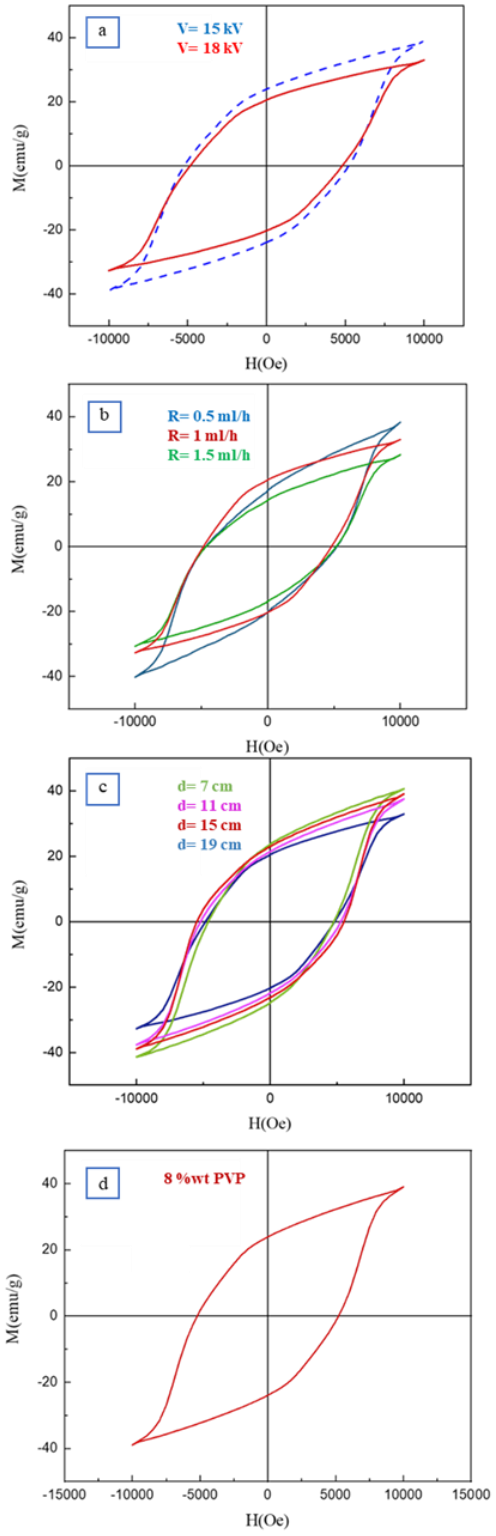

Figure 4. (a) Hysteresis loops of the randomly oriented $SrFe_{12}O_{19}$ nanofibers obtained at 15 kV and 18 kV applied voltages. (b) Hysteresis loops of nanofibers obtained at 0.5 ml/h, 1 ml/h and 1.5 ml/h flow rates. (c) Hysteresis loops of nanofibers obtained at different distances between nozzle tip and collector. (d) Hysteresis loop of nanofibers with 8 wt% PVP

The decrease in coercivity at 19 cm suggests that, at this longer distance, the benefits of increased evaporation time are outweighed by other factors such as jet instability or over-evaporation. This could lead to fibers with more surface defects or inconsistent diameters, reducing coercivity (Teo et al., 2006).

This result highlights the importance of balancing the distance to optimize fiber uniformity and magnetic properties (Sill et al., 2008). Figure 4(d) shows the hysteresis loops of the strontium ferrite nanofibers obtained at polymer concentrations of 8 wt%. As shown in Table 2, with increasing amounts of PVP, the fiber diameter increases, causing the Hc to decrease from 4.20 × 10^5 A/m to 3.84 × 10^5 A/m according to Equation (3). Since the nanofibers are not fully saturated in the VSM analysis, the Law of Approach to Saturation (LAS), as shown in Equation (4), was used for an accurate determination of the saturation magnetization. The magnetic properties of all samples are reported in table 2.

$$M(H) = M_s\left(1 - \frac{a}{H} - \frac{b}{H^2}\right) + \aleph H \quad (4)$$

where M(H) presents the magnetization at a given applied magnetic field (H), M_s stands for the saturation magnetization, and a and b are fitting parameters that account for deviations from saturation. The terms $\frac{a}{H}$ and $\frac{b}{H^2}$ represent the approach to saturation. As H increases, these terms decrease, causing the magnetization to approach M_s. The term ℵH accounts for the linear increase in magnetization with the applied field due to the linear response of some magnetic moments not aligned with the applied field (Chitra Devi et al., 2019).

TABLE 2. magnetic properties of the randomly oriented $SrFe_{12}O_{19}$ nanofibers

Sample	$M_{s\,(VSM)}$ (A.m²/kg) & (emu/g)	$M_{s(LAS)}$ (A.m²/kg) & (emu/g)	M_r (A.m²/kg) & (emu/g)	H_c (A/m) (Oe)
8 wt% PVP	47	68	28	4.20 × 10^5 5281
12 wt% PVP	33	54	20	3.84 × 10^5 4828
Voltage of 15 kV	33	54	20	3.84 × 10^5 4828
Voltage of 18 kV	39	62	24	4.10 × 10^5 5153
Flow rate of 0.5 ml/h	38	65	19	3.90 × 10^5 4899
Flow rate of 1.0 ml/h	33	54	20	3.84 × 10^5 4828
Flow rate of 1.5 ml/h	28	46	16	3.83 × 10^5 4814
Distance of 7 cm	41	63	33	3.70 × 10^5 4643
Distance of 11 cm	38	62	22	4.12 × 10^5 5184
Distance of 15 cm	39	60	23	4.29 × 10^5 5390
Distance of 19 cm	33	54	20	3.84 × 10^5 4828

4. CONCLUSION(S)

In this study, electrospinning was utilized to fabricate strontium ferrite nanofibers, which were subsequently calcined at 800°C. X-ray diffraction (XRD) confirmed the formation of a single-phase structure. Investigations into the magnetic and structural properties using FE-SEM, XRD, and VSM revealed significant outcomes. Higher polymer concentrations in the electrospinning solution were correlated with larger nanofiber diameters, with notable effects on coercivity observed in samples containing PVP concentrations of 8 wt% and 12 wt%. The optimized sample, processed at 800°C with 12 wt% PVP, exhibited excellent magnetic properties, achieving a coercivity of 4.29×10^5A/m and a saturation magnetization of 60.05 A·m²/kg. Additionally, increasing the electrospinning voltage effectively reduced nanofiber diameters. This was evident in SEM images, where distinctive bead-like structures appeared at 21 kV. These findings underscore the potential of electrospinning for precisely tailoring the magnetic and structural characteristics of strontium ferrite nanofibers, presenting promising possibilities for applications in advanced magnetic materials.

ACKNOWLEDGEMENTS

We gratefully acknowledge Department of Materials Engineering, Malek Ashtar University of Technology, Isfahan, Iran for financial support.

NOMENCLATURE

a and b in Equation (4)	Fitting parameters in LAS equation
a and c in Table (1)	Lattice parameters for unit cell dimensions
d	Interplanar spacing
D	Fiber diameter impacting magnetic properties
DMF	N, N-dimethylformamide, a solvent
EDS	Energy-dispersive X-ray spectroscopy
FE-SEM	Field emission scanning electron microscopy diameter
H_c	Field strength needed to demagnetize
K	Anisotropy constant
L	Average crystal size
LAS	Method for determining saturation magnetization, particularly when full saturation isn't reached in VSM's range
M(H)	Magnetization at a given field
Miller Indices	Crystal planes orientation notation
M_r	Magnetization left after the field is removed
M_s	Maximum magnetization achievable
M_s (LAS)	Saturation magnetization using LAS method
PVP	Polyvinylpyrrolidone, a polymer-based matrix
$SrFe_{12}O_{19}$	Strontium ferrite
V	Unit cell volume
VSM	Vibrating sample magnetometer
XRD	X-ray diffraction
β	Full width at half maximum (FWHM) of the diffraction peak
λ	X-ray wavelength
μ_0	Magnetic field production constant
א	Accounts for linear magnetization increase in LAS

REFERENCES

1. Chitra Devi, E., & Soibam, I. (2019). Law of approach to saturation in Mn–Zn ferrite nanoparticles. *Journal of Superconductivity and Novel Magnetism*, *32*. https://doi.org/10.1007/s10948-018-4823-4
2. Cong-ju, L., & Xu, G. (2011). Template preparation of strontium hexaferrite ($SrFe_{12}O_{19}$) micro/nanostructures: Characterization, synthesis mechanism and magnetic properties. *Materials Research Bulletin*, *46*, 119-123. https://doi.org/10.1016/j.materresbull.2010.09.030
3. Dabirian, F., Hosseini Ravandi, S. A., & Pishevar, A. (2010). Investigation of parameters affecting PAN nanofiber production using electrical and centrifugal forces as a novel method. *Current Nanoscience*, *6*, 545-552. https://doi.org/10.2174/157341310797575078
4. Deitzel, J., Kleinmeyer, J., Harris, D. E. A., & Tan, N. B. (2001). The effect of processing variables on the morphology of electrospun nanofibers and textiles. *Polymer*, *42*, 261-272. https://doi.org/10.3390/nano10061077
5. Gupta, A., & Roy, P. K. (2024). Improved strontium hexaferrites: An overview of current progress in synthesis, properties, and applications. *Materials Science and Engineering: B*, *306*, 117458. https://doi.org/10.1016/j.mseb.2024.117458
6. Huang, Z.-M., Zhang, Y., & Kotaki, M. (2003). A review on polymer nanofibers by electrospinning and their applications in nanocomposites. *Composites Science and Technology*, *63*, 2223-2253. https://doi.org/10.1016/S0266-3538(03)00178-7
7. Huang, X., Chen, K., Zhang, Z., Li, C., Li, P., Wang, X., & Lu, J. (2024). Study on the hydrolysis characteristics of polymeric aluminum chloride forced by fine bubbles and its key factors affecting the efficiency and capacity of forcing hydrolysis. *Water Research*, *250*, 122757. https://doi.org/10.1016/j.watres.2024.122757
8. Jing, P., Wang, Y., Wu, W., Li, H., & Yang, S. (2015). Width-controlled M-type hexagonal strontium ferrite ($SrFe_{12}O_{19}$) nanoribbons with high saturation magnetization and superior coercivity synthesized by electrospinning. *Scientific Reports*, *5*, 15089. https://doi.org/10.1038/srep15089
9. Kim, G., Kim, S., Jeong, H., & Chung, J. (2024). Numerical analysis of mixing performance in Y-junction mixers and its impact on yields from supercritical water hydrolysis. *The Journal of Supercritical Fluids*, *215*, 106425. https://doi.org/10.1016/j.supflu.2024.106425
10. Liu, G. F., Wang, S., Zhang, Y., & Xu, L. (2015). Magnetic properties and unusual morphologies of barium ferrites prepared by electrospinning and sol-gel auto-combustion method. *Materials Science Forum*, *815*, 141-146. https://doi.org/10.4028/www.scientific.net/MSF.815.141
11. Lu, Y., Yang, X. C., Zhu, J. L., Song, F. Z., & Shen, X. Q. (2011). Morphological and magnetic characteristics of strontium ferrite micro- and nanofibers. *Advanced Materials Research*, *399-401*, 736-740. https://doi.org/10.4028/www.scientific.net/AMR.399-401.736
12. Mathews, S., & Babu, D. (2021). Analysis of the role of M-type hexaferrite-based materials in electromagnetic interference shielding. *Current Applied Physics*, *29*. https://doi.org/10.1016/j.cap.2021.06.001
13. Mit-uppatham, C., Nithitanakul, M., & Supaphol, P. (2004). Ultrafine electrospun polyamide-6 fibers: Effect of solution conditions on morphology and average fiber diameter. *Macromolecular Chemistry and Physics*, *205*, 2327-2338. https://doi.org/10.1002/macp.200400225
14. Morales, A., & Lieber, C. (1998). A laser ablation method for the synthesis of crystalline semiconductor nanowires. *Science*, *279*, 208-211. https://doi.org/10.1126/science.279.5348.208
15. Na, K. H., Kim, J. H., & Kim, S. H. (2018). Fabrication and characterization of the magnetic ferrite nanofibers by electrospinning process. *Thin Solid Films*, *660*. https://doi.org/10.1016/j.tsf.2018.06.018
16. Pillay, V., de Jongh, J., & Choonara, Y. E. (2013). A review of the effect of processing variables on the fabrication of electrospun nanofibers for drug delivery applications. *Journal of Nanomaterials*, *2013*. https://doi.org/10.1155/2013/789289
17. Pullar, R. C. (2012). Hexagonal ferrites: A review of the synthesis, properties and applications of hexaferrite ceramics. *Progress in Materials Science*, *57(7)*, 1191–1334. https://doi.org/10.1016/j.pmatsci.2012.04.001
18. Ramakrishna, K. F. S., Teo, W.-E., Lim, T.-C., & Ma, Z. (2005). An introduction to electrospinning and nanofibers (p. 396). *World Scientific Publishing Co. Pte. Ltd*. https://doi.org/10.1142/9789812567611
19. Shen, X., Liu, M., Song, F., & Meng, X. (2010). Structural evolution and magnetic properties of $SrFe_{12}O_{19}$ nanofibers by electrospinning. *Journal of Sol-Gel Science and Technology*, *53(2)*, 448–453. https://doi.org/10.1007/s10971-009-2119-7
20. Shen, X., Yan, D., Wei, D., & Xu, Z. (2012). Shape anisotropy, exchange-coupling interaction and microwave absorption of hard/soft nanocomposite ferrite microfibers. *Journal of the American Ceramic Society*, *95(12)*, 3863-3870. https://doi.org/10.1111/j.1551-2916.2012.05375.x
21. Sill, T., & Recum, H. (2008). Electrospinning: Applications in drug delivery and tissue engineering. *Biomaterials*, *29*, 1989-2006. https://doi.org/10.1016/j.biomaterials.2008.01.011
22. Supekar, S., Gawde, M. S., & Bhagat, S. (2024). Relationship between structural and magnetic properties of 48Ni–52Fe laminates: Improvement study induced by annealing conditions. *Journal of Materials Science: Materials in Electronics*, *35*. https://doi.org/10.3390/nano10061077

23. Teo, W. (2006). A review on electrospinning design and nanofibre assemblies. *Nanotechnology*, *17*, R89-R106. https://doi.org/10.1088/0957-4484/17/14/R01

24. Wang, W., Liu, Y., Xu, C., Zheng, C., & Wang, G. (2002). Synthesis of NiO nanorods by a novel simple precursor thermal decomposition approach. *Chemical Physics Letters*, *362*, 119-122. https://doi.org/10.1016/S0009-2614(02)00996-X

25. Y, D., & Xia, Y. N. (2004). Electrospinning of nanofibers: Reinventing the wheel? *Advanced Materials*, *16*, 1151-1170. https://doi.org/10.1002/adma.200400719

26. Yang, Y., Liu, X., Jin, D., Huang, K., & Gao, S. (2014). The effects of the iron content on structural and magnetic properties of $Sr_{0.80}La_{0.20}Fe_xZn_{0.15}O_{19}$ hexagonal ferrites. *Journal of Magnetism and Magnetic Materials*, *355*, 254–258. https://doi.org/10.1016/j.jmmm.2013.12.010

Advanced Ceramics Progress

Volume 10, Number 2, Spring 2024)

CONTENTS

Journal Home Page: www.acerp.ir